Design and Fabrication of Flexible Neuromorphic Devices for Enhanced Learning and Memory Emulation

A Thesis
Submitted for the Degree of

Doctor of Philosophy

By

Bhupesh Yadav

Chemistry and Physics of Materials Unit
Jawaharlal Nehru Centre for Advanced Scientific Research
(An Institution Deemed-to-be-University)
Bengaluru-560064 (India)
August 2024

Declaration

I hereby declare that the thesis entitled "**Design and Fabrication of Flexible Neuromorphic Devices for Enhanced Learning and Memory Emulation**" is an authentic record of research work carried out by me at the Chemistry and Physics of Materials Unit, Jawaharlal Nehru Centre for Advanced Scientific Research, Bengaluru, India under the supervision of Prof. Giridhar U. Kulkarni and that it has not been submitted elsewhere for the award of any degree or diploma. In keeping with the general practice in reporting scientific observations, due acknowledgment has been made whenever the work described is based on the findings of other investigators. Any omission that might have occurred due to oversight or error in judgment is regretted.

Bhupesh Yadav

Certificate

Certified that the work described in this thesis titled "**Design and Fabrication of Flexible Neuromorphic Devices for Enhanced Learning and Memory Emulation**" has been carried out by Bhupesh Yadav at the Chemistry and Physics of Materials Unit, Jawaharlal Nehru Centre for Advanced Scientific Research, Bengaluru, India, under my supervision and that it has not been submitted elsewhere for the award of any degree or diploma.

Professor Giridhar U. Kulkarni
(Research Supervisor)

Acknowledgments

First and foremost, I would like to thank my research supervisor ***Professor Giridhar U. Kulkarni,*** for his constant guidance and support throughout this research journey. I am very grateful to him for introducing me to the research field, suggesting very interesting ideas, and thus encouraging and motivating me towards new explorations. His meticulous approach to experimental design or analyzing the data has inspired me to achieve such confidence in designing and performing research.

Prof. C. N. R. Rao, a constant source of inspiration and it is always a great opportunity to listen to encouraging words about research by the legend. I learned more about him through my research supervisor, who himself is a great disciple of Prof. Rao.
I thank past and present ***Presidents of JNCASR*** for their immense support in various activities.

It is my pleasure to thank the past and present ***Chairmen of CPMU*** for allowing me to use department instrumentation facilities.

I thank all ***my collaborators***; Prof. Vidhyadhiraja, Dr. Bharath B, Dr. Indrajit Mondal, Dr. Manpreet Kaur and Ms. Shubhanshi for their fruitful discussion and active collaboration.

I thank all the ***faculty members of JNCASR and CeNS*** for their cordiality, especially my teachers, Prof. A. Sundaresan, Prof. Bivas Saha, Prof. Giridhar U. Kulkarni, for their courses.
Timely and ready assistance and also friendly attitude from ***technical staff*** is greatly acknowledged. I thank Mr. Srinivas, Mr. Srinath, Mr. Alla Srinivasarao, Mr. Sanjit, Dr. Basavaraja, Ms. Meenakshi, Ms. Remya, Mr. Kannan for their invaluable technical assistance.

Special thanks to Mr. Sunil, Mrs. Vanitha, and Ms. Reetu for their assistance in various activities.

I am grateful to ***my past and present lab mates***; Dr. Sunil Walia, Dr. Ashutosh, Dr. Bharath, Dr. Chaitali, Dr. Nikita, Dr. Indrajit, Dr. Suman, Dr. Rajshekhar, Dr. Suchithra, Dr. Subash, Dr. Ganesh Dr. Manpreet, Dr. Simantini, Dr. Sriram, Dr. Swathi, Dr. Arti, Ankit, Rahul, Mukhesh, Tejaswini, Shubhanshi, Shubham, Mousona, Chirag, Ann Mary, Sukanya, Parvathy, Pavitra.

A special note of thanks goes to Ms. Surabhi, Ms. Tejaswini, Ms. Shubhanshi, Ms. Mousona, Mr. Shubham and Mr. Rohit and for proofreading the thesis.

I thank the staff of the academic and administrative section in JNCASR for their assistance.

I would like to thank the library, computer lab, Dhanvantri and hostel staff for their cooperation and help. I thank JNC Gardening and security staff for maintaining this campus beautiful and safe.

I thank ***JNCASR and CSIR*** for residential, financial assistance and ***DST*** for providing facilities. I thank all my 2019 batch mates. I thank all my friends in and out of JNCASR for their wonderful friendship and unconditional love and affection.

Special thanks to Ms. Surabhi for the help, support and joyful moments.

Volleyball Group: Chetan, Sinay, Rahul Rawat, Rahul Yadav, Suryadev, Jatin, Amrendra, Sudip, Arka, Umesh Sir and CPMU volleyball team.

Friends: Ankit, Rohit, Dr. Rajendra, Abhishek, Swaraj, Monis, Nilutpal, Geetansh, Rajarshi, Abhijit, Sujan, Shiv, Mukhesh, Soumita, Daizy, Surishi, Divya, Preeti, Himanshu, Debattam and Dheemahi.

The Boys Group: Shashank, Kamlesh, Uttam, Dr. Panda, Dr. Reetendra, Dr. Navneet, Dr. Ashutosh, Dr. Momin, Dr. Narendra, Dr. Shivram, Mayank and Pogo for unwavering support.

School and college friends: Vaishali, Sumit, Shivani, Alka, Shubham and Shailesh.

All the friends, acquaintances and well-wishers.

I thank all my ***teachers***.

Besides research life, Prof. G. U. Kulkarni and his family's personal care and affection are greatly acknowledged for providing me a home away from home. I thank Mrs. Indira Kulkarni, Teju and Poorna for their warmth and hospitality.

I would like to thank my parents, siblings for their continuous and consistent support and encouragement; otherwise, I could not have come thus far.

I thank the Almighty for his blessings.

Preface

Neuromorphic devices inspired by the structure and functionalities of brain offers a promising path for efficient and low-power information processing. These devices emulate biological synaptic activity as well as few cognitive behaviors showing a novel approach to artificial intelligence applications. By mimicking synaptic functionalities, these devices inspire the development of more adaptive and intelligent systems, capable of real-time learning and evolving. Additionally, neuromorphic devices can be integrated into various applications such as robotics and autonomous systems. The advancement of this technology has the potential to bridge the gap between machine intelligence and human cognition. The thesis presents the design and fabrication of such flexible neuromorphic devices capable of emulating various synaptic functionalities. The primary focus of the research includes the fabrication of neuromorphic devices to emulate synaptic functionalities of the brain. The thesis is divided into six chapters.

Chapter I provides an overview of neuromorphic devices, categorizing them based on their input stimuli and underlying mechanisms. It concludes with the scope of the thesis.

Chapter II describes the fabrication and characterization techniques employed to create these devices.

Chapter III focuses on the optimization of a self-formed dewetted Ag as the active material for neuromorphic device fabrication. This material is formed by heating a 30 nm Ag film resulting in Ag agglomerates separated by nanogaps. This unique dewetted Ag morphology resembles the structural complexity of biological neural networks. Electrical stimulation enables various synaptic functionalities such as threshold switching, short-term plasticity (STP) and long-term plasticity (LTP). The application of carefully designed voltage pulses enables the device to emulate higher-order learning behavior including first and second-order associative learning and Ebbinghaus forgetting of associative learning.

Chapter IV describes the fabrication of a flexible synaptic device using Kapton as a flexible substrate. This device translates neuromorphic behavior to flexible substrates, demonstrating STP, LTP, and multiple conductance states even in the bent state. For the first time, classical conditioning was emulated in the bent state using this flexible device.

Chapter V introduces the fabrication of strain-sensitive neuromorphic devices without the aid of integrated sensors for perception. The crackle lithography enables the formation of percolating metal networks to fabricate such strain-sensitive devices. This chapter contains two sections. **Chapter VA** describes the fabrication of a dual-functional device working as a strain sensor at low strain values, while electrical stimulation of the same device at higher strains helps in exhibiting neuromorphic functionalities. The device contains Ag metal mesh as active material on a PDMS substrate. The fabricated device performed speech recognition and mechanical frequency detection while being in strain sensor regime. Also, the device performs basic synaptic functionalities such as threshold switching, STP and LTP behavior in the neuromorphic regime. The strain sensitivity of the device was enhanced by a factor of 10^6 in the neuromorphic regime. The device could also emulate strain-dependent switching as well as plasticity behavior by utilising strain as an additional stimulus. By leveraging this strain-dependent behavior and combining electrical and strain inputs, the device mimics the pain-related response of the biological systems including nociception and antinociception. **Chapter VB** presents a tactile neuromorphic device that utilises strain as an input stimulus for neuromorphic functionalities. The device containing semi-embedded Au micro-mesh in a PDMS substrate demonstrated learning behaviors such as slow and fast learning leading to STP and LTP behavior. Notably, the device exhibits a paired-pulse facilitation (PPF) value of more than 200%, close to the PPF value in biological systems.

Chapter VI provides a summary of the thesis work and offers an outlook on future directions of the developed neuromorphic devices.

Table of contents

Declaration I

Certificate III

Acknowledgments V

Preface VII

Table of Contents IX

Acronyms XI

Chapter I: Introduction 1

I.A In-materia Intelligence.....1

I.B Brain: Synapse and synaptic functionalities.....3

I.C Synapse emulation with neuromorphic devices: architecture and crucial parameters.....4

I.D Classification of neuromorphic devices.....6

I.E Emulation of cognitive behaviors in neuromorphic devices.....15

I.F Scope of the thesis.....17

Chapter II: Fabrication and Characterization Techniques 23

Chapter III: Optimized Active Material for Neuromorphic Device Fabrication: Emulating Ebbinghaus Forgetting of Associative Learning 25

III.1: Introduction.....25

III.2: Scope of the present investigation.....28

III.3: Experimental details.....28

III.4: Results and discussion.....28

III.5: Conclusions.....48

References.....49

Chapter IV: A Flexible Artificial Synaptic Network: Fabrication, Characterization, and Emulating Synaptic Activity 55

IV.1: Introduction.....55

IV.2: Scope of the present investigation……57
IV.3: Experimental details……57
IV.4: Results and discussion……58
IV.5: Conclusions……69
References……70

Chapter V: Development of Strain Sensitive Neuromorphic Devices 77

Chapter VA: A Stretchable Neuromorphic Device Mimicking Pain related Response

VA.1:Introduction……77
VA.2: Scope of the present investigation……79
VA.3: Experimental details……80
VA.4: Results and discussion……81
VA.5: Conclusions……101
References……102

Chapter VB: Designing a Tactile Neuromorphic Device using Strain as Input Stimulus

VB.1: Introduction……111
VB.2: Scope of the present investigation……113
VB.3: Experimental details……113
VB.4: Results and discussion……114
VB.5: Conclusions……121
References……122

Chapter VI: Summary and Outlook……125

List of Publications……127

Acronyms

AFM	Atomic Force Microscopy
Ag	Silver
ASN	Artificial Synaptic Network
Au	Gold
CMOS	Complementary Metal Oxide Semiconductor
ECM	Electro Chemical Metallization
ECT	Electrochemical Transistor
EPSC	Excitatory Post Synaptic Current
FESEM	Field Emission Scanning Electron Microscope
HRS	High Resistance State
LRS	Low Resistance State
LTM	Long-Term Memory
LTP	Long-Term Plasticity
MTJ	Magnetic tunnel Junctions
NVM	Non-Volatile Memory
PCM	Phase Change Memory
RRAM	Resistive Random-Access memory
SADP	Spike Amplitude Dependent Plasticity
SEM	Scanning Electron Microscopy
Si	Silicon
SRDP	Spike Rate Dependent Plasticity
STM	Short-Term Memory
STP	Short-Term Plasticity
TCR	Temperature Coefficient of Resistance
TM	Transition Metal Dichalcogenides
UV	Ultraviolet
VCM	Valence Change Memory
XRD	X-ray Diffraction

Chapter I

Introduction

I.A *In-materia* intelligence

In recent years, there has been a tremendous advancement in the fabrication of neuromorphic devices, particularly utilising a wide range of materials during fabrication [1]. Neuromorphic devices are inspired by the structure and the functionalities of the brain and aim to mimic the operation of synapses [2]. The incorporation of nanomaterials in neuromorphic devices opens new paths for developing the energy energy-efficient and low-power neuromorphic systems because of the unique properties of materials at the nanoscale [3]. These devices utilise the excellent properties of nanomaterials such as tunable electronic properties, high surface area, and nanoscale precision to develop active material equivalent to neurons [4]. This technological development is the foundation for the next generation of artificial intelligence (AI) and intelligent systems.

Conventional computing systems, based on the von Neumann architecture, face efficiency challenges due to the separation of memory and processing units, known as the von Neumann bottleneck [5]. This separation results in increased space requirements, longer data transfer times, and higher power consumption when moving data between memory and processing units, leading to suboptimal computational performance. Moreover, these systems operate on binary digits (0s and 1s), which can be limiting for complex, parallel processing tasks. For instance, a powerful supercomputer takes 365 days to emulate the brain activity of a rodent by consuming ~MWs energy [6]. This highlights the critical need for a paradigm shift in the current computing architectures, where neuromorphic devices could offer a potential alternative. To tackle these challenges, researchers are exploring neuromorphic devices that integrate memory and processing capabilities, emulating the efficiency and functionality of the human brain [7]. These devices could usher in a new computing paradigm, aiming to mimic the brain's ability of parallel processing effectively overcoming the von Neumann bottleneck [8]. For the realization of neuromorphic devices, memristors are very promising candidates [1]. These specific electronic components exhibit memory resistance, meaning their resistance varies based on past

voltage and current. Memristor technology is rapidly advancing due to its non-volatile nature, nanometer scale, simple structure, high speed, and low power consumption. These characteristics, similar to synapses in the brain, make memristors highly suitable for neuromorphic computing. Consequently, a lot of research has been done to develop resistive random-access memory (RRAM), another term for memristors.

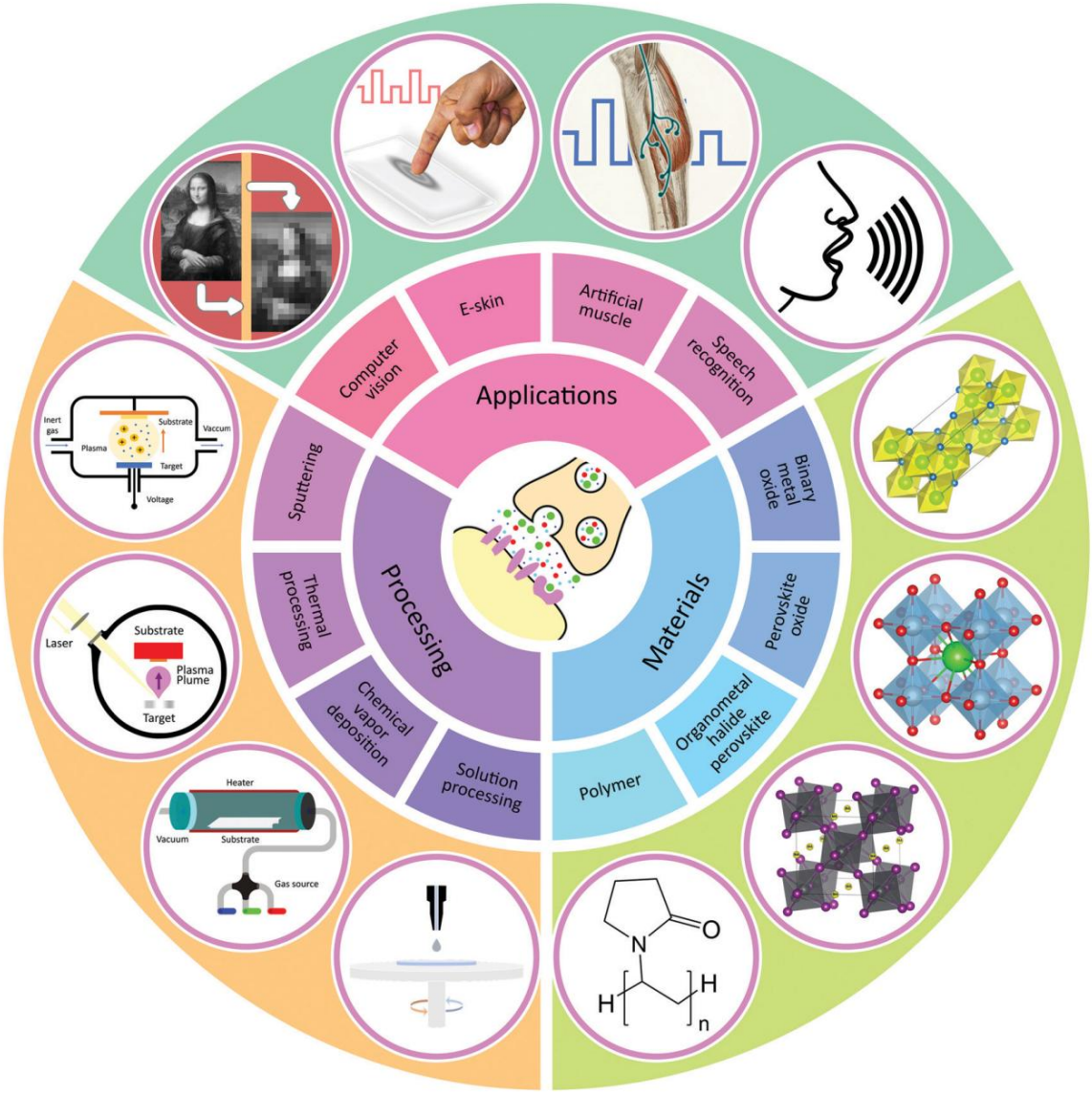

Figure I.1: Recent materials utilised for the fabrication of artificial synaptic devices. Figure adapted with permission from Reference 9; copyright 2021 Royal Society of Chemistry.

To date, numerous materials demonstrating synaptic behavior have been explored, including transition metal oxides, organic and inorganic oxides, polymers, 2D materials (such as graphene, MoS_2, WSe_2), nanoparticles, nanowires, nanofibers, perovskites, and quantum dots (Figure I.1)[9]. These materials display excellent electrical, optical and

mechanical properties making them a promising candidate for neuromorphic applications.

I.B Brain: Synapse and synaptic functionalities

Before discussing further about neuromorphic devices, it is crucial to understand what makes the brain so fascinating that people are trying to mimic its functionalities. The human brain, an extraordinary marvel of nature, is regarded as the most complex structure in the known universe. Acting as the control centre for the entire body, it consists of approximately 100 billion neurons interconnected by trillions of synapses [10]. This extensive neural network excels in parallel computing, enabling the brain to process vast amounts of information simultaneously and adaptively at incredible speeds (up to 10^{18} operations per second) while consuming only about 20 watts of power [11]. Inspired by the brain's remarkable capabilities, scientists and engineers have endeavored to create architectures that replicate its functionalities.

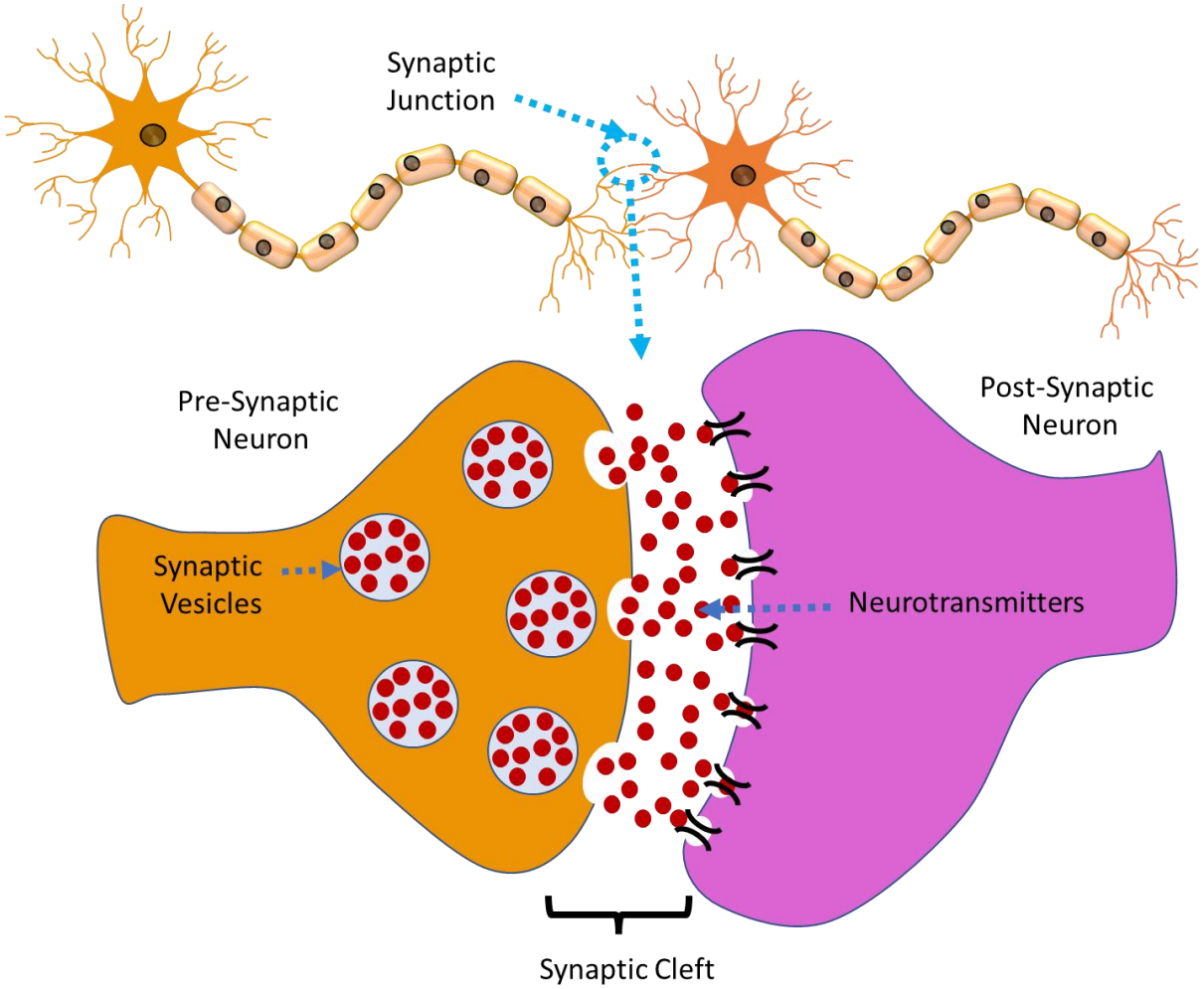

Figure I.2: Schematic representing the synaptic junction between the neurons and synapse.

The functioning of the brain relies on the neurons and synapses at the cellular level [12]. A synapse is a junction that helps in the transfer of information from one neuron (pre-synaptic neuron) to the other (post-synaptic neuron) or vice versa (Figure I.2). Whenever any information is received by sensory neurons it travels to the brain as an electrical signal known as action potential. At the synapse, this action potential forces the synaptic vesicles in the pre-synaptic neuron to move towards the synaptic cleft (the gap between the two neurons) and triggers the release of the neurotransmitters across the synaptic cleft. These neurotransmitters are further received by the receptors on the post-synaptic neurons which results in a change of synaptic weight of the junction. Synaptic weight is the strength of the connection between the two neurons. The higher synaptic weight is associated with better memory formation and retention [13]. The two distinct kinds of memory forms are typically known as short-term memory (STM) and long-term memory (LTM). The changes in synaptic strength which occur for a short period form the STM while changes in synaptic strength extended for a longer time or the permanent alteration of the connection result in the LTM.

I.C Synapse emulation with neuromorphic devices: architecture and crucial parameters

To emulate such functionalities, synaptic activity emulation is a fundamental starting point. Neuromorphic devices usually mimic this synaptic activity using typical two-terminal memristor geometry with a metal-insulator-metal (MIM) structure (Figure I.3)[14]. In this setup, the top and bottom metals serve as the top electrode (TE) and bottom electrode (BE), respectively, while the insulating layer functions as the resistance resistance-switching medium. Information is encoded by the resistance state of the device, which can be altered or modulated by applying specific voltage sweeps or pulses. For instance, Jang et.al. utilised the Cu/pV3D3/Al geometry to fabricate a synaptic device [14]. The application of electrical stimulation induces the formation of a filamentary conduction path within the active material resulting in a change in the conductance of the device. To compare such a structure with the biological synapse, the top electrode here represents the presynaptic neuron, and the bottom electrode serves as the postsynaptic neuron. These devices exhibit plasticity behavior by modulating the conductance state of the device in response to external stimuli akin to the synaptic weight change of the neurons.

The neuromorphic devices modulate the property of their active material or the conductance of the device using electrical stimuli, often in the form of voltage pulses, to emulate the synaptic functionalities [15,16]. The key parameters of these voltage pulses are pulse amplitude (V_P), pulse interval (t_w), pulse interval (t_i), pulse number (N_P), and reading voltage (V_R) play a significant role in shaping the behavior of these devices. Then, there is current compliance (I_{CC}) which controls maximum electrical burden on the device. During the application of these pulses, the conductance of the device shows an enhancement as illustrated in Figure I.4. However, after the removal of the pulses, the device tends to retain this enhanced conductance for a finite period of time, typically measured with minimal V_R. The retention and decay of the conductance are highly influenced by the device architecture and the pulsing conditions. V_R is generally very small (~ mV) so as not to disturb the conductance state during the retention. The table in Figure I.4b presents the rudimentary comparison of the typical ranges of the parameters between bio-neuron and neuromorphic devices.

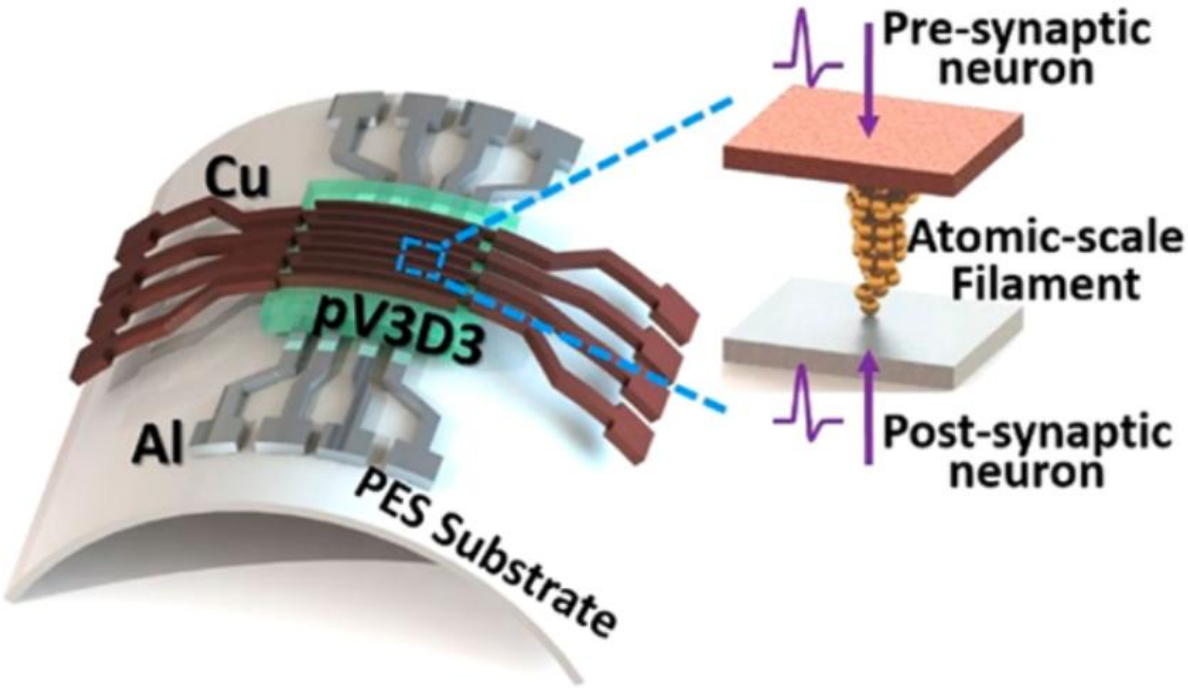

Figure I.3: Schematic showing two-terminal memristor as electronic synapse with Cu/pV3D3/Al geometry on a flexible PES substrate. The top and bottom electrodes resemble the presynaptic and postsynaptic neurons, respectively. Figure adapted with permission from Reference 14; copyright 2019 American Chemical Society.

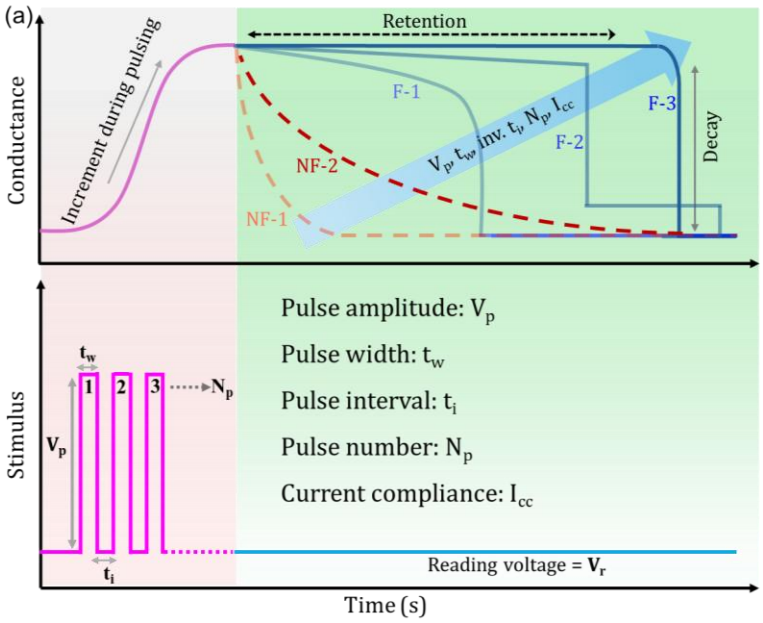

(b)

Stimulus parameters	Bio-range	Neuromorphic range
V_p	-70 to +30 mV	-10 to +10 V
t_w	2 to 5 ms	1 ms to 10 s
t_i	1 ms (defined by refractory period) to hours	1 ms to 10 s
N_p	Undefined	1 to 1000
I_{cc}	NA (EPSC: 100 pA)	1 nA to 100 mA

Figure I.4: (a) Schematic illustrating typical memory evolution (purple incremental curve) and retention behavior of filamentary (F) and Non-Filamentary (NF) type devices, in response to applied pulses. Filamentary devices exhibit abrupt decay of conductance (Blue curves) meanwhile non-filamentary devices show exponential decay of the conductance over time. The conductance enhancement and decay behavior can be modulated using the six voltage pulse parameters. (b) Typical working ranges for neuromorphic devices compared with bio neurons.

In filamentary (F) devices, such as ECM and VCM VCM-based devices, the conductance decays abruptly [15]. This is due to the rapid formation and dissolution of conductive paths made of filaments form and dissipate rapidly which leads to abrupt decay of conductive filaments, leading to sudden change in conductance. On the other hand, non-filamentary devices typically show exponential decay of the conductance over time. These devices rely on charge trapping mechanisms, where trapped charges gradually disperse, resulting in gradual conductance decrement [17].

When all six pulse attributes are strong, it leads to longer retention of conductance exhibiting LTP behavior. Meanwhile, weak attributes could show STP behavior. The decay of conductance portrays the property of plasticity where once the information is lost the active material is available for fresh processing. It is similar to the learning and forgetting of the biological systems where active material resembles the neural content.

I.D Classification of neuromorphic devices

These devices can be classified based on the type of stimuli they use to emulate neural functions: electrical stimuli-based devices, such as memristors; optical stimuli-based devices, utilizing materials like photochromic or photorefractive materials; and other

types, including ferroelectric-based devices, spintronic devices, and biomolecular devices, each leveraging unique mechanisms and materials to mimic neural activities. This multifaceted approach promises to revolutionize computing by enhancing efficiency, speed, and capability.

I.D (a) Electrical stimuli-based devices

i. Electrochemical metallization memory (ECM):

The electrochemical metallization memory-based devices typically use a memristor geometry, metal-insulator-metal (MIM) [18,19]. It consists of a top anode electrode as active metal (Ag, Cu etc.), an electrolyte layer and inert metal as the bottom cathode electrode (Pt, TiN) [20,21]. These devices rely on electrochemical processes to mimic the synaptic behavior of biological systems. The positive voltage application to the top electrode leads to the oxidation ($M \rightarrow M^+ + e^-$) of the active metal which migrates in the direction of the field and goes through reduction ($M^+ + e^- \rightarrow M$) at the inert electrode. This process leads to a conducting filament formation across the two electrodes leading to a change in the resistance state of the device [22,23]. Conversely, the application of negative voltage on the top electrode results in the rupture of conducting filaments and resetting back of the resistance state. The conductance of these devices can be modulated by using the voltage pulses. The conductance is considered equivalent to the biological synaptic weight while voltage pulse as an action potential.

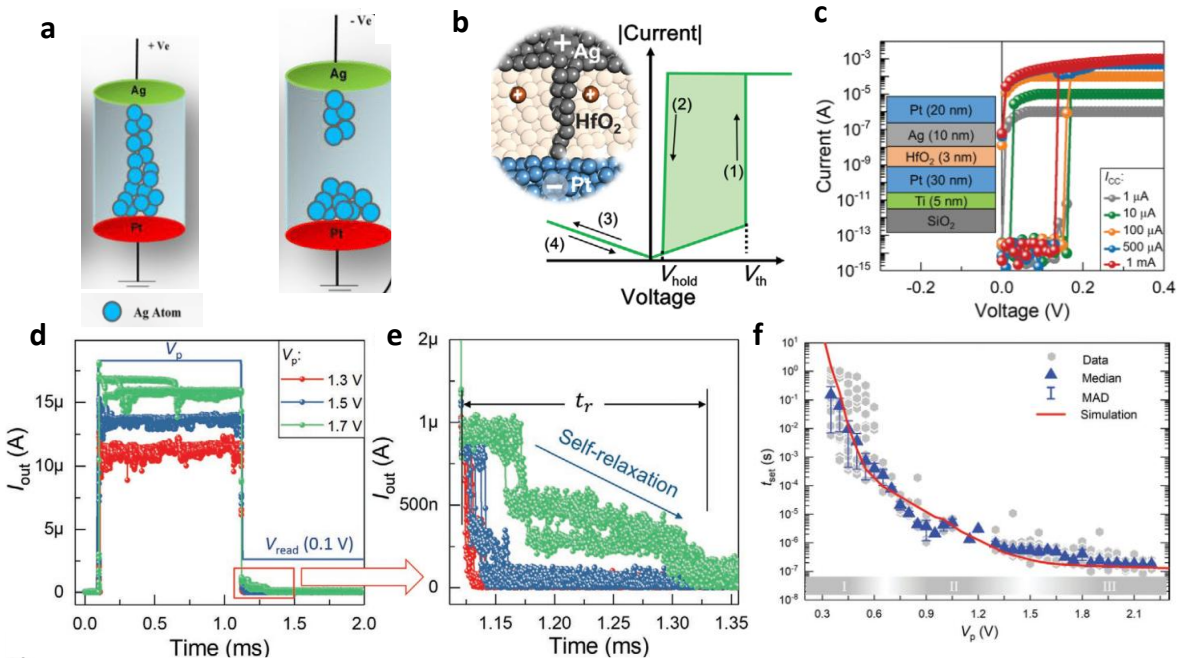

Figure I.5: (a) Schematic of the ECM device containing Ag and Pt as top and bottom electrodes (b) Typical I-V characteristic curve, demonstrating the device's switching

behavior due to conducting filament formation between the two electrodes (inset). c) Convergent switching observed at ~0.17 mV under various current compliances ranging from 1 μA to 1 mA. d) Different conductance levels of the device achieved by applying pulse amplitudes between 1.3 V and 1.7 V. e) The consequent relaxation behaviour of the device, indicating higher conductance retention levels for higher input pulses. f) The SET switching kinetics of Ag/HfO_2/Pt v-ECM cells are analysed. Median values of the experimental data are shown as triangles, with vertical lines indicating the median absolute deviation (MAD). The data is categorized into three regions: I, II, and III, corresponding to the nucleation-limited, electron-transfer-limited, and mixed control regimes, respectively. The numerical simulation results, depicted as a solid red line, are fitted to the experimental data for comparison. Figure adapted with permission from Reference 24; copyright 2022 John Wiley & Sons.

Chekol *et al*. reported such ECM-based memristor devices with Ag/Pt electrodes and HfO_2 layers (3 and 5 nm) [24]. The device exhibited abrupt volatile switching behavior as shown in Figure I.5b. The repeated switching at different current compliance shows no change in threshold voltage (Figure I.5c). The device also featured low leakage current, large on/off ratio, low V_{th}, over 10^6 switching cycles endurance, and fast switching speeds (SET and relaxation times <300 ns and 250 ns). Stability was confirmed for over 500,000 cycles using 200 μs/2 V pulses, making them suitable for neuromorphic computing and low-power applications. The relaxation time (t_r) of diffusive memristors, determined by programming voltage (V_P) (Figure I.5d) and pulse time (t_P), increased exponentially with V_P (Figure I.5e) and followed a power-law relationship with t_P. SET kinetics were influenced by both nucleation energy and ion migration dynamics, with switching speed (t_{set}) decreasing and eventually saturating with higher V_P. Three distinct regimes were identified: nucleation-limited (<0.6 V), electron-transfer limited (0.6–1.5 V), and mixed electron-transfer and ion migration limited (>1.5 V) (Figure I.5f). These findings underscore the importance of SET kinetics and filament growth mechanisms in determining relaxation behavior and optimizing memristor performance in neuromorphic circuits. Also, relaxation of the device conductance after pulse application shows the plasticity behavior in the device which makes them a suitable candidate for the development of intelligent devices.

ii. Valence change memory (VCM):

These devices also utilize a metal-insulator-metal (MIM) architecture, featuring an insulating or dielectric material between two metal electrodes [25,26]. Initially, VCM devices exhibit low conductivity due to the insulating channel. Upon applying an electric field, oxygen vacancies migrate, reducing the interface barrier height and forming

conductive filaments, thus switching the device to a high-conducting state (Figure I.6a). Precise control of the active material's stoichiometry is essential for optimal performance. Various oxide materials have been investigated for VCM devices, such as TiO_2, NbO_x, HfO_2, Ta_2O_5, NiO, CoO, ZnO, Cu_xO, and ZrO_2 [27–30]. These devices demonstrate synaptic activity and the emulation of short-term and long-term potentiation (STP and LTP) with specific electrical pulses. The filament dynamics in VCM devices are crucial, as thinner filaments dissolve quickly, leading to STP behavior, while thicker filaments exhibit stable, long-term conductance. This behavior can be controlled by adjusting pulse numbers and current compliance. The working mechanism of VCM devices involves the migration of atomic vacancies in a semiconducting matrix, forming conductive filaments under an electric field. For instance, in TiO_2-based devices [26,31], oxygen vacancies migrate toward the cathode, forming filaments that can be dissolved by a reverse voltage. Material selection is critical; metals like Pt with intermediate oxygen diffusivity [29,30] and low work function metals like Ti and Al are often used [32].

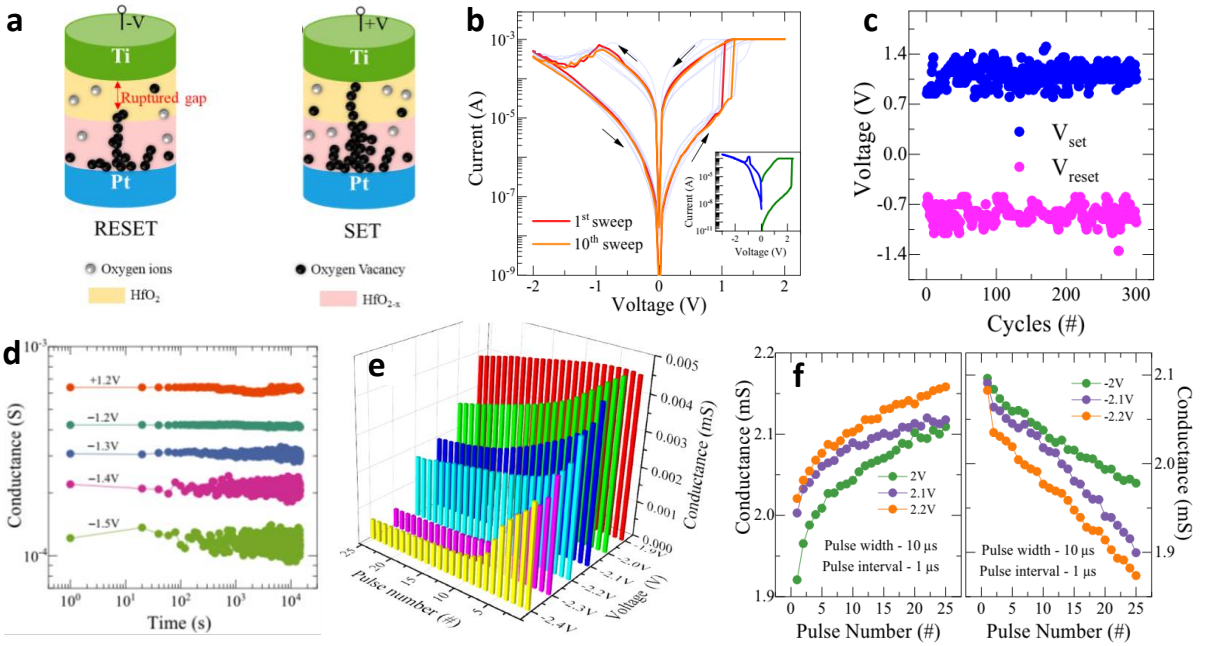

Figure I.6: (a) Schematic depicting the typical resistive switching mechanism in Ti/HfO_2/HfO_{2-x}/Pt memristive device. (b) Bipolar I–V characteristic curves are measured within a voltage sweep range of ±2 V, scanning rate of 50 mV/s. The inset displays the I–V curve during the initial electroforming process. (c) Variation of the set and reset voltages over 300 cycles, showing cycle-to-cycle variation. (d) Retention behaviour of multiple conductance states with varying pulse amplitudes, from -1.5 V to +1.2 V. (e) Variation of conductance upon application of different pulses of various amplitude. (f) Conductance behaviour during potentiation and depression with varying input parameters. Figure adapted with permission from Reference 33; copyright 2023 Nature Portfolio.

To eliminate the stochastic behavior of VCM devices, Sahu *et al*. explored Ti/HfO_2/HfO_{2-x}/Pt memristive device, having distinct HfO_2/HfO_{2-x} bilayer structure which facilitates the creation and redistribution of oxygen vacancies crucial for resistive switching [33]. DC voltage sweep measurements revealed the device's high resistance state (HRS) transitioning to a low resistance state (LRS) at ~2.3 V, with consistent bipolar resistive switching behavior (Figure I.6b). The set and reset voltages varied within narrow ranges, ensuring low voltage operation, reliability, and reproducibility. The device exhibited excellent retention and endurance properties (Figure I.6c). By controlling voltage sweep rates, the device achieved multilevel conductance states (Figure I.6d and e), emulating synaptic potentiation and depression (Figure I.6f). XPS analysis confirmed the presence of a stoichiometric upper HfO_2 layer and an oxygen-deficient lower HfO_{2-x} layer, crucial for filamentary switching. The bilayer structure enabled precise filament geometry changes, enhancing stability and reproducibility. Synaptic weight update characteristics were demonstrated with various pulse voltage conditions, indicating the device's potential for reliable synaptic plasticity. The study highlighted the importance of pulse conditions, such as amplitude, width, and interval time, in modulating synaptic weight, essential for neuromorphic computing applications.

iii. Phase change memory (PCM):

Phase change memory (PCM) devices utilize phase change materials, such as chalcogenide glass GST ($Ge_2Sb_2Te_5$)[34], In_3SbTe_2 (IST)[35], $Ag_4In_3Sb_{67}Te_{26}$ (AIST)[36] etc, for memory applications due to their fast-switching speed, high packing density, and non-volatile nature [37]. In these devices, the material is sandwiched between electrodes and can switch between a crystalline (high conducting) phase and an amorphous (low conducting) phase through Joule heating (Figure I.7a and I.7b) [38,39]. Short electric pulses induce amorphization by rapid heating and quenching, while longer pulses cause crystallization by annealing (Figure I.7c).

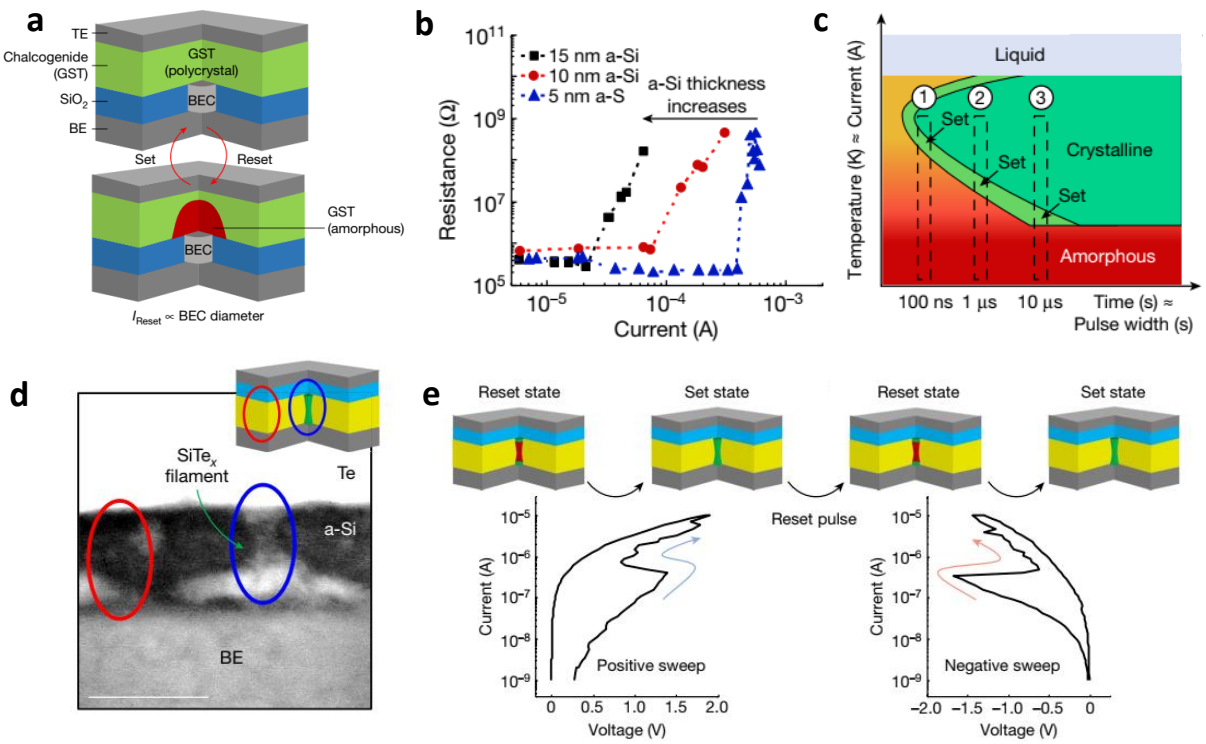

Figure I.7: (a) Illustrations depicting the set and reset operations of a conventional GST-based phase-change memory (PCM) featuring a highly confined bottom electrode contact (BEC) designed to minimize the reset current. (b) Reset process of NFPCMs with 15 nm, 10 nm, and 5 nm thick a-Si layers, resistance versus current curves demonstrating that the reset current decreases with increasing a-Si layer thickness. (c) Schematic of a time–temperature-transformation diagram illustrating the transition between amorphous and crystalline phases of a material. (d) TEM HAADF image in the set state of the NFPCM, displaying a Te filament, formed through the a-Si layer. (e) The unipolar operation of the NFPCM demonstrates that the device undergoes the set operation effectively for both positive and negative polarity current sweeps, indicating a minimal impact of electrical polarity on the resistive switching behaviour. Figure adapted with permission from Reference 40; copyright 2024 Nature Portfolio.

PCM devices feature high cyclic endurance, low power consumption, and stable states lasting over ten years. Neuromorphic computing applications benefit from PCM's ability to mimic synaptic behaviors such as potentiation and depression. Recent advancements include lignin-based synaptic devices and efforts to improve device properties through material doping and structural modifications. Traditional PCMs, however, require high reset currents, affecting energy efficiency. Park *et al*. explored nano-filament phase-change memory (NFPCM) device using a silicon telluride ($SiTe_x$) filament, which achieves ultra-low reset currents of approximately 10 µA while maintaining excellent memory characteristics [40]. This NFPCM confines the phase-change region within an electrically formed filament. This polycrystalline $SiTe_x$ filament with a diameter of approximately 5.5 nm is created by sequentially depositing chalcogenide elements (Te and Si) between two

electrodes, allowing Te atoms to migrate into the amorphous Si layer under a positive bias (Figure I.7d). Electrical measurements demonstrate the $SiTe_x$ filament's non-volatile and reversible phase-change switching with semiconductor characteristics in both polycrystalline and amorphous phases. The device significantly reduces the reset current due to efficient Joule heating, maintaining robust endurance and fast switching speeds. Additionally, the reset current is further reduced by applying a negative bias to the top electrode, retracting excess Te from the filament (Figure I.7e). This NFPCM's superior scalability and energy efficiency make it a promising candidate for advanced memory technologies in neuromorphic computing, edge processors, and in-memory computing systems.

iv. Other devices:

Beyond ECM (Electrochemical Metallization), VCM (Valence Change Memory), and PCM (Phase Change Memory) devices, several other types of neuromorphic devices have been developed to emulate the brain's neural networks. These devices leverage various physical mechanisms to achieve synaptic-like functionalities. Here are some notable examples:

Spintronic devices: Spintronic devices use the spin of electrons, in addition to their charge, to store and process information. Magnetic Tunnel Junctions (MTJs) are a common type of spintronic device used in neuromorphic computing. These devices consist of two ferromagnetic layers separated by an insulating barrier [41]. The resistance of the MTJ changes depending on the relative orientation of the magnetic moments in the two layers, enabling binary data storage. Spintronic devices offer high endurance, low power consumption, and non-volatility.

Ferroelectric devices: Ferroelectric transistors use ferroelectric materials that have a spontaneous electric polarization, which can be reversed by an external electric field [42]. This polarization state can represent binary information, and the device can mimic synaptic functions by modulating the channel conductance based on the polarization state. Ferroelectric transistors offer low power operation, non-volatility, and high switching speeds, making them suitable for neuromorphic applications.

I.D (b) Optical stimuli-based devices

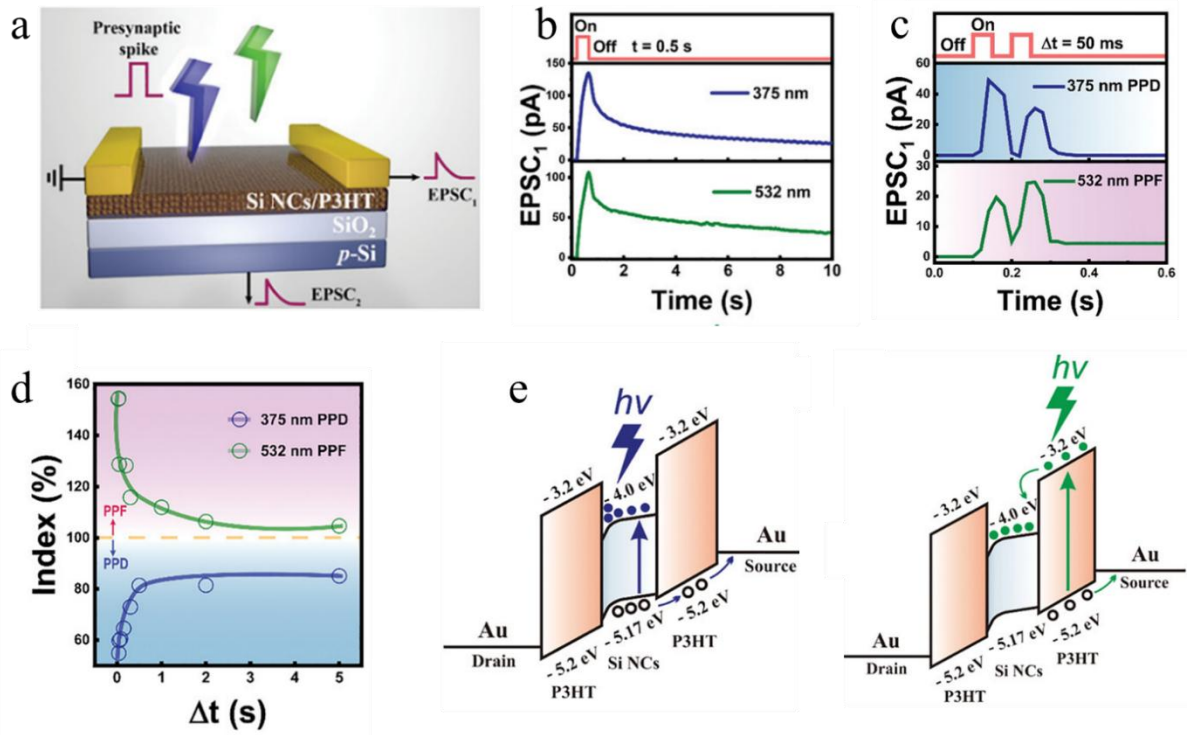

Figure I.8: Schematic of the Si NCs/P3HT heterojunction device. EPSC response of device with (b) 0.5 s pulse of 375 and 532 nm wavelength light illumination (c) two pulses with an interval of 50 ms. (d) PPF and PPD index of the device with time interval. (e) The conduction mechanism of the device involves the illumination of 375 and 532 nm wavelengths. Figure adapted with permission from Reference 44; copyright 2021 John Wiley & Sons.

These devices show neuromorphic plasticity based on light as an external stimulus. The device consists of optically active material that generates photogenerated charge carriers on light stimulation to change the conductance [43]. Wang *et al*. fabricated an optoelectronic synaptic device based on a hybrid structure of silicon nanocrystals (Si NCs) and poly(3-hexylthiophene) (P3HT), as shown in Figure I.8a [44]. Light as an input presynaptic pulse is applied to the device, and the corresponding EPSC as an output is measured. The change in conductance of the device with the illumination of 375 and 532 nm wavelength of light can be clearly observed in Figure I.8b. Depending on the wavelength of light, the device shows the EPSC (532 nm) and IPSC (375 nm) response with two pulses depicted in Figure I.8c. The device is illuminated with two pulses (pulse width 50 ms), and the EPSC ratio of the second spike (A2) and first spike (A1) was calculated with varying intervals. The value of A2/ A1 decreases (increases) with an increase in the interval between the pulse at a wavelength of 375 nm (532 nm). The pair pulse facilitation (PPF) and pair pulse depression (PPD) with time intervals between are

shown in Figure I.8d. The PPF/PPD behavior emulates the STP of the device [45]. The photogenerated charge carriers are produced on Si NCs and P3HT under 375 and 532 nm, respectively. The conduction mechanism in Figure I.8e shows that on the illumination of UV light, photogenerated electrons are trapped in Si NCs due to the potential well by the heterojunction. The photogenerated holes move towards the P3HT layer, reducing the barrier and increasing the EPSC with spike duration. The trapped electron recombines with the holes, thereby decreasing EPSC. With 532 nm illumination, photogenerated charge carriers are only formed in the P3HT layer. Most electrons are trapped in Si NCs, and holes remain in P3HT. The separation of charge carriers gives rise to an increase in EPSC.

I.D (c) Other stimuli-based devices

i. Mechanical stimuli-based devices:

Piezoelectric memristors: Piezoelectric materials generate an electric charge in response to mechanical stress. Piezoelectric memristors leverage this property to modulate resistance based on applied mechanical pressure [46]. These devices can emulate synaptic plasticity by converting mechanical signals into electrical ones, providing a direct interface between mechanical stimuli and neuromorphic computation. They are particularly useful in tactile sensing applications, where mechanical forces are predominant.

Triboelectric device: Triboelectric nanogenerators convert mechanical energy into electrical energy through contact electrification and electrostatic induction [47]. These devices can be used to drive neuromorphic devices by generating electrical pulses in response to mechanical movements. These devices can serve in applications requiring energy harvesting from motion, such as wearable electronics and self-powered sensors.

ii. Thermal stimuli-based devices:

Thermoelectric memristors: Thermoelectric materials generate a voltage when there is a temperature difference across them [48]. Thermoelectric memristors utilize this phenomenon to modulate resistance based on thermal gradients. These devices can mimic synaptic functions by responding to temperature changes, making them suitable for environments where thermal fluctuations are common. They can be used in temperature sensing and adaptive response systems.

Phase-change materials (PCMs) with thermal stimulation: While typically electrically stimulated, PCMs can also be triggered by direct thermal stimuli [37]. Heating these materials can induce phase transitions, changing their electrical resistance. Using thermal pulses to control these transitions can emulate neural activities, particularly in applications where temperature control is feasible.

iii. Chemical stimuli-based devices:

Electrochemical transistors (ECTs): Electrochemical transistors modulate their conductance based on ionic movement induced by chemical reactions [49]. These devices can emulate synaptic behavior by using chemical stimuli to alter their state. ECTs are particularly relevant in bioelectronics and interfacing with biological systems, where chemical signals play a crucial role.

iv. Pressure and strain-based devices:

Piezoresistive memristors: Piezoresistive materials alter their resistance under mechanical strain [50]. Piezoresistive memristors leverage this effect to modulate their resistance based on applied stress, mimicking synaptic functions through mechanical-to-electrical signal transduction. These devices are useful in applications requiring flexible and stretchable electronics.

I.E Emulation of cognitive behaviors in neuromorphic devices

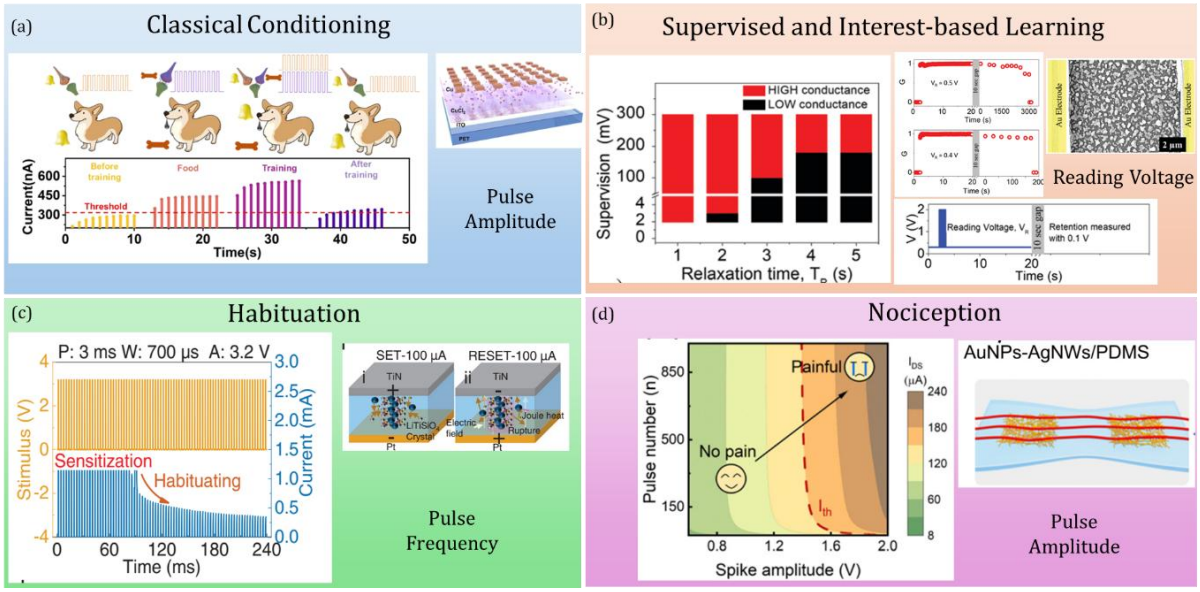

Figure I.9: Emulation of higher cognitive behavior using neuromorphic devices (a) classical conditioning emulated by utilising two distinct pulse amplitude. Figure adapted with permission from Reference 51; copyright 2024 American Chemical Society. (b) supervision and interest-based learning mimicked by using reading voltage. Figure adapted with permission from Reference 15; copyright 2020 Royal Society of Chemistry.

(c) Habituation emulated by pulse frequency modulation. Figure adapted with permission from Reference 52; copyright 2020 John Wiley & Sons. (d) The pain-related response (Nociception behavior) was replicated by adjusting the pulse amplitude. Figure adapted with permission from Reference 54; copyright 2024 Royal Society of Chemistry.

In addition to basic synaptic functionalities such as threshold switching, and short and long-term potentiation, neuromorphic devices are also explored to perform higher-order cognitive behaviours. Figure I.9 highlights a few successfully emulated cognitive behavior achieved using various neuromorphic devices. The six key parameters of the voltage pulses are carefully modulated to perform such functions. One of the basic cognitive behavior emulated using neuromorphic devices, often considered benchmark study is classical conditioning or associative learning. In this context, Meng et.al. demonstrate the emulation of associative learning by two different amplitude electrical pulses acting as unconditioned stimuli (US - food) and conditioned stimuli (CS - bell) utilising the device geometry shown in Figure 1.9a [51]. With only bell stimuli, the device response does not cross the threshold whereas, after training with the simultaneous application of food and bell stimuli, the device exhibits a response for the bell stimuli alone establishing an association between the US and the CS. Similarly, Bannur *et al.* exploits the reading voltage variations to show the mimicking of supervised and interest-based learning [15]. For mimicking the same, a self-formed dewet Ag film is employed. The variation in V_R defines the strength of supervision. The larger the V_R, the higher the retention and the stronger the supervision. The habituation behavior was also reported by Wu *et al.* with modulating the pulse frequency [52]. The study shows that synapse habituates faster to high-frequency stimuli where the response decreases gradually for the same stimuli. The brain plays a crucial role in protecting the body from harmful or noxious stimuli [53]. Some specialized sensory neurons such as nociceptors, are responsible for detecting noxious stimuli such as extreme temperature. These nociceptors send a signal to the brain which triggers the reflexive response to avoid the potential damage to the body. For example, the sudden reflex of the hand from hot surfaces is caused by the help of the brain which receives potential threat signals from the nociceptors. Xu *et al.* utilised a sequence of electrical pulses to simulate the painful behavior of threshold, sensitization, and desensitization [53]. The emulation of synaptic activity and the approach towards cognitive behavior shows that neuromorphic devices hold great promise for advancing artificial intelligence.

I.F Scope of the thesis

In the current era of big data, traditional computing systems based on von Neumann architecture are unable to fulfill the growing computation demands. Neuromorphic devices based on designs inspired by the human brain are promising in this context. A neuromorphic device is expected not only to emulate plasticity and higher-order cognitive behavior but should also do so without relying on external CMOS circuits or software platforms. Present-day neuromorphic devices involve complex fabrication techniques and only emulate limited synaptic behavior. The thesis explores the fabrication of neuromorphic devices with simple processes which show on-synapse intelligence.

References

[1] A S Sokolov, H Abbas, Y Abbas and C Choi 2021Towards engineering in memristors for emerging memory and neuromorphic computing: A review *J. Semicond.* **42** 013101

[2] Wan Q, Sharbati M T, Erickson J R, Du Y and Xiong F 2019 Emerging Artificial Synaptic Devices for Neuromorphic Computing *Adv. Mater. Technol.* **4** 1–34

[3] Lu Q, Zhao Y, Huang L, An J, Zheng Y and Yap E H 2023 Low-Dimensional-Materials-Based Flexible Artificial Synapse: Materials, Devices, and Systems *Nanomaterials* **13** 373

[4] Udaya Mohanan K 2024 Resistive Switching Devices for Neuromorphic Computing: From Foundations to Chip Level Innovations *Nanomaterials* **14** 527

[5] R. Pendurthi, D. Jayachandran, A. Kozhakhmetov, N. Trainor, J. A. Robinson, J. M. Redwing and S. Das 2022 Heterogeneous Integration of Atomically Thin Semiconductors for Non-von Neumann CMOS. *Small* **18** 2202590

[6] Kuzum D, Jeyasingh R G D, Lee B and Wong H-S P 2012 Nanoelectronic Programmable Synapses Based on Phase Change Materials for Brain-Inspired Computing *Nano Lett.* **12** 2179–86

[7] Cao G, Meng P, Chen J, Liu H, Bian R, Zhu C, Liu F and Liu Z 2021 2D Material Based Synaptic Devices for Neuromorphic Computing *Adv. Funct. Mater.* **31** 2005443

[8] Sun L, Wang W and Yang H 2020 Recent Progress in Synaptic Devices Based on 2D

Materials *Adv. Intell. Syst.* **2** 1900167

[9] Chen F, Zhou Y, Zhu Y, Zhu R, Guan P, Fan J, Zhou L, Valanoor N, von Wegner F, Saribatir E, Birznieks I, Wan T and Chu D 2021 Recent progress in artificial synaptic devices: materials, processing and applications *J. Mater. Chem. C* **9** 8372–94

[10] Yang R, Huang H-M and Guo X 2019 Memristive Synapses and Neurons for Bioinspired Computing *Adv. Electron. Mater.* **5** 1900287

[11] Huang W, Xia X, Zhu C, Steichen P, Quan W, Mao W, Yang J, Chu L and Li X 2021 Memristive Artificial Synapses for Neuromorphic Computing *Nano-Micro Lett.* **13** 85

[12] Martin S J, Grimwood P D and Morris R G M 2000 Synaptic Plasticity and Memory: An Evaluation of the Hypothesis *Annu. Rev. Neurosci.* **23** 649–711

[13] Neves G, Cooke S F and Bliss T V P 2008 Synaptic plasticity, memory and the hippocampus: a neural network approach to causality *Nat. Rev. Neurosci.* **9** 65–75

[14] Jang B C, Kim S, Yang S Y, Park J, Cha J-H, Oh J, Choi J, Im S G, Dravid V P and Choi S-Y 2019 Polymer Analog Memristive Synapse with Atomic-Scale Conductive Filament for Flexible Neuromorphic Computing System *Nano Lett.* **19** 839–49

[15] Bannur B and Kulkarni G U 2020 On synapse intelligence emulated in a self-formed artificial synaptic network *Mater. Horiz.* **7** 2970–7

[16] La Barbera S, Vuillaume D and Alibart F 2015 Filamentary Switching: Synaptic Plasticity through Device Volatility *ACS Nano* **9** 941–9

[17] Rao T S, Kundu S, Bannur B, George S J and Kulkarni G U 2023 Emulating Ebbinghaus forgetting behavior in a neuromorphic device based on 1D supramolecular nanofibres *Nanoscale* **15** 7450–9

[18] Kozicki M N, Mitkova M and Valov I 2016 Electrochemical Metallization Memories *Resist. Switch.* 483–514

[19] Valov I, Waser R, Jameson J R and Kozicki M N 2011 Electrochemical metallization memories—fundamentals, applications, prospects Nanotechnology **22** 254003

[20] Ohno T, Hasegawa T, Tsuruoka T, Terabe K, Gimzewski J K and Aono M 2011 Short-

term plasticity and long-term potentiation mimicked in single inorganic synapses *Nat. Mater.* **10** 591–5

[21] Fu T, Liu X, Gao H, Ward J E, Liu X, Yin B, Wang Z, Zhuo Y, Walker D J F, Joshua Yang J, Chen J, Lovley D R and Yao J 2020 Bioinspired bio-voltage memristors *Nat. Commun.* **11** 1861

[22] Yan X, Zhang L, Chen H, Li X, Wang J, Liu Q, Lu C, Chen J, Wu H and Zhou P 2018 Graphene Oxide Quantum Dots Based Memristors with Progressive Conduction Tuning for Artificial Synaptic Learning *Adv. Funct. Mater.* **28** 1–10

[23] Milano G, Aono M, Boarino L, Celano U, Hasegawa T, Kozicki M, Majumdar S, Menghini M, Miranda E, Ricciardi C, Tappertzhofen S, Terabe K and Valov I 2022 Quantum Conductance in Memristive Devices: Fundamentals, Developments, and Applications *Adv. Mater.* **34** 2201248

[24] Chekol S A, Menzel S, Ahmad R W, Waser R and Hoffmann-Eifert S 2022 Effect of the Threshold Kinetics on the Filament Relaxation Behavior of Ag-Based Diffusive Memristors *Adv. Funct. Mater.* **32** 2111242

[25] Milano G, Porro S, Valov I and Ricciardi C 2019 Recent Developments and Perspectives for Memristive Devices Based on Metal Oxide Nanowires *Adv. Electron. Mater.* **5** 1800909

[26] Acharyya D, Hazra A and Bhattacharyya P 2014 A journey towards reliability improvement of TiO2 based Resistive Random Access Memory: A review *Microelectron. Reliab.* **54** 541–60

[27] Ahn Y, Shin H W, Lee T H, Kim W-H and Son J Y 2018 Effects of a Nb nanopin electrode on the resistive random-access memory switching characteristics of NiO thin films *Nanoscale* **10** 13443–8

[28] Prezioso M, Merrikh-Bayat F, Hoskins B D, Adam G C, Likharev K K and Strukov D B 2015 Training and operation of an integrated neuromorphic network based on metal-oxide memristors *Nature* **521** 61–4

[29] He W, Huang K, Ning N, Ramanathan K, Li G, Jiang Y, Sze J, Shi L, Zhao R and Pei J 2014 Enabling an Integrated Rate-temporal Learning Scheme on Memristor *Sci.*

Rep. **4** 4755

[30] Liu H, Dong Y, Galib M, Cai Z, Stan L, Zhang L, Suwardi A, Wu J, Cao J, Tan C K I, Sankaranarayanan S K R S, Narayanan B, Zhou H and Fong D D 2022 Controlled Formation of Conduction Channels in Memristive Devices Observed by X-ray Multimodal Imaging *Adv. Mater.* **34** 2203209

[31] Kim D S, Watkins V J, Cline L A, Li J, Sun K, Sugar J D, Fuller E J, Talin A A and Li Y 2023 Nonvolatile Electrochemical Random-Access Memory under Short Circuit *Adv. Electron. Mater.* **9** 2200958

[32] Jeong D S and Hwang C S 2018 Nonvolatile Memory Materials for Neuromorphic Intelligent Machines *Adv. Mater.* **30** 1704729

[33] Sahu D P, Park K, Chung P H, Han J and Yoon T-S 2023 Linear and symmetric synaptic weight update characteristics by controlling filament geometry in oxide/suboxide HfO_x bilayer memristive device for neuromorphic computing *Sci. Rep.* **13** 9592

[34] Yamada N, Ohno E, Nishiuchi K, Akahira N and Takao M 1991 Rapid-phase transitions of GeTe-Sb_2Te_3 pseudobinary amorphous thin films for an optical disk memory *J. Appl. Phys.* **69** 2849–56

[35] Saxena N, Persch C, Wuttig M and Manivannan A 2019 Exploring ultrafast threshold switching in In_3SbTe_2 phase change memory devices *Sci. Rep.* **9** 19251

[36] Kang L and Chen L 2021 Overview of the Role of Alloying Modifiers on the Performance of Phase Change Memory Materials *J. Electron. Mater.* **50** 1–24

[37] Xu M, Mai X, Lin J, Zhang W, Li Y, He Y, Tong H, Hou X, Zhou P and Miao X 2020 Recent Advances on Neuromorphic Devices Based on Chalcogenide Phase-Change Materials *Adv. Funct. Mater.* **30** 2003419

[38] Xu K, Miao X and Xu M 2019 The Structure of Phase-Change Chalcogenides and Their High-Pressure Behavior *Phys. status solidi – Rapid Res. Lett.* **13** 1800506

[39] Zhang W, Mazzarello R, Wuttig M and Ma E 2019 Designing crystallization in phase-change materials for universal memory and neuro-inspired computing *Nat. Rev. Mater.* **4** 150–68

[40] Park S-O, Hong S, Sung S-J, Kim D, Seo S, Jeong H, Park T, Cho W J, Kim J and Choi S 2024 Phase-change memory via a phase-changeable self-confined nano-filament *Nature* **628** 293–8

[41] Marrows C H, Barker J, Moore T A and Moorsom T 2024 Neuromorphic computing with spintronics *npj Spintron.* **2** 12

[42] Kim I-J and Lee J-S 2023 Ferroelectric Transistors for Memory and Neuromorphic Device Applications *Adv. Mater.* **35** 2206864

[43] Song S, Kim J, Kwon S M, Jo J-W, Park S K and Kim Y-H 2021 Recent Progress of Optoelectronic and All-Optical Neuromorphic Devices: A Comprehensive Review of Device Structures, Materials, and Applications *Adv. Intell. Syst.* **3** 2000119

[44] Wang Y, Zhu Y, Li Y, Zhang Y, Yang D and Pi X 2022 Dual-Modal Optoelectronic Synaptic Devices with Versatile Synaptic Plasticity *Adv. Funct. Mater.* **32** 2107973

[45] Xiao W, Shan L, Zhang H, Fu Y, Zhao Y, Yang D, Jiao C, Sun G, Wang Q and He D 2021 High photosensitivity light-controlled planar ZnO artificial synapse for neuromorphic computing *Nanoscale* **13** 2502–10

[46] Khan M U, Abbas Y, Rezeq M, Alazzam A and Mohammad B 2024 Unidirectional Neuromorphic Resistive Memory Integrated with Piezoelectric Nanogenerator for Self-Power Electronics *Adv. Funct. Mater.* **34** 2305869

[47] Ding G, Han S-T, Roy V A L, Kuo C-C and Zhou Y 2023 Triboelectric nanogenerator for neuromorphic electronics *Energy Rev.* **2** 100014

[48] Zhang Y, Zhao H, Chang H, Lyu X, Jing X, Yang W, Xie H and Crittenden J 2023 High-Performance Memristors Based on Bi_2Te_3 *J. Electron. Mater.* **52** 1242–9

[49] Ling H, Koutsouras D A, Kazemzadeh S, van de Burgt Y, Yan F and Gkoupidenis P 2020 Electrolyte-gated transistors for synaptic electronics, neuromorphic computing, and adaptable biointerfacing *Appl. Phys. Rev.* **7** 11307

[50] Leng Y-B, Zhang Y-Q, Lv Z, Wang J, Xie T, Zhu S, Qin J, Xu R, Zhou Y and Han S-T 2023 Recent Progress in Multiterminal Memristors for Neuromorphic Applications *Adv. Electron. Mater.* **9** 2300108

[51] Meng J, Song J, Fang Y, Wang T, Zhu H, Ji L, Sun Q Q, Zhang D W and Chen L 2024

Ionic Diffusive Nanomemristors with Dendritic Competition and Cooperation Functions for Ultralow Voltage Neuromorphic Computing *ACS Nano* **18** 9150–9

[52] Wu Z, Lu J, Shi T, Zhao X, Zhang X, Yang Y, Wu F, Li Y, Liu Q and Liu M 2020 A Habituation Sensory Nervous System with Memristors *Adv. Mater.* **32** 1–9

[53] Xu Y, Liu D, Dai S, Zhang J, Guo Z, Liu X, Xiong L and Huang J 2024 Stretchable and neuromorphic transistors for pain perception and sensitization emulation *Mater. Horiz.* **11** 958–68

Chapter II

Fabrication and Characterization Techniques

In this thesis, neuromorphic devices have been designed to emulate various human-like cognitive activities. To synthesize, characterize, and study these devices, a state-of-the-art laboratory environment equipped with the appropriate tools is required. This chapter provides an overview of the cleanroom facility and the details of the instruments used for the characterization.

Cleanroom fabrication facility

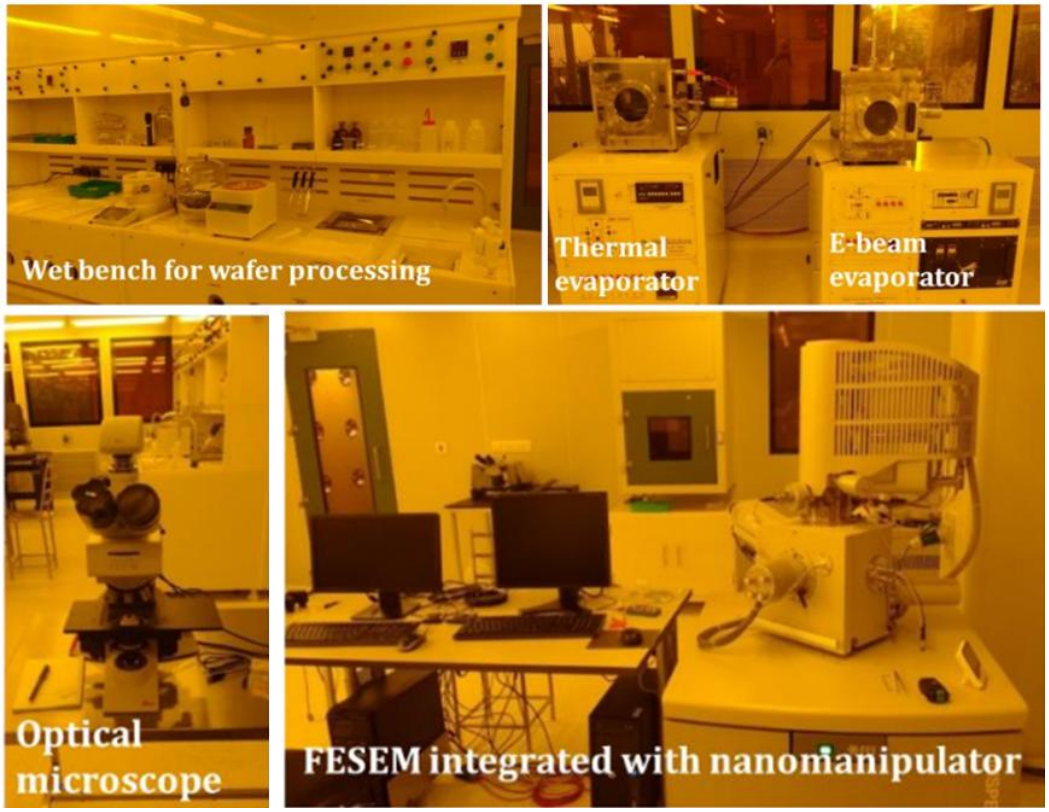

Different fabrication techniques and characterization tools which are discussed below were set up in a class 1000 cleanroom facility. The operation conditions and various fabrication methods were optimized.

Characterization techniques

Scanning electron microscopy (SEM)

SEM was performed using Thermofisher Apreo 2 S. The imaging was performed with low accelerating voltages of 1kV and beam current of 50 pA with the in-lens detector for obtaining high resolution images in high magnification.

SEM equipped with nanomanipulator

The Nova NanoSEM 600, equipped with an integrated nanomanipulator, was employed to meticulously capture the in-situ morphological changes induced by electrical stimulation. The electric bias was applied to the device using Keithley 4200 through the nanomanipulator precisely landed on the Ag nanostructures and the changes were observed in SEM using ET detector.

X-ray diffraction (XRD)

XRD measurements were conducted using a Rigaku diffractometer to analyze the crystalline structure of the samples. The diffraction patterns were recorded over a 2θ range from 10° to 80°, ensuring comprehensive coverage of potential crystal planes for accurate phase identification and structural analysis.

Optical microscope

The optical microscope, Keyence VHX-7000, was used to capture images in both reflective and transmission modes, with a magnification range of 20× to 2000×.

UV-vis spectroscopy

Transmittance measurements were performed using a Perkin-Elmer Lambda 900 UV/vis/NIR spectrophotometer. The UV-Vis spectroscopy was performed in the range of 200-800 nm to measure the transmittance of samples.

Keithley semiconductor characterization system

Electrical measurements of the device were performed using Keithley 4200, 2450, 2461, and 4200A. The Regular I-V and voltage list sweeps were used for generating linear and customized pulse signals.

Temperature-controlled linkam stage

Temperature-dependent measurements were performed using a Linkam temperature stage under a controlled nitrogen atmosphere. The measurements spanned a temperature range from room temperature to 150 K, enabling a detailed investigation of the material's behavior. These measurements were used to assess whether the material exhibited metallic or semiconducting characteristics across the specified temperature range.

Chapter III

Optimized Active Material for Neuromorphic Device Fabrication: Emulating Ebbinghaus Forgetting of Associative Learning

Summary

In this study, a self-formed dewetted silver (Ag) active material was optimized for neuromorphic applications. A two-terminal device incorporating this optimized material was fabricated, exhibiting resistive switching behavior due to the migration of Ag under an electric field. The device's conduction was confirmed through low-temperature variation studies of the low resistance state (LRS), and in-situ field emission scanning electron microscopy (FESEM) studies provided visual evidence of filament formation. The neuromorphic device successfully mimicked synaptic functionalities such as short-term plasticity (STP) and long-term plasticity (LTP). Additionally, the device demonstrated associative learning through the application of voltage pulses and, for the first time, emulated the forgetting of associative learning, following the Ebbinghaus forgetting curve, which describes the pattern of human memory decay.

III.1 Introduction

In the contemporary period of swift technological advancement, there is an unprecedented need for high-performance computing systems[1,2]. Due to their intrinsic limitation of bandwidth and energy efficiency, traditional von Neumann architectures are becoming insufficient. The speed of data transfer between memory and the central processing unit (CPU) becomes a major barrier due to these limitations, resulting in the von Neumann bottleneck[3]. Computing architectures that can handle big data with speed and precision are required, while minimizing energy consumption since artificial intelligence and machine learning are becoming increasingly complex and current computing systems are at their limits[4].

Neuromorphic devices which are inspired by the brain have emerged as one of the possible solutions to overcome these issues. By replicating the neural architecture and functionalities of the human brain, neuromorphic technologies provide a paradigm shift from traditional computing approaches[5]. The human brain is remarkably efficient in carrying out complex activities like pattern recognition, learning, and decision-making with very minimal energy usage[6,7]. The presence of a million neurons with a billion

synaptic connections among them is responsible for the efficient computing and cognitive abilities of the brain[8]. The neuromorphic devices aim to mimic the basic synaptic functionalities such as spiking behavior, short-term plasticity (STP), long-term plasticity (LTP), and various others. Along with the basic synaptic functionalities these devices have also emulated a few cognitive behaviors[9,10]. Various types of neuromorphic devices have been reported based on their mechanism including electrochemical metallization (ECM) or electromigration, valence change memory (VCM), phase-change memory (PCM), etc[11,12]. Among these, ECM-based neuromorphic devices have drawn a lot of attention due to their high switching rates, low-power consumption, and excellent scalability[13]. Also, these devices exhibit plasticity and have emulated intricate tasks like pattern recognition and associative learning, which are essential for learning processes[14]. Their capacity to replicate such complex neural processes highlights their potential in furthering neuromorphic computing and creating more effective and powerful AI systems processes. The functioning of these devices involves the formation of dissolution of metallic filaments within a dielectric media when subjected to the electrical field[15]. Various ECM-based devices have reported emulation of plasticity behaviours such as short-term plasticity (STP), long-term potentiation (LTP) and spike-time dependent plasticity (STDP)[15]. The neuromorphic devices have also demonstrated the emulation of cognitive behavior, such as classical conditioning with the use of external stimuli. Classical conditioning, a foundational psychological experiment conducted by Pavlov in 1897, is considered to be the benchmark study in neuromorphic devices. Pavlov's experiment involved training his dog to come for the food (unconditioned stimulus) by hearing the ringing bell (conditioned stimulus). During the training, he started ringing the bell while feeding him, which associated the bell signal with the food signal. Through repeated pairings of the bell and the food, the dog learned to salivate at the sound of the bell alone. This is one of the common cognitive behaviors observed in biological systems called classical conditioning[16]. Few articles report the mimicking of associative learning using the device. Table III.2 in the discussion lists the neuromorphic devices based on both ECM and VCM mechanisms, which have successfully emulated associative learning. The associative learning is also emulated using optically activated neuromorphic devices[17–20]. The emulation of associative learning using both electrical and optical inputs such as food and bell is also reported by using one of these devices[21,22]. Ji. *et al.* utilize the mechanical input as a food signal and the optical input

as a bell signal to mimic classical conditioning by integrating a pressure sensor with the device[23]. In another case, Wan. *et al.* have used the optical inputs as food and the auditory input as the bell to show the association by integrating an acoustic sensor[24]. However, none of these reports discusses the forgetting of such complex cognitive learning. Learning and forgetting are the two important characteristics of the brain where learning allows us to acquire new knowledge while forgetting clears unused or outdated information to make a way for new learning[37]. So, the study of forgetting is equally important when associative learning is involved.

Alongside the mechanism of operation, active material also plays a vital role in the functioning of a neuromorphic device as the property of the active material is altered using electrical stimuli. The active material should be dynamically reconfigurable and adaptive to the variety of inputs akin to synaptic connections in the human brain. Compared to the real neural networks the self-formed materials also can form the networks independently. The ability of self-formed networks to support the development of distinct neural masses results in variable plasticity, which is necessary for complex brain processing.

Herein, the ECM mechanism is combined with a self-formed structure. Thus, extracting the advantages of both and also closely mimicking the biological neural network through the mindful design of the active material. The work shows the optimization of the dewetted Ag active material for neuromorphic applications. The active material is optimized after studying the role of temperature and time during the dewetting process. After optimizing the active material, a two-terminal neuromorphic device containing self-formed dewetted Ag as the active material was fabricated. The device fabrication process is simple, scalable and cost-effective. The application of the voltage triggers the migration of Ag across the gaps leading to the threshold-switching behavior of the device. The device emulates synaptic functionalities such as threshold switching, STP, and LTP. The device also illustrates associative learning using voltage pulses. Along with associative learning, the device also demonstrates the forgetting of associative learning, which is not reported in the literature.

III.2 Scope of the present investigation

The scope of this chapter lies in the optimization of a novel neuromorphic device based on a self-formed dewetted Ag active material, which addresses the limitations of traditional von Neumann architectures. The study aims to highlight the advantages of combining electrochemical metallization (ECM) with a self-formed structure to closely replicate the biological neural networks. The research work focuses on understanding the role of temperature and time during the dewetting process to optimize the active material. The resulting device mimics the cognitive process of associative learning and its subsequent forgetting to demonstrate essential synaptic behaviors such as STP and LTP. This work contributes to the field of neuromorphic computing by offering a simple, scalable, and cost-effective fabrication process for advanced neuromorphic devices, paving the way for more efficient and powerful artificial intelligence systems.

III.3 Experimental details

A cleaned glass slide of dimension 2 × 2 cm^2 was taken, and an Ag film of thickness 30 nm was deposited using an e-beam evaporator at a pressure of 10^{-6} torr. The deposited substrate was heated at 300 °C in the ambient for 30 s which led to dewetting to form nanostructured Ag islands. Finally, two Au contact pads having 100 µm gap were deposited using thermal evaporation. Optical microscopy images of the device were collected using a Keyence microscope (VHX 7000). To visualize the morphology of Ag nanostructures, a field emission scanning electron microscope (FESEM) (Thermofisher Apreo 2 S) was employed. All the electrical characterizations were performed in Keithley 2450 and Keithley 2461. The temperature-dependent resistance measurement was done using the Linkam temperature stage. The fill factor of the Ag nanostructures was calculated using ImageJ software.

III.4 Results and discussion

III.4.1 Optimization of active material for neuromorphic applications

The active material plays a crucial role in the functioning of the neuromorphic devices. Herein, as the first step, the active material was optimized in order to fabricate a neuromorphic device. The active material is formed by subjecting Ag film to thermal stress. Specifically, 30 nm Ag is deposited on a glass slide using an e-beam evaporator. A few Ag films were taken and subjected to thermal treatment at various temperatures. The

dewetting was performed at temperatures ranging from 130 °C to 400 °C on a pre-heated hotplate (Figure III.1).

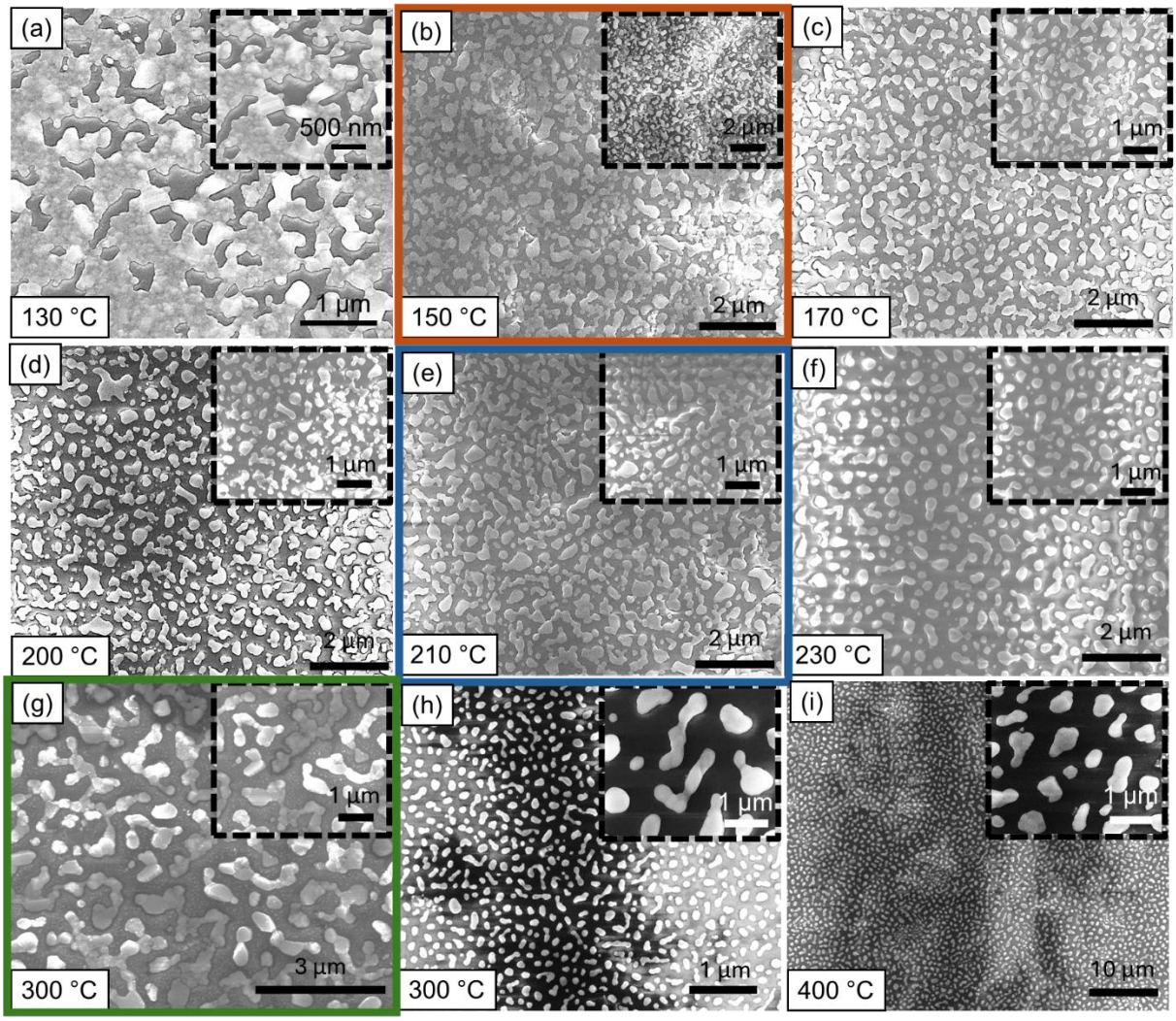

Figure III.1: Low and High-magnification images of a 30 nm dewetted Ag film at (a) 130 °C for 1 hour, (b) 150 °C for 25 minutes, (c) 170 °C for 12 minutes, (d) 200 °C for 3 minutes, (e) 210 °C for 1 minute 30 seconds, (f) 230 °C for 1 minute, (g) 300 °C for 30 seconds, (h) 300 °C for 1 minute, (i) 400 °C for 20 seconds. Insets show high-magnification images of the same region. The square color boxes represent the dewetted substrates taken for device fabrication.

When the film exhibited a color change, showing significant transformation due to heating, the substrate was promptly removed from the hotplate and placed on a cold surface. The film dewetted at a temperature of 130 °C maintained for 1 hour, resulting in the rupture of Ag film and forming a long chain of Ag nanostructures, while still preserving good connectivity within the Ag film (Figure III.1a). When the temperature is slightly increased to 150 °C, the film transforms into a disconnected network of Ag nanostructures within a time frame of 20 minutes (Figure III.1b). This indicates that the

increase in temperature can accelerate the dewetting process and lead to the formation of nanoscale features. Similarly, the solid-state dewetting was performed at several temperatures 170 °C (Figure III.1c), 200 °C (Figure III.1d), 210 °C (Figure III.1e), and 230 °C (Figure III.1f), resulting in Ag nanostructures. This indicates that a modest increase in temperature can lead to the formation of nanoscale features. However, the dewetting at higher temperatures, such as 300 °C (Figure III.1g,h) and 400 °C (Figure III.1i) results in the formation of spherical particles within 1 minute. The solid-state dewetting of Ag thin film leads to the formation of disconnected Ag structures, starting from the ruptures in the film[38]. These voids start to grow with time, and the film breaks into irregularly shaped nanostructures. However, further increase in temperature results in the separated metal nanostructures. At this point, the film loses its connectivity over a larger area. Finally, the additional treatment of heat leads to the formation of spherical particles. The dewetting process strongly depends on both the temperature and the time of the dewetting to produce Ag nanostructures and particles. The dewetting process is driven by the minimization of the total energy of the film, the interface energy, and the substrate-free energy[39,40].

The FESEM images were further analysed using ImageJ software for the fill factor calculations, a measure of surface coverage of Ag. The dewetting at low temperatures shows a higher coverage of Ag, resulting in a fill factor of 77.5% (Figure III.2a). In contrast, the fill factor reduced to nearly 50% for the 210 and 300 °C (Figure III.2b-c). This reduction in fill factor at higher temperatures indicates more extensive breaking up of Ag film into smaller structures, reducing the overall surface coverage. The dewetting at 400 °C produces spherical particles, resulting in 33% surface coverage only (Figure III.2d). The ability to control parameters such as temperature thus allows tuning of different structures. Table III.1 highlights the FF comparison of all the substrates heated at various conditions.

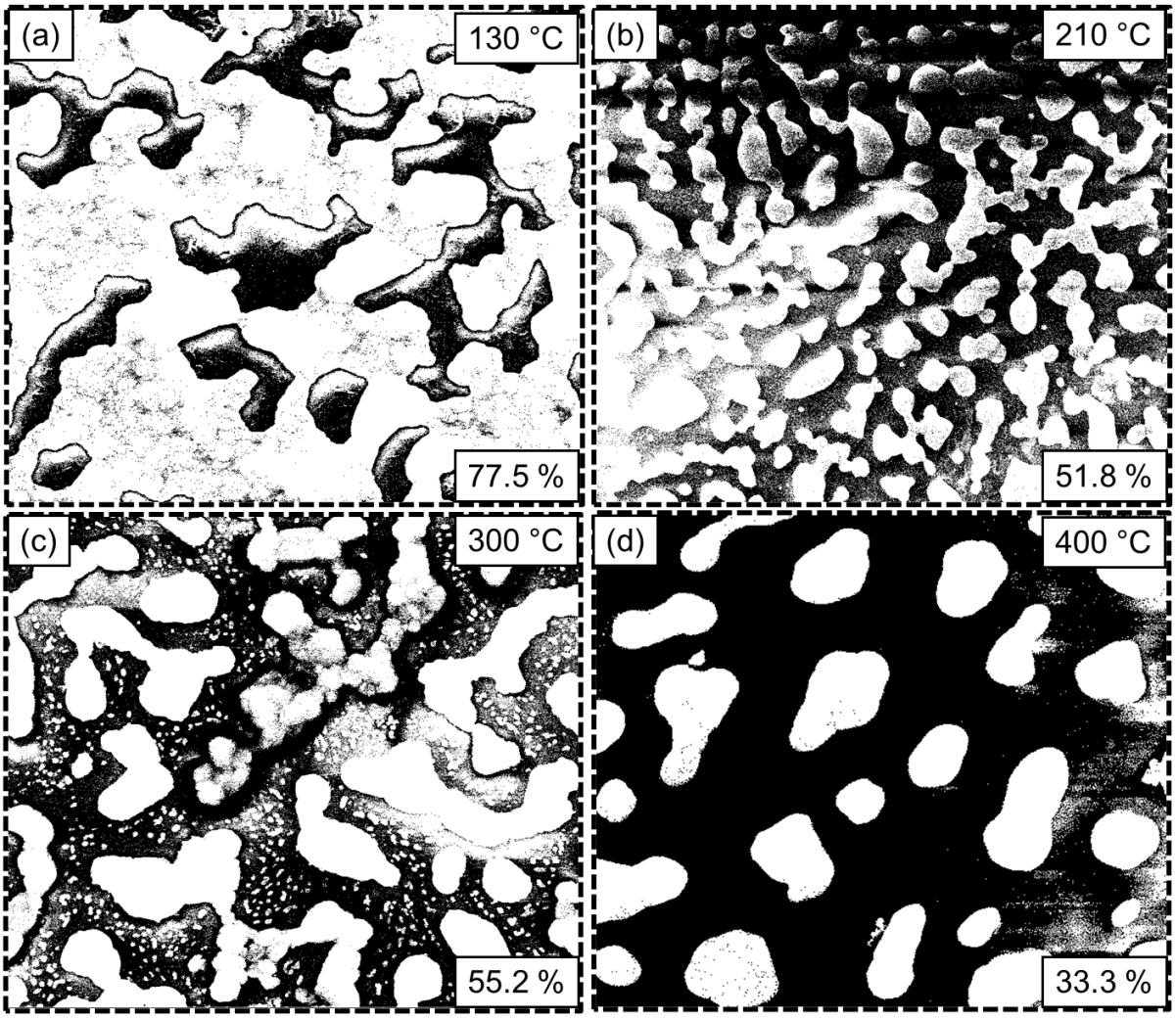

Figure III.2: The ImageJ analysis highlighting the fill factor of the film dewetted at (a) 130 °C (b) 210 °C (c) 300 °C and (d) 400 °C.

Table III.1: Fill factor of dewetted Ag film at various dewetting temperatures and time.

Temperature	Time	Average FF
130	1 hr	77.03
150	**25 min**	**53.3**
170	12 min	48.4
200	3 min	43.4
210	**1 min 30 s**	**46.9**
230	1 min	45.0
300	**30 s**	**55.9**
300	1 min	35.6
400	20 s	34.9

The previous work from our group utilizes the dewetted Ag to fabricate a neuromorphic device to perform plasticity behavior[36,41]. However, the optimization of the active element to show such memory behavior was not discussed. After investigating the dewetting behavior and the formation of active material, the films with better dewetting conditions such as those with hierarchical nanostructures, lesser but desirable distance between the nanostructures and uniform films were chosen and three devices were fabricated by depositing the Au electrodes on top of the dewetted Ag nanostructures.

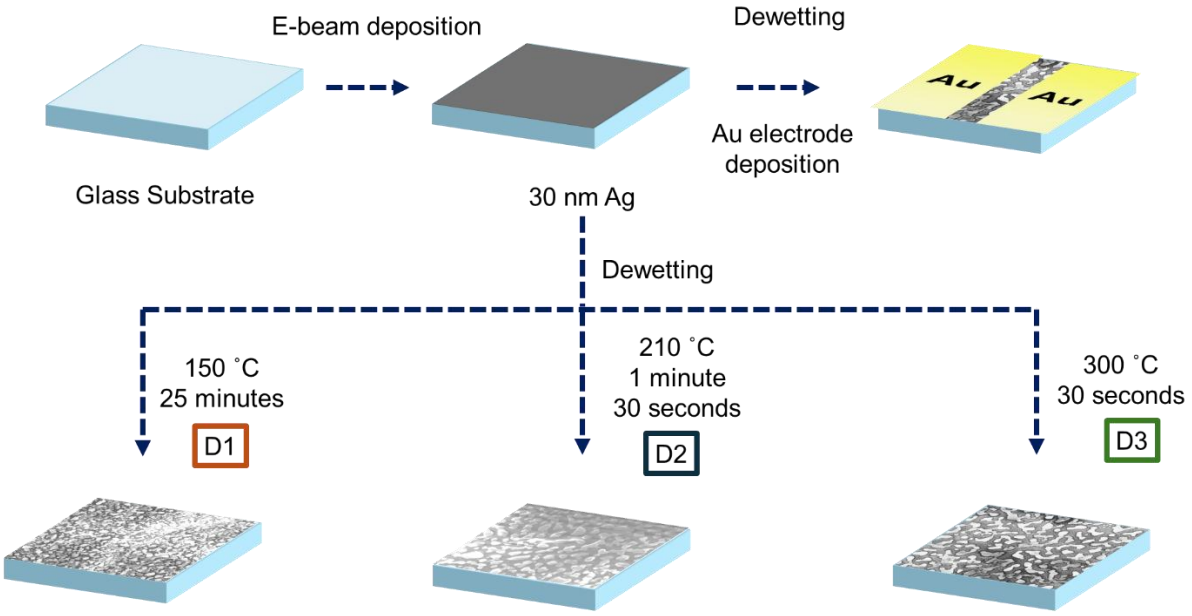

Figure III.3: Schematic illustrating the fabrication of devices D1, D2 and D3.

The devices were categorized based on their dewetting conditions as follows: D1 (substrate dewetted at 150 °C for 25 minutes), D2 (substrate dewetted at 210 °C for 1 minute 30 seconds), and D3 (substrate dewetted at 300 °C for 30 seconds). The device fabrication process is schematically illustrated in Figure III.3. In each device, the dewetted Ag nanostructures are positioned between the two Au electrodes having a gap of ~ 100 µm.

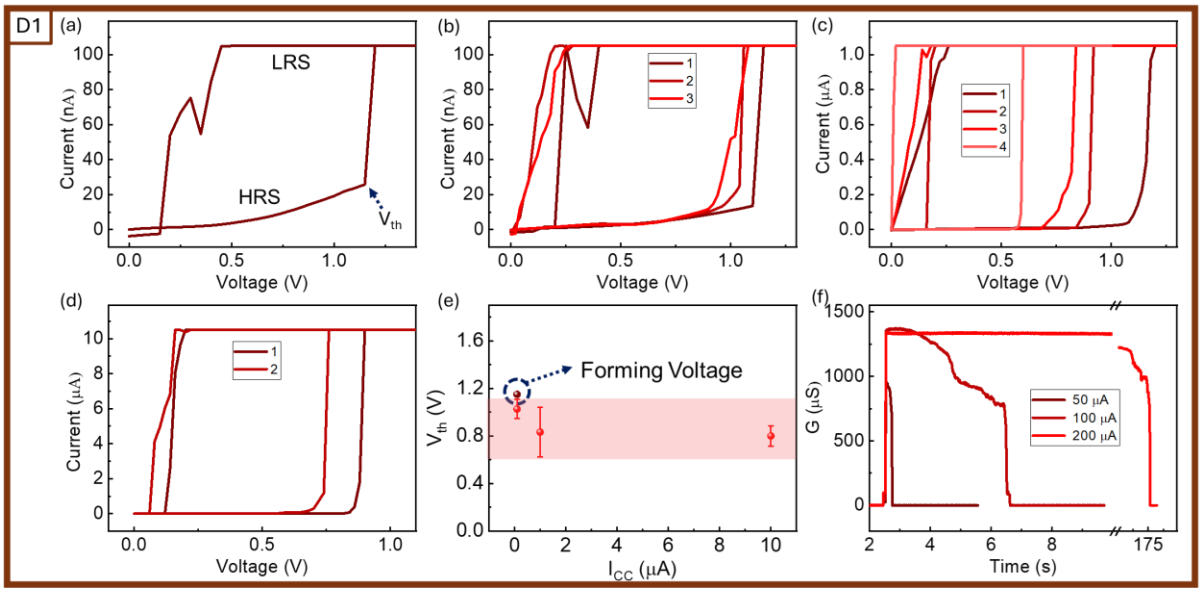

Figure III.4: Electrical characterization of device D1 (a) I-V sweep exhibiting threshold switching reporting forming voltage around 1.1 V. Consecutive I-V sweeps at set I_{CC} of (b) 100 nA (c) 1 μA and (d) 10 μA. (e) Variation of V_{th} with the set I_{CC}. (f) STP to LTP transition by varying I_{CC} using voltage pulses.

The devices initially exhibit very high resistance, typically in the range of several MΩ due to the disconnected Ag nanostructures between the two Au electrodes which is called the high resistance state (HRS). Therefore, this high resistance is a result of the interrupted pathways for electron flow between the Au electrodes. However, when a voltage sweep is performed on device D1, a sharp transition in device current is observed upon reaching a certain threshold known as threshold voltage (V_{th}) transitioning to a low resistance state (LRS) (Figure III.4a). This sharp increase in current indicates that the device switches from its initial HRS to a LRS. This behavior is characteristic of the threshold-switching behavior of the device, where the application of a sufficient voltage causes the device to transition to a significantly more conductive state. This threshold-switching behavior underpins the potential of these devices for use in resistive switching applications. The V_{th} recorded during the first I-V sweep on a pristine device is known as the forming voltage of the device. This forming voltage represents the initial voltage required to induce a transition from HRS to LRS in the device. While sweeping back the device returns to its initial HRS, confirming the volatile switching behavior of the device. Also, it attains a pinched hysteresis loop similar to memristors, which shows the memory behavior of the device. To understand the behavior of the device under different conditions, the I-V sweeps were consecutively performed at different current compliance (I_{CC}) to observe the variation of the V_{th}. The V_{th} value was observed to be ~1 V at 100 nA, which shows a slight

shift at higher I_{CC} values. This indicates that the device shows stable V_{th} characteristics across a range of current compliances Figure III.4b-d shows the consecutive I-V loops at 100 nA, 1 μA, and 10 μA, respectively. The V_{th} value plotted against the set I_{CC} reveals minimal variation in V_{th} (Figure III.4e). This consistency is crucial for reliable device performance, ensuring predictable switching behavior regardless of I_{CC} setting. Additionally, the forming voltage was found to be close to the V_{th} values, which shows the forming free switching in the device. This proximity indicates that the device does not require a significantly higher initial voltage to switch into the LRS. The application of the electric field across the gaps triggers the electromigration of Ag, which establishes a conducting path across the two Au electrodes[42]. The formation of the conducting path is responsible for the resistive switching in the device. These conducting path or filaments tends to relax after the removal of the applied bias which explains the return to the HRS. The migration of Ag with the applied electric field has been studied previously[43,44]. The experimental characterization to support the conduction mechanism will be discussed later.

The retention of the current while sweeping back hints at the plasticity behavior of the device. To investigate such behavior precisely, voltage pulses were employed. The device was subjected to a single voltage pulse of amplitude 2 V and the response to the pulse was monitored using a reading voltage (V_R) of 100 mV to accurately measure changes in conductance. The conductance of the device significantly enhanced in response to the voltage pulse. Figure III.4f shows the variation of conductance of the device after the application of the voltage pulse which shows that the conductance state was retained even after the application of the pulse. This change indicates that the device's resistance decreased in response to electrical stimulus, reflecting a shift to a more conductive state. Notably, this elevated conductive state was maintained, showing the device's ability to hold a state temporarily without continuous stimulus. The experiment showed that the device's conductance can be modulated by voltage pulses. The voltage pulse was applied with different I_{CC} including 50 μA, 100 μA and 200 μA. The device reverts to its initial state within 2 seconds at 50 μA set I_{CC}. Meanwhile, it retains the conductance for ~ 6 seconds at 100 μA I_{CC}. A further increase in I_{CC} leads to an enhanced conductance retention of ~ 3 minutes. The retention of conductance at different I_{CC} illustrates the two important characteristics of the neuromorphic devices known as short-term plasticity (STP) and long-term potentiation (LTP)[45,46]. These are akin to short-term memory and long-term

memory of the biological systems. Also, according to the Atkinson-Shiffrin multi-store memory model in biological systems, any information perceived by a human initially enters sensory memory[47]. Based upon the rehearsal or the repetition of the information it can form either a short-term or long-term memory. In a similar manner, our device demonstrated a transition from short-term to long-term plasticity by varying the I_{CC} in the device. When the set I_{CC} was increased to 200 µA, a transition from STP to LTP was observed with the retention of the conductance state close to 3 minutes. The filaments become more consolidated and stronger at higher compliance to allow more current to flow which leads to the stabilization of the V_{th} in a narrow range.[48] Also, a denser filament takes a longer time to relax back which leads to a longer retention. The device successfully demonstrated threshold switching and plasticity behavior similar to the human brain.

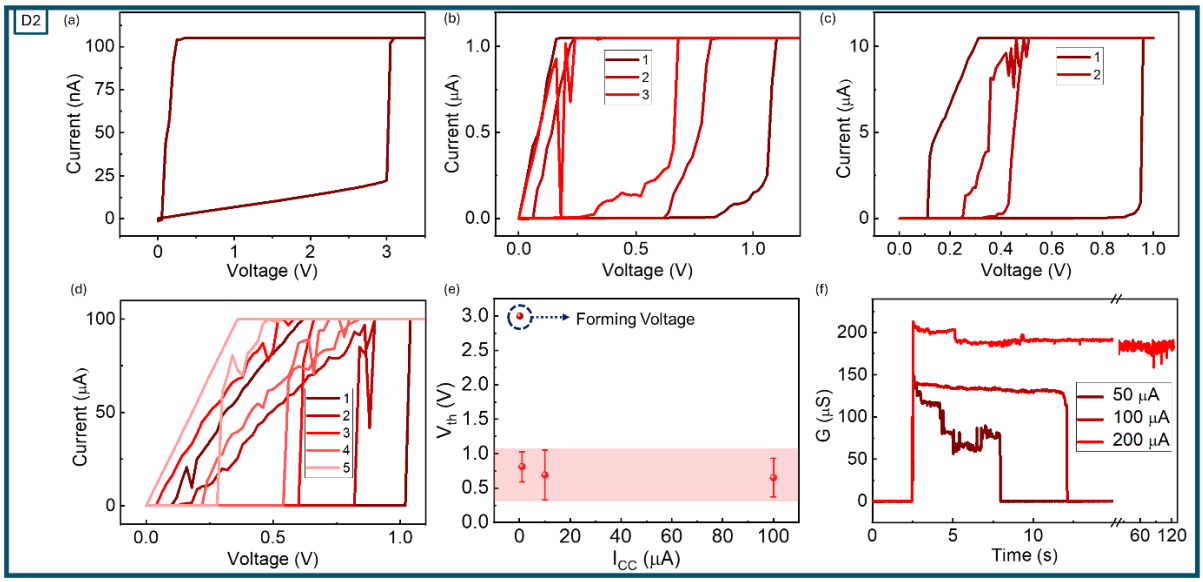

Figure III.5: Electrical characterization of device D2 (a) I-V sweep exhibiting threshold switching reporting forming voltage around 3 V. Consecutive I-V sweeps at set I_{CC} of (b) 1 µA, (c) 10 µA and (d) 100 µA. (e) Variation of V_{th} with the set I_{CC}. (f) STP to LTP transition by varying I_{CC} using voltage pulses.

After examining resistive switching in device D1, device D2 was taken for detailed electrical characterization. It also exhibits a resistive switching, which is observed during an I-V sweep (0-3 V) at a set I_{CC} (Figure III.5a). Upon voltage application in a pristine device, the device switches to a LRS around 3 V confirming it as forming voltage. To further investigate, consecutive I-V sweeps were performed at various I_{CC} to observe the threshold switching variation in relation to the set I_{CC} (Figure III.5b-d). Remarkably, the I-V sweep performed at higher I_{CC} (1 µA) shows a threshold switching below 1 V (Figure

III.5b). Figure III.5e shows that device D2 requires a higher forming voltage while V_{th} shows minimal variation at different I_{CC}. Furthermore, to investigate the STP and LTP behavior of device D2, it was subjected to a single voltage pulse of amplitude 2 V having both width and interval of 50 ms with a reading voltage (V_R) of 100 mV. The device shows a similar behavior as device D1, showing STP behavior at 50 and 100 µA of I_{CC} while transitioning to LTP at 200 µA.

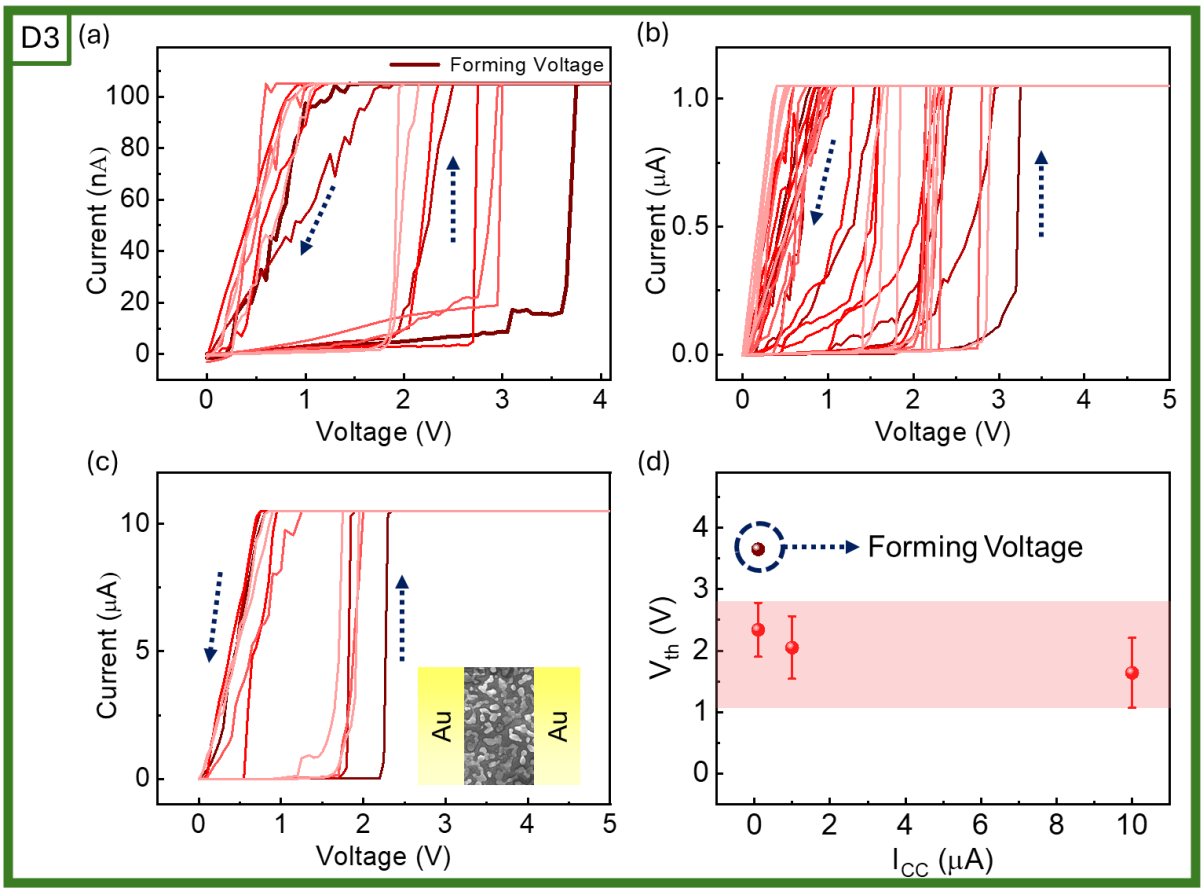

Figure III.6: Electrical characterization of device D3 (a) I-V sweep at 100 nA I_{CC} exhibiting threshold switching reporting forming voltage around 3.6 V. Consecutive I-V sweeps at set I_{CC} of (b) 1 µA and (c) 10 µA. Inset in (c) shows the device schematic. (d) Variation of V_{th} with the set I_{CC}.

Similar studies were performed on the device D3 as shown in Figure III.6. As previously observed, the threshold switching behavior of the device has emerged during the I-V sweep. The I-V sweep at 100 nA I_{CC} on a pristine device confirms the forming voltage to be ~ 3.65 V (Dark brown curve in Figure III.6a). The consecutive I-V sweeps at I_{CC} of 100 nA (Figure III.6a), 1 µA (Figure III.6b) and 10 µA (Figure III.6c) were performed to check the cyclic variation of the V_{th}. The switching threshold was found to be reduced below 2 V at higher I_{CC} values. The average V_{th} calculated from the figure was plotted against the I_{CC}, which shows a slight decrement in threshold voltage as I_{CC} increases (Figure III.6d).

As explained earlier, at higher I_{CC} the filaments become more consolidated and thicker, leading to decrement in V_{th}.

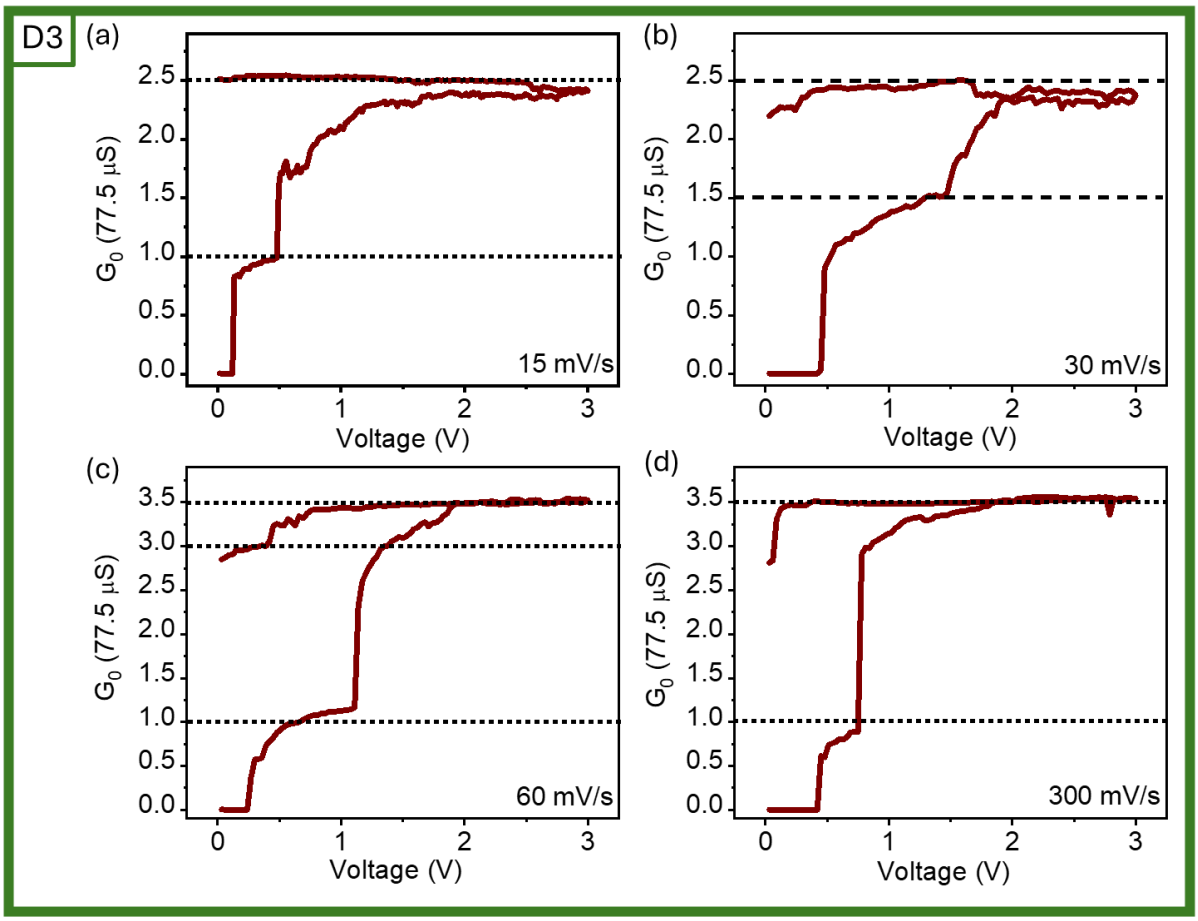

Figure III.7: The change in the conductance of the device during voltage sweep results in the discrete jumps corresponding to the quantum point contact (77.5 µS). The quantum conductance plateaus behavior at a sweep rate of (a) 15 mV/s (b) 30 mV/s (c) 60 mV/s and (d) 300 mV/s.

While performing I-V sweeps in the device during the change of resistance states from HRS to LRS few sudden jumps were observed. To investigate this, the voltage sweep was performed at different sweep rates, and their conductance was monitored. Surprisingly, rather than a gradual increase, the conductance was found to be enhanced in discrete steps. These conductance jumps occur when the length of the conducting filament becomes comparable to the mean free path of the electrons. In such cases, the electronic transport shifts from diffusive to ballistic, due to which the quantum point contact is formed by the conducting filament[49]. The occurrence of integer and half-integer quantum conductance states has been observed in the devices using Cu and Ag as electrochemically active material. [50–52].

These jumps are very well studied and explored in metallic systems and are called quantum conductance jumps. The occurrence of these jumps was modulated using the sweep rate in the device. The device while sweeping at a low sweep rate (15 mV/s and 30 mV/s) illustrates few half-integer and integer quantum conductance states including 1 G_0, 1.5 G_0, and 2.5 G_0 (Figure III.7a-b), where G_0 is conductance quantum. In quantum conductors, conductance is quantized and occurs in discrete form rather than continuous. Meanwhile, at higher sweep rates (60 mV/s and 300 mV/s) the quantum conductance states 1 G_0, 3 G_0, and 3.5 G_0 were observed (Figure III.7c-d). Surprisingly, at a higher sweep rate, few states including $2G_0$, were found to be missing. The conductance states could be missing due to the large migration of Ag at higher sweep rates making a sharp increase in conductance.

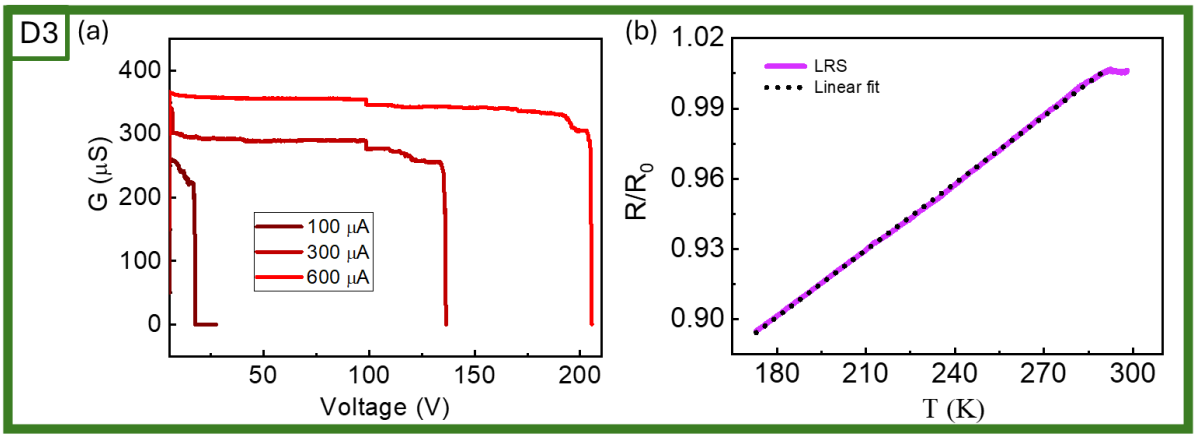

Figure III.8: (a) STP and LTP behavior in device D3. (b) The variation of LRS with temperature indicates metallic filament formation.

The device D3 was also thoroughly investigated to show STP and LTP behavior using the voltage pulses. The device shows clearly the transformation of STP to LTP with an increase in I_{CC} from 100 µA to 600 µA (Figure III.8a). The device retention was found to be 10 s, 130 s, and 200 s at I_{CC} of 100 µA, 300 µA, and 600 µA respectively. This progression shows that higher I_{CC} values increase retention. As compared to devices D1 and D2, the forming voltage was found to be a little higher in device D3. Also, a higher I_{CC} was required in device D3 to achieve the LTP state. These differences show that D3 shows distinct electrical properties, due to variations in its fabrication. Comparing the forming and threshold voltages of the devices, devices D1 and D2 had lower threshold voltages (around 0.5 to 0.6 V), which could limit the dynamic range of the device's operation. Therefore, Device D3, with its higher threshold voltage, was selected for further studies.

To investigate the conduction mechanism behind such behavior in device D3, it was potentiated at higher I_{CC} using 20 pulses of 2 V, resulting in an LTP state or the potentiated state. While the device was in the LRS state, the substrate temperature was varied from room temperature to -125 °C and the corresponding change in resistance was monitored (Figure III.8b). The resistance decreases linearly with the temperature change. The resistance variation was fitted with the following equation:

$$R = [\,1 + \alpha\,(T - T_0)]\,R_0 \qquad (1)$$

Where R (T) is the resistance as a function of temperature, R_0 is the resistance at room temperature, T_0 and α represents the temperature coefficient of resistance (TCR). The decrement of resistance with temperature confirms the metallic conduction in the device during LRS conduction.

With linear curve fitting, using equation 1 in $y = mx + c$, the slope (m) gives the value of the TCR. The experimental calculated value of TCR was found to be 0.001 K^{-1}, slightly lower than the bulk value which can be expected for a disordered system[53].

To get a better understanding of the mechanism involved in threshold switching and other behaviors experimentally, in-situ FESEM was employed. This technique helped in understanding morphological changes within the device. A specific region close to the Au electrode was identified using the FESEM to observe the morphological changes in the device under the application of voltage (III.9a). One of the probes was kept on an Au electrode while the other probe was placed in the active region containing dewetted Ag (Figure III.9a). This set up facilitated direct observation of changes in the nanostructures with applied electric field. A voltage bias of 20 V was applied across the gap between the probes, and FESEM images were compared before and after the applied bias. The morphology change is observed in the encircled region in Figure III.9b image. The zoomed-in image in the inset confirms the trace of the migrated Ag across the gap in the direction of the field. However, the changes were only spotted in a single place. A bias of higher amplitude (50 V) was applied to drive more migration, and the morphology fluctuations were recorded (Figures III.9c-d). The FESEM images in Figure III.9c show the FESEM image of the region before bias with some zoomed-in regions. The morphology changes after the applied bias are shown in Figure III.9d where the zoomed-in FESEM images highlight the traces of the filaments observed at three different locations. The

formation of a conductive pathway under the influence of an electric field corroborates with the observation of transformation from HRS to LRS upon crossing a specific threshold voltage.

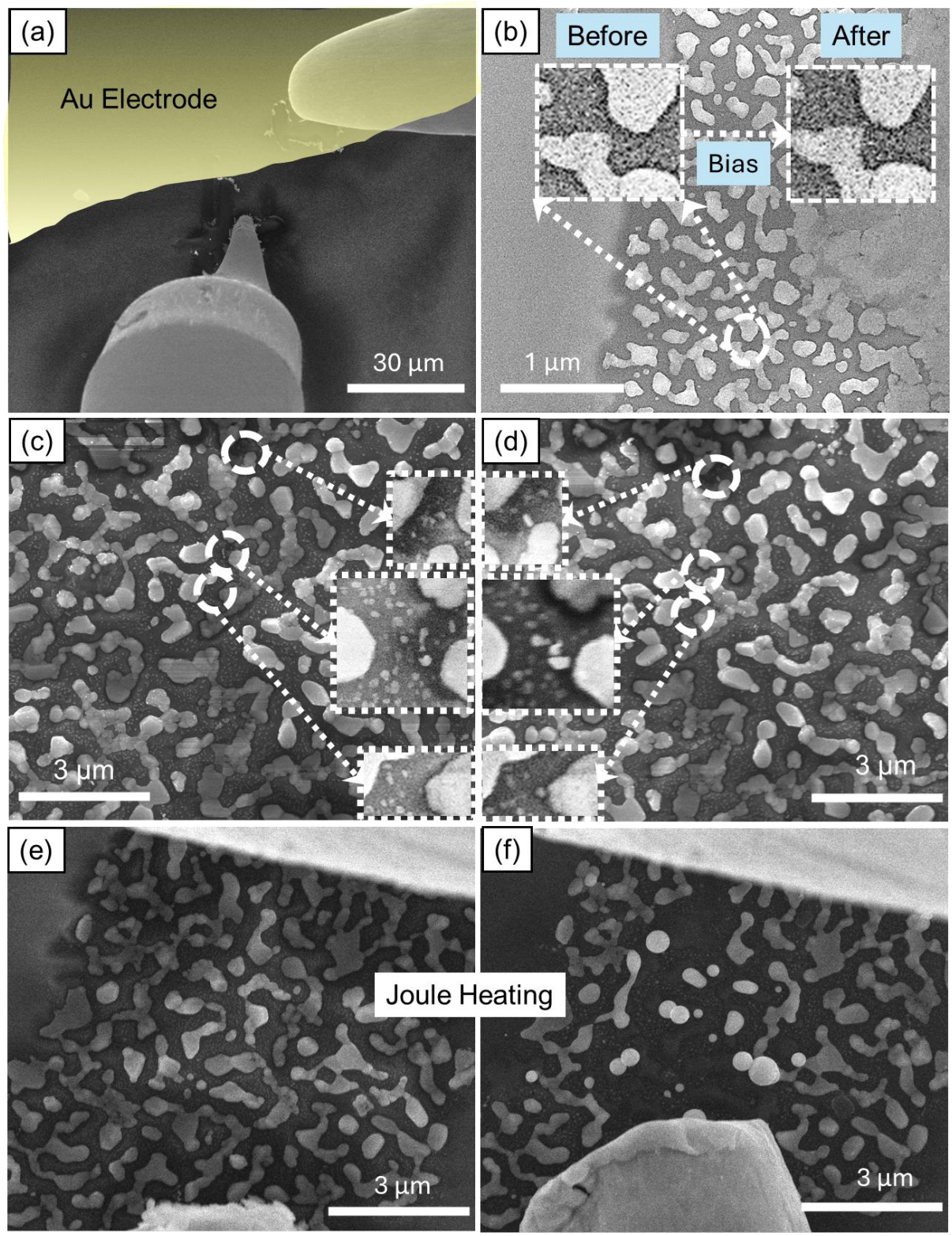

Figure III.9: In-situ FESEM study (a) Nanofinger and nanoprobe were placed on Au electrode (highlighted by golden colour) and active material (Ag) on a micro-scale region.

(b) High-magnification FESEM image showcasing the Ag islands. Inset images show the zoomed-in view of the encircled region before and after the application of 20 V bias. (c) FESEM image depicting the traces of filaments in the device subjected to 50 V sweep. Insets show the zoomed-in image of filament traces. (d) FESEM image showcasing the joule heating effect on the Ag nanostructures after application of 50 V bias at a higher I_{CC} value.

However, the current flowing across these conducting filaments may lead to joule heating at higher I_{CC} values. A 50 V bias was applied at a higher I_{CC} in the device and the FESEM images before and after the bias application were captured (Figure III.9e-f). Surprisingly, the area where localized Ag islands (Figure III.9e) were found to be ruptured and coalescence occurred simultaneously, as shown in Figure III.9f. The comparison images confirm the possibility of the joule heating in the device at higher I_{CC} values. The in-situ FESEM images provide the traces of the Ag filaments across the gaps. The application of the voltage triggers the filament formation across these gaps to form a conduction path between the two electrodes resulting in the threshold switching of the device. The enhanced understanding of filament evolution helps in the characterization of the device's performance and reliability. The temperature variation of the LRS and the in-situ FESEM studies confirm the formation of metallic filaments across the electrodes upon the application of bias across the device.

After successfully demonstrating the basic neuromorphic functionalities such as threshold switching, STP, and LTP, the device was utilized to mimic one of the cognitive behaviors, classical conditioning. The experiment focused on replicating the associative learning process observed in biological systems using voltage pulses as stimuli. Figure III.10a schematically illustrates the classical conditioning process where a dog is shown to salivate in response to the bell after training with a ringing bell in the presence of food. In the device, the food and bell signals were strategically assigned as 2 V and 0.5 V, respectively. As the food signal represents an unconditioned stimulus, the response is expected, so the voltage amplitude was chosen above the V_{th} of the device. Meanwhile, the bell signal amplitude is below V_{th} as a conditioned stimulus is not expected to generate a response before training. The application of a food signal (2 V) generated a measurable response in the device (Figure III.10b). This response could be considered analogous to the salivation by the dog while observing food. Meanwhile, the bell signal (0.5 V) could not generate any response (Figure III.10c).

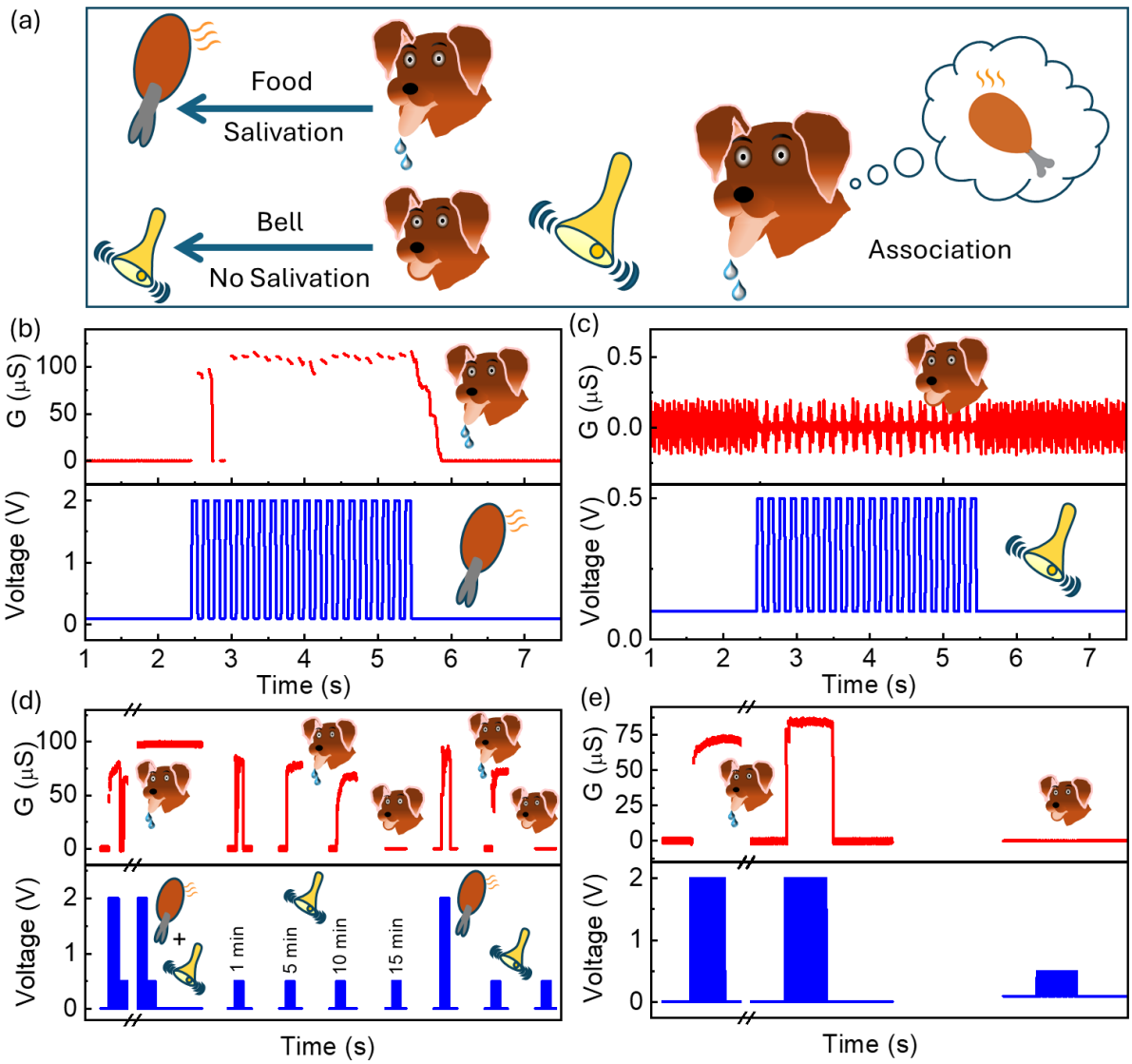

Figure III.10: (a) Schematic illustrating dog salivating for food and not for the bell before association (left); salivating for ringing bell after association (right) (b) Response of the device showing higher conductance for the 2 V food pulses. (c) No response (no conductance change) for 0.5 V bell signal. (d) Classical conditioning is emulated using 2 V (food) and 0.5 V (bell) signals with 10 sets of training. (e) No response for the bell was observed after the complete dissociation of the conditioning by training with food pulses alone.

The next included training the device with the application of food and bell signals together using 2 and 0.5 V pulses. During the training, the device generated an expected response (Figure III.10d). Surprisingly, 0.5 V pulses (bell signal) could generate a response after the training. The training in the device using two different signals is similar to the ringing of the bell while feeding the dog for the association. The device could generate a response with a 0.5 V which was not observed before training, is analogous to dog salivation to the bell ringing. The device successfully created an association between an unconditioned stimulus (2 V) and a conditioned stimulus (0.5 V), demonstrating

classical conditioning. The application of the bell signal alone without the application of the food signal leads to the dissociation of the signal. The response for the bell signal was observed at regular intervals, which shows that the response diminishes after 15 minutes (Figure III.10c). This could be due to the dissociation of the bell signal with time which is well-studied in psychology. However, the response could be regenerated using a food signal before the application of the bell signal. The food signal acts as a treat which creates a response for the bell signal next time in the hope for food. However, as every learning decays over time, the bell signal also decays at last. Further training will be required to get a response. To validate the association, 10 sets of food signals (similar to the number of sets applied during association training) were applied, and the response for the bell signal was monitored (Figure III.10e). No response was observed for the bell signal which shows that the association was created using simultaneous training of food and bell signals.

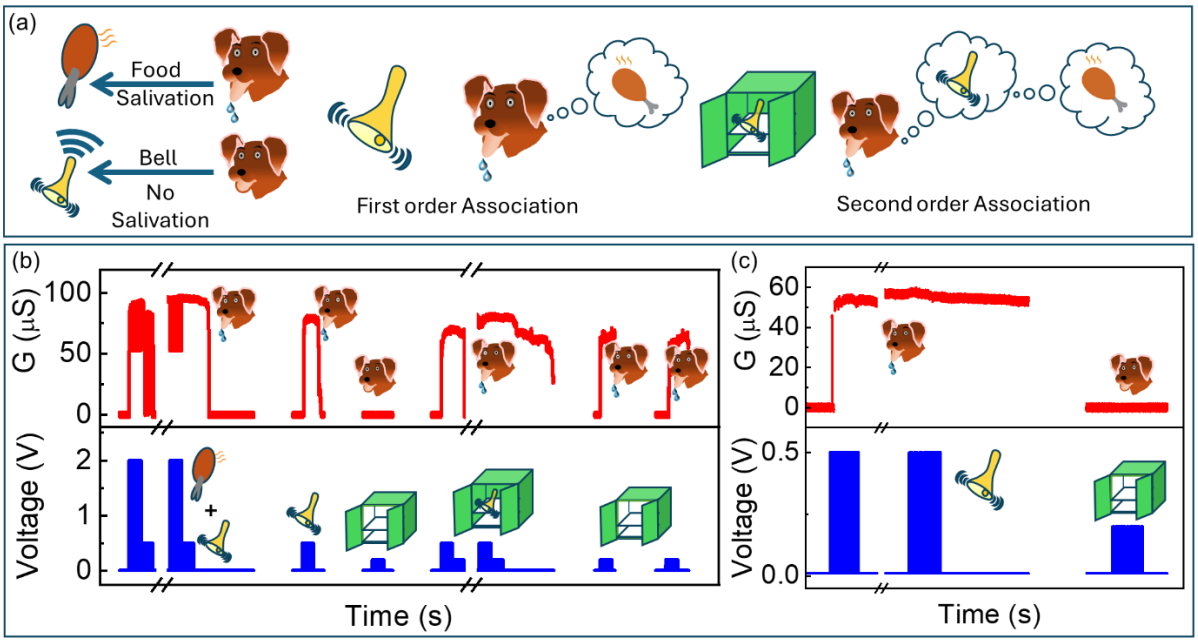

Figure III.11: (a) Schematic illustrating dog salivating for food and not for the bell before association (left); salivating for ringing bell after first order association (middle); salivating for the sound of cupboard opening after second order association. (b) Second-order Classical conditioning was emulated using 2 V (food) and 0.5 V (bell) and a third signal of 0.2 V (cupboard door sound) with 10 sets of training. (c) Higher order/ Second-order conditioning emulated using a third signal 0.2 V (cupboard door sound). (d) No response for the cupboard door sound was observed after the complete dissociation of the conditioning by training with the bell pulses alone.

The human brain can perform higher-order cognitive functions very effectively, such as forming associations within multiple stimuli. Classical conditioning can be extended to a

higher order also associating a new signal with the bell. In this scenario, a cupboard door sound is considered inside which bell is kept. The dog, based on daily observation, can associate the cupboard door sound with the bell signal establishing higher-order or second-order association (Figure III.11a). This higher-order cognitive function was demonstrated using the same device. The whole process of higher-order association is schematically shown in Figure III.11a and experimentally illustrated in Figure III.11b. One more stimulus of 0.2 V was taken and assigned as the cupboard door sound. Initially, the association was created between the food (2 V) and bell (0.5 V) signals. Once the response for the bell signal was observed, the cupboard door sound (0.2 V) was applied, which could not generate any response (Figure III.11b). Further, the bell (0.5 V) and cupboard door sound (0.2 V) signals were applied simultaneously to create the association. The device generated a response for the cupboard door sound (0.2 V) after the training. The observed response for the cupboard door sound gives the empirical demonstration of the higher-order or second-order association. The second-order association was also validated using the application of 10 sets of bell signals to observe the response for the cupboard door signal (Figure III.11c). However, no response was observed for the cupboard door signal, which validates the second-order association.

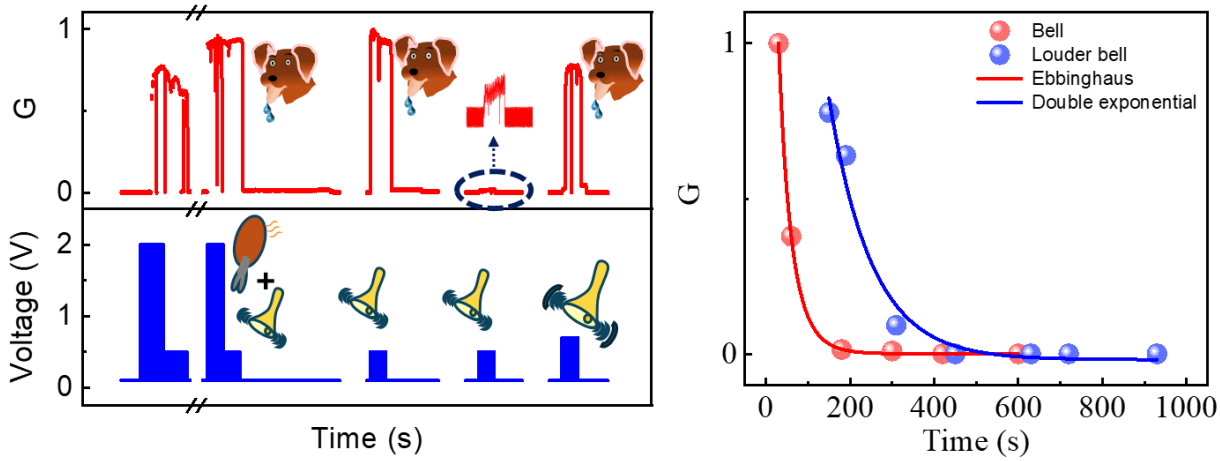

Figure III.12: Gradual decay of bell and louder bell post-association. (b) Forgetting the associated bell and louder bell signal post-association.

The repeated application of bell stimuli alone, without the food stimuli, led to a decrement in the device's response to the bell stimuli. However, when the response for the bell pulse is about to diminish, a higher amplitude bell pulse might activate a higher response. If considered in real-life scenarios, the dog will stop salivating at the bell sound if food is not provided consistently. But when the association strength is about to diminish, the dog may salivate to a louder bell sound in the hope of food. A louder bell sound can reignite

the expectation of food, demonstrating a complex cognitive function. The association was created in the device using similar training sets for bell pulse and the response for bell pulse is constantly monitored. While the response was about to diminish, a louder bell stimulus having a little larger amplitude than the bell stimulus was applied (Figure III.12a). Surprisingly, an enhanced response was observed for the louder bell pulse (Figure III.12a). The device successfully and effectively mimics the complex cognitive behavior including classical conditioning, higher order classical conditioning, and an enhanced response during louder bell application. The previous work from our work also reports the emulation of first and second-order association. However, the decay of the associative learning was not discussed. All the memories formed using several rehearsals in the brain lead to decay over time[37]. The decay of the memory also plays a crucial role in memory management in the brain. To emulate such functionality, the device was first associated with a bell signal. Once the response for the bell signal was observed, it was monitored after regular intervals to see the decay pattern of it. A significant response was observed for the bell signal 30 seconds after the association. However, the response decreases gradually and finally dies after 7 minutes. Along with the bell signal, the response for the louder bell was also monitored which also shows a decay behavior. However, the response to the louder bell took a longer time to diminish. To investigate further, the device conductance values were observed after regular intervals and plotted. The decay of the bell signal was fitted with an Ebbinghaus forgetting curve. The Ebbinghaus forgetting curve describes the decay of human memory as a function of time. This shows that the decay of associative learning shows memory decay similar to human beings. The Ebbinghaus equation is given as.

$$\frac{G}{G_{max}} = \exp\left(-\left(t/\tau\right)\right)^{\beta}$$

Here, G/G_{max} is the synaptic weight change, τ is the relaxation time constant, and β is the stretching exponent (Figure III.12b). From the fitted equation, the values of τ and β were found to be 21.25 s and 0.8. Also, the decay of the louder bell signal was fitted with a double exponential curve. Though both Ebbinghaus and the double exponential function explain the decay of memory over time, the double exponential decay of memory is usually found in humans during the decay of long-term memories[54]. The associative learning forgetting follows Ebbinghaus forgetting, which shows the capability of the

active material to significantly emulate brain-inspired activities. Table III.1 enumerates the neuromorphic devices that mimic associative learning. Notably, it highlights the first instance of emulating Ebbinghaus's forgetting in associative learning.

Table III.2: Comparison of neuromorphic devices mimicking associative learning.

S. No.	Device Structure	Mechanism	Associative learning	Second-order associative learning	Forgetting of associative learning	Ref.
1	Cu/$CuCl_2$/ITO	ECM	Yes	No	No	[25]
2	Cu/Honey-CNT/ITO	ECM	Yes	No	No	[26]
3	Pd/carbon QDs/Ga_2O_3/Pt	ECM	Yes	No	No	[27]
4	Ag/TiO_2/Pt	ECM	Yes	No	No	[28]
5	Ag/Ho_2O_3/FTO	ECM	Yes	No	No	[29]
7	ITO/Al_2O_3 NP:PI/Ag	ECM	Yes	No	No	[30]
8	ITO/MXene/EGaIn	ECM	Yes	No	No	[31]
8	Mo/HfAlO/TiN	VCM	Yes	No	No	[32]
9	Ti/W/NbOx/Nb/Pt	VCM	Yes	No	No	[33]
10	Ag/MoSe2/FTO	VCM	Yes	No	No	[34]
11	Ag/aloe vera/FTO	VCM	Yes	No	No	[35]
12	Au/dewetted Ag/Au*	ECM	Yes	Yes	No	[36]
14	Au/dewetted Ag/Au	ECM	Yes	Yes	Yes	This Work

* Previous work from the group

III.4.2 Variation of the electrode gap

The effective gap between the two Au electrodes can have an impact on the threshold behavior of the device. To study such behavior, three different devices were prepared, having electrode gaps of 100 µm, 200 µm, and 350 µm. These gaps were created using copper wires of different diameters as the shadow mask during the Au electrode

deposition. After the device preparation, these devices were subjected to an electric field through I-V sweeps. The I-V sweep on a pristine device having a 100 µm gap shows the threshold switching at ~ 4.25 V, which is the electroforming or the forming voltage of the device (Figure III.13a). However, consecutive I-V sweeps show a significant decrement in V_{th}. Threshold switching at I_{CC} of 1 and 10 µA shows the further decrement in the V_{th} and finally achieving switching threshold below 1 V. The device having a 250 µm gap demonstrates the threshold switching at 4.75 V forming voltage (Figure III.13b). The similar switching at higher I_{CC} finally results in a threshold voltage of ~ 1.2 V. However, the device having the largest electrode gap of 350 µm resulted in forming and threshold voltage of 40 and 20 V (Figures III.13 c).

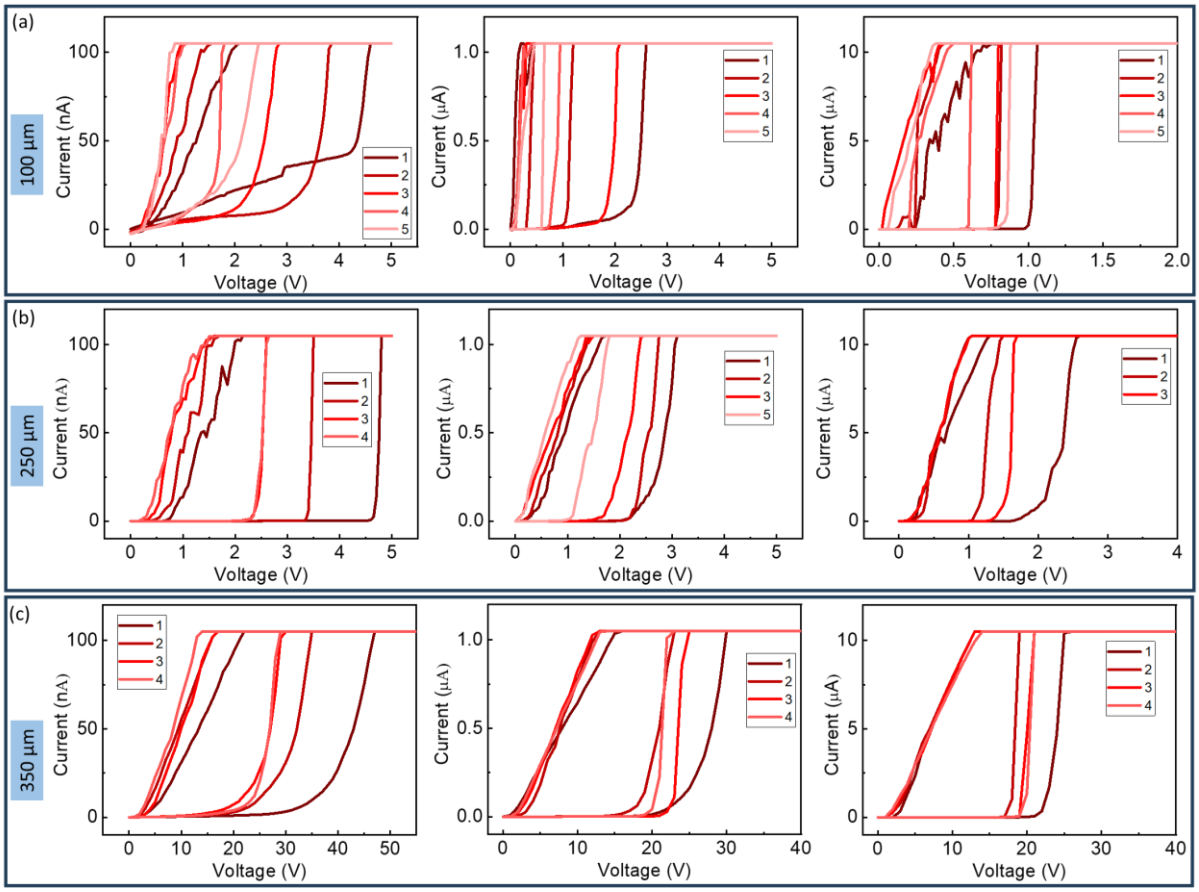

Figure III.13: I-V sweep of the devices at different I_{CC} having electrode gaps of (a) 100 µm, (b) 250 µm and (c) 350 µm.

The forming voltage of these devices is plotted against the electrode gap, which shows an exponential variation with the electrode gap (Figure III.14a). The V_{th} values at I_{CC} of 100 nA, 1 µA, and 10 µA were also plotted against the electrode gap which also follows an exponential trend (Figure III.14b). Also, the V_{th} value was found to be reduced at higher

I_{CC} values as observed in the inset of figure III.14b. As explained earlier, the filaments becomes more consolidated at higher I_{CC} leading to the stabilization of the V_{th} in a narrow range. The table in Figure III.14c shows the final comparison of forming and threshold voltage for all the devices. The reported results show that the effective gap of the electrode plays an important role in the threshold switching of the device, which further can affect learning behaviors.

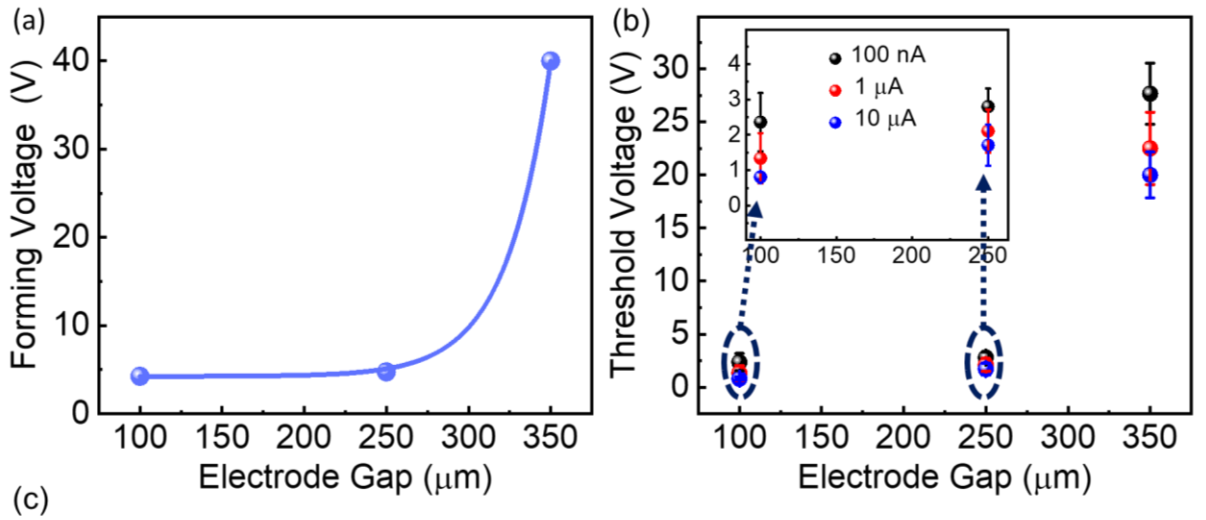

(c)

Electrode Gap (μm)	Forming Voltage (V)	Threshold Voltage (V)		
		100 nA	1 μA	10 μA
100	4.25	2.36	1.34	0.81
250	4.75	2.8	2.11	1.71
350	40	27.66	22.5	20

Figure III.14: (a) The variation of forming voltage with the electrode gap. (b) Threshold voltage at various I_{CC} plotted against electrode gap. (c) Table illustrating the comparison between devices having different electrode gaps.

III.5 Conclusions

In summary, a self-formed dewetted Ag active material was optimized for neuromorphic applications. A two-terminal neuromorphic device with dewetted Ag as active material was fabricated. The device exhibits resistive switching behavior due to the migration of the Ag upon electric field application. The discrete quantum conductance jumps were observed while performing the I-V sweeps, which could be modulated with the help of the sweep rate. The metallic conduction was confirmed using the low-temperature variation of the LRS state. Also, an in-situ FESEM study was employed to observe the traces of conducting filaments. The device successfully mimics the STP and LTP behavior. The

associative learning was also emulated with the help of voltage pulses. Also, the forgetting of associative learning was emulated for the first time, which follows the Ebbhinghaus forgetting curve, which describes the human memory decay pattern.

References

[1] Ajani S N, Khobragade P, Dhone M, Ganguly B, Shelke N and Parati N 2024 Advancements in Computing: Emerging Trends in Computational Science with Next-Generation Computing *Int. J. Intell. Syst. Appl. Eng.* **12** 546–59

[2] Damsgaard H J, Grenier A, Katare D, Taufique Z, Shakibhamedan S, Troccoli T, Chatzitsompanis G, Kanduri A, Ometov A, Ding A Y, Taherinejad N, Karakonstantis G, Woods R and Nurmi J 2024 Adaptive approximate computing in edge AI and IoT applications: A review *J. Syst. Archit.* **150** 103114

[3] H. Seok, D. Lee, S. Son, H. Choi, G. Kim and T. Kim 2024 Beyond von Neumann Architecture: Brain-Inspired Artificial Neuromorphic Devices and Integrated Computing. *Adv. Electron. Mater.* **10**, 2300839

[4] Hemmati A, Raoufi P and Rahmani A M 2024 Edge artificial intelligence for big data: a systematic review. *Neural Comput. Appl.* **36** 11461–11494

[5] Zolfagharinejad M, Alegre-Ibarra U, Chen T, Kinge S and van der Wiel W G 2024 Brain-inspired computing systems: a systematic literature review *Eur. Phys. J. B* **97** 70

[6] Balasubramanian V 2021 Brain power *Proc. Natl. Acad. Sci. U. S. A.* **118** 3–5

[7] Haken H 2013 *Principles of Brain Functioning: A Synergetic Approach to Brain Activity, Behavior and Cognition* (Springer Berlin Heidelberg)

[8] Ho V M, Lee J A and Martin K C 2011 The cell biology of synaptic plasticity *Science* **334** 623–8

[9] Sun Y, Wang H and Xie D 2024 *Recent Advance in Synaptic Plasticity Modulation Techniques for Neuromorphic Applications* vol 16 (Springer Nature Singapore)

[10] Ielmini D and Ambrogio S 2020 Emerging neuromorphic devices *Nanotechnology* **31** 92001

[11] Wan Q, Wan C, Wu H, Yang Y, Huang X, Zhou P, Chen L, Wang T Y, Li Y, Xue K H, He

Y H, Miao X S, Li X, Xie C, Chen H, Song Z, Wang H, Hao Y, Zhang J, Huang J, Ren Z Y, Zhu L Q, Du J, Ge C, Liu Y, Ding G, Zhou Y, Han S T, Wang G, Yu X, Chen B, Chu Z, Wang L, Xia Y, Mu C, Lin F, Chen C, Cheng B, Xing Y, Zeng W, Chen H, Yu L, Indiveri G and Qiao N 2022 2022 roadmap on neuromorphic devices and applications research in China *Neuromorphic Comput. Eng.* **2** 042501

[12] Zhu J, Zhang T, Yang Y and Huang R 2020 A comprehensive review on emerging artificial neuromorphic devices *Appl. Phys. Rev.* **7** 011312 (2020)

[13] Valov I, Waser R, Jameson J R and Kozicki M N 2011 Erratum: Electrochemical metallization memories - Fundamentals, applications, prospects *Nanotechnology* **22** 254003

[14] Waser R and Aono M 2007 Nanoionics-based resistive switching memories *Nat. Mater.* **6** 833–40

[15] Kozicki M N, Mitkova M and Valov I 2016 Electrochemical Metallization Memories *Resist. Switch.* 483–514

[16] Fearing F, Pavlov I P and Anrep G V. 1929 Conditioned Reflexes. An Investigation of the Physiological Activity of the Cerebral Cortex *J. Am. Inst. Crim. Law Criminol.* **20** 153

[17] Ahmed T, Kuriakose S, Mayes E L H, Ramanathan R, Bansal V, Bhaskaran M, Sriram S and Walia S 2019 Optically Stimulated Artificial Synapse Based on Layered Black Phosphorus *Small* **15** 1–12

[18] Chen Y, Qiu W, Wang X, Liu W, Wang J, Dai G, Yuan Y, Gao Y and Sun J 2019 Solar-blind SnO2 nanowire photo-synapses for associative learning and coincidence detection *Nano Energy* **62** 393–400

[19] He W, Fang Y, Yang H, Wu X, He L, Chen H and Guo T 2019 A multi-input light-stimulated synaptic transistor for complex neuromorphic computing *J. Mater. Chem. C* **7** 12523–31

[20] Sahu M C, Sahoo S, Mallik S K, Jena A K and Sahoo S 2023 Multifunctional 2D MoS_2 Optoelectronic Artificial Synapse with Integrated Arithmetic and Reconfigurable Logic Operations for In-Memory Neuromorphic Computing Applications *Adv.*

Mater. Technol. **8** 1–10

[21] Y. Cheng, H. Li, B. Liu, L. Jiang, M. Liu, H. Huang, J. Yang, J. He and J. Jiang 2020 Vertical 0D-Perovskite/2D-MoS2 van der Waals Heterojunction Phototransistor for Emulating Photoelectric-Synergistically Classical Pavlovian Conditioning and Neural Coding Dynamics. *Small* **16**, 2005217

[22] Kim J G, Liu R, Dhakal P, Hou A, Gao C, Qiu J, Merkel C, Zoran M and Wang S 2024 Heterostimuli chemo-modulation of neuromorphic nanocomposites for time-, power-, and data-efficient machine learning *Matter* **7** 1230–44

[23] Ji X, Paulsen B D, Chik G K K, Wu R, Yin Y, Chan P K L and Rivnay J 2021 Mimicking associative learning using an ion-trapping non-volatile synaptic organic electrochemical transistor *Nat. Commun.* **12** 1–12

[24] Wan H, Zhao J, Lo L W, Cao Y, Sepúlveda N and Wang C 2021 Multimodal Artificial Neurological Sensory-Memory System Based on Flexible Carbon Nanotube Synaptic Transistor *ACS Nano* **15** 14587–97

[25] Meng J, Song J, Fang Y, Wang T, Zhu H, Ji L, Sun Q Q, Zhang D W and Chen L 2024 Ionic Diffusive Nanomemristors with Dendritic Competition and Cooperation Functions for Ultralow Voltage Neuromorphic Computing *ACS Nano* **18** 9150–9

[26] Tanim M M H, Templin Z, Hood K, Jiao J and Zhao F 2023 A Natural Organic Artificial Synaptic Device Made from a Honey and Carbon Nanotube Admixture for Neuromorphic Computing *Adv. Mater. Technol.* **8** 1–10

[27] Pei Y, Zhou Z, Chen A P, Chen J and Yan X 2020 A carbon-based memristor design for associative learning activities and neuromorphic computing *Nanoscale* **12** 13531–9

[28] Jena AK, Sahu MC, Mohanan KU, Mallik SK, Sahoo S, Pradhan GK and Sahoo S. 2023 Bipolar Resistive Switching in TiO2 Artificial Synapse Mimicking Pavlov's Associative Learning. *ACS Appl Mater Interfaces.* **15** 3574-3585

[29] Jetty P, Kannan U M and Narayana Jammalamadaka S 2023 Emulation of Pavlovian conditioning and pattern recognition through fully connected neural networks using Holmium oxide (Ho_2O_3) based synaptic RRAM device Nanotechnology **35**

75701

[30] Wu C, Kim T W, Guo T, Li F, Lee D U and Yang J J 2017 Mimicking Classical Conditioning Based on a Single Flexible Memristor *Adv. Mater.* **29** 1602890

[31] Thomas A, Saha P, Sahad E M, Krishnan K N and Das B C 2024 Versatile Titanium Carbide MXene Thin-Film Memristors with Adaptive Learning Behavior *ACS Appl. Mater. Interfaces* **16** 20693–704

[32] Ju D and Kim S 2024 Implementation of edge computing using HfAlO -based memristor *J. Alloys Compd.* **997** 174804

[33] Han C Y, Fang S L, Cui Y L, Liu W, Fan S Q, Huang X D, Li X, Wang X L, Zhang G H, Tang W M, Lai P T, Liu J, Wan X, Yu Z and Geng L 2023 Configurable NbO_x Memristors as Artificial Synapses or Neurons Achieved by Regulating the Forming Compliance Current for the Spiking Neural Network *Adv. Electron. Mater.* **9** 202300018

[34] Chen X, Deng L, Luo F, Wu Y, Tian F and Zhang X 2024 High-performance artificial synapses based on two-dimensional $MoSe_2$ powder with Se vacancies *J. Mater. Chem. C* **12** 7068–78

[35] Jetty P, Kannan U M and Jammalamadaka S 2024 Aloe Vera-Inspired Cognitive Computing: Unveiling the Power of Pavlovian Conditioning and Pattern Recognition with a Synaptic RRAM Device *ACS Appl. Electron. Mater.* **6** 1992–2002

[36] Bannur B, Yadav B and Kulkarni G U 2022 Second-Order Conditioning Emulated in an Artificial Synaptic Network *ACS Appl. Electron. Mater.* **4** 1552–7

[37] Hardt O, Nader K and Nadel L 2013 Decay happens: The role of active forgetting in memory *Trends Cogn. Sci.* **17** 111–20

[38] Łapiński M, Kozioł R, Skubida W, Winiarz P, Mahjoub R, Elhassan Y, Sadowski W and Kościelska B 2023 Transformation of bimetallic Ag – Cu thin films into plasmonically active composite nanostructures *Sci. Rep.* **13** 1–8

[39] Quan J, Zhang J, Qi X, Li J, Wang N and Zhu Y 2017 A study on the correlation between the dewetting temperature of Ag film and SERS intensity *Sci. Rep.* **7** 1–12

[40] Roa S and Burgos M J C 2023 Dewetting regimes in ultra-thin nanocrystalline Ag

films *Mater. Lett.* **336** 133863

[41] Bannur B and Kulkarni G U 2020 On synapse intelligence emulated in a self-formed artificial synaptic network *Mater. Horizons* **7** 2970–7

[42] Masuda H and Kizuka T 2014 Distance control of electromigration-induced silver nanogaps. *J. Nanosci. Nanotechnol.* **14** 2436–40

[43] Jepiti P, Yoon S and Kim J 2022 Electromigration Reliability in Ag Lines Printed with Nanoparticle Inks: Implications for Printed Electronics *ACS Appl. Nano Mater.* **5** 2569–77

[44] Chatterjee A, Bai T, Edler F and Tegenkamp C 2018 Electromigration and morphological changes in Ag nanostructures *J. Phys.: Condens. Matter* **30** 084002

[45] Kim M and Lee J 2018 Short-Term Plasticity and Long-Term Potentiation in Artifi cial Biosynapses with Diffusive Dynamics *ACS Nano* **12** 1680–7

[46] Ohno T, Hasegawa T, Tsuruoka T, Terabe K, Gimzewski J K and Aono M 2011 Short-term plasticity and long-term potentiation mimicked in single inorganic synapses *Nat. Mater.* **10** 591–5

[47] Atkinson R C and Shiffrin R M 1968 Human Memory: A Proposed System and its Control Processes11This research was supported by the National Aeronautics and Space Administration, Grant No. NGR-05-020-036. The authors are indebted to W. K. Estes and G. H. Bower who provided many valuable sugge Psychology of Learning and Motivation vol 2, ed K W Spence and J T Spence (Academic Press) pp 89–195

[48] Barbera S La, Vuillaume D and Alibart F 2015 Filamentary Switching : Synaptic Plasticity through Device Volatility *ACS Nano* **9** 941–9

[49] Milano G, Aono M, Boarino L, Celano U, Hasegawa T, Kozicki M, Majumdar S, Menghini M, Miranda E, Ricciardi C, Tappertzhofen S, Terabe K and Valov I 2022 Quantum Conductance in Memristive Devices: Fundamentals, Developments, and Applications *Adv. Mater.* **34** 2201248

[50] Manning H G, Niosi F, da Rocha C G, Bellew A T, O'Callaghan C, Biswas S, Flowers P F, Wiley B J, Holmes J D, Ferreira M S and Boland J J 2018 Emergence of winner-

takes-all connectivity paths in random nanowire networks *Nat. Commun.* **9** 1–9

[51] Jang B C, Kim S, Yang S Y, Park J, Cha J H, Oh J, Choi J, Im S G, Dravid V P and Choi S Y 2019 Polymer Analog Memristive Synapse with Atomic-Scale Conductive Filament for Flexible Neuromorphic Computing System *Nano Lett.* **19** 839–49

[52] Milano G, Raffone F, Bejtka K, De Carlo I, Fretto M, Pirri F C, Cicero G, Ricciardi C and Valov I 2024 Electrochemical rewiring through quantum conductance effects in single metallic memristive nanowires *Nanoscale Horizons* **9** 416–26

[53] Bannur B and Kulkarni G U 2020 On synapse intelligence emulated in a self-formed artificial synaptic network *Mater. Horizons* **7** 2970–7

[54] Raymond C R and Redman S J 2006 Spatial segregation of neuronal calcium signals encodes different forms of LTP in rat hippocampus *J. Physiol.* **570** 97–111

Chapter IV

A Flexible Artificial Synaptic Network: Fabrication, Characterization, and Emulating Synaptic Activity

Summary

This study introduces flexible neuromorphic devices with dewetted Ag morphology, mimicking biological synaptic activities. The devices exhibit electrically induced switching between high and low resistance states, along with multiple quantum conductance state jumps during retention. Excellent bending endurance and emulation of learning behaviors such as short-term plasticity, long-term potentiation, and classical conditioning, even in bent states, are achieved. This work marks the first demonstration of classical conditioning in a bent state.

IV.1 Introduction

In recent years, there has been a surge in reports on potentiating devices to mimic brain intelligence. These brain-inspired intelligent devices are expected to be efficient in terms of computing speed and energy requirements compared to the conventional von-Neumann-based computers of the present day and would revolutionalize the AI industry. Literature from the last few years is abound with diverse device architectures exploiting a range of active materials. While the two-terminal geometry is more prevalent, three-terminal gated devices are also common. Among active elements, TiO_2, Ag_2S, HfO_2, TaO, and ZnO have been frequently employed[1–8]. Accordingly, device action invokes mechanisms such as electrochemical metallization (ECM), valence change (VCM), phase change (PCM), ferroelectric, etc.[9–13]. ECM-based devices are more frequent due to several advantages- reasonable switching voltages and power consumption, higher reliability, multiple conductance states with high degrees of stability, etc.[14–17]. The devices have been explored for emulating synaptic functionalities such as short-term plasticity (STP), long-term potentiation (LTP), potentiation/depression, spike time-dependent plasticity (STDP), and classical conditioning.

Most designs reported in the literature employ rigid substrates for device fabrication, even though the other components, including the active element, may function just as normal under flex conditions. This is not much of a concern in applications stationed at a location such as high-end computing servers. However, applications in healthcare, soft

robotics, neuroprosthetics, and intelligent sensing demand some degree of flexibility in the context of the wearability of the device. Additionally, such devices ought to be lightweight and consume low power. This explains the busy activity in the literature on building flexible neuromorphic devices (Table S1). Efforts have been observed in this direction recently. For instance, Shi *et al*. reported a 2-terminal flexible device based on a dielectric layer made of wool keratin exhibiting STP and LTP learning behaviors[18]. Burgt *et al*. showed the classical conditioning behavior in flexible devices using PEDOT: PSS as the active layer[19]. In another example, integer and half-integer quantum conductance values were experimentally identified in a flexible PESAl/PV3D3/Cu device[20]. Although these devices are claimed to be flexible, in most instances, the neuromorphic characteristics remain unexplored in the bent states. Indeed, very few report bent-state learning behaviors (see Table S1). Lin *et al*. reported synaptic functionalities such as STP, LTP and STDP in the bent state using WO_x as active material[21]. Also, Yang *et al*. showed forgetting/learning behavior in a strained state[22]. In another example, pattern recognition in a bent state was also achieved[23].

When it comes to complex functionalities, hierarchical architectures are desired so as to attain topological networks having broad working ranges, similar to biological systems. Contextually, self-formed structures have proved to be advantageous over the conventional out-of-plane device geometry due to scalable lithography-free processing, fabrication ease and cost-effectiveness. Some of us reported devices made of self-formed dewetted Ag nanostructures to demonstrate higher-order cognitive functions like supervision, interest-based learning, and classical and second-order conditioning, which otherwise are not so commonly observed in typical neuromorphic devices[24,25]. Nonetheless, the device's potential to emulate cognitive learning at flexible states is yet to be explored.

The present work carries forward the dewetted Ag morphology to a flexible substrate. Simple fabrication of a two-terminal device containing dewetted Ag morphology with bimodal distribution on a flexible substrate to mimic the biological synaptic activities is reported. The application of an electric field aids the Ag-based filament formation, which leads to the switching of the device from a high resistance state (HRS) to a low resistance state (LRS). During the relaxation process of short-term or long-term retention, multiple quantum conductance state jumps were observed, in addition to excellent bending

endurance up to 100 cycles, observed in both flat and bent states. Learning behaviors such as STP, LTP and classical conditioning were successfully emulated even in the bent state of the device. To the best of our knowledge, classical conditioning in a bent state has been emulated for the first time.

IV.2 Scope of the present investigation

This investigation aims to further explore the potential of flexible neuromorphic devices with dewetted Ag morphology. The focus will be on optimizing device performance, understanding the underlying mechanisms of synaptic functionalities in bent states, and exploring complex cognitive learning behaviors. Additionally, investigations into hierarchical architectures and scalable processing techniques will be conducted to enhance device capabilities for applications in healthcare, soft robotics, neuroprosthetics, and intelligent sensing. The study seeks to contribute to the advancement of flexible neuromorphic computing systems with practical implications for wearable and portable technologies.

IV.3 Experimental details

A cleaned Kapton tape of dimension 3×2 cm^2 was deposited with an Ag film of thickness 30 nm using an e-beam evaporator at a pressure of 10^{-6} torr. Subsequently, the substrate was heated at 200 °C in the ambient for 80 s to induce dewetting and form nanostructured Ag islands. Thereafter, a second deposition of Ag (~ 4 nm) was carried out. Finally, a pair of Au contact pads with a gap of 100 μm was formed on the dewetted Ag structure by shadow mask deposition.

Optical microscopy images were collected using a Keyence microscope (VHX 7000) at 2000x magnification. A field emission scanning electron microscope (FESEM) (Thermofisher Apreo 2 S) was employed to visualize the morphology of the Ag nanostructures. All the electrical characterizations were performed in Keithley 2450, while the device was mounted on a standard screw gauge for flexing.

IV.4 Results and discussion

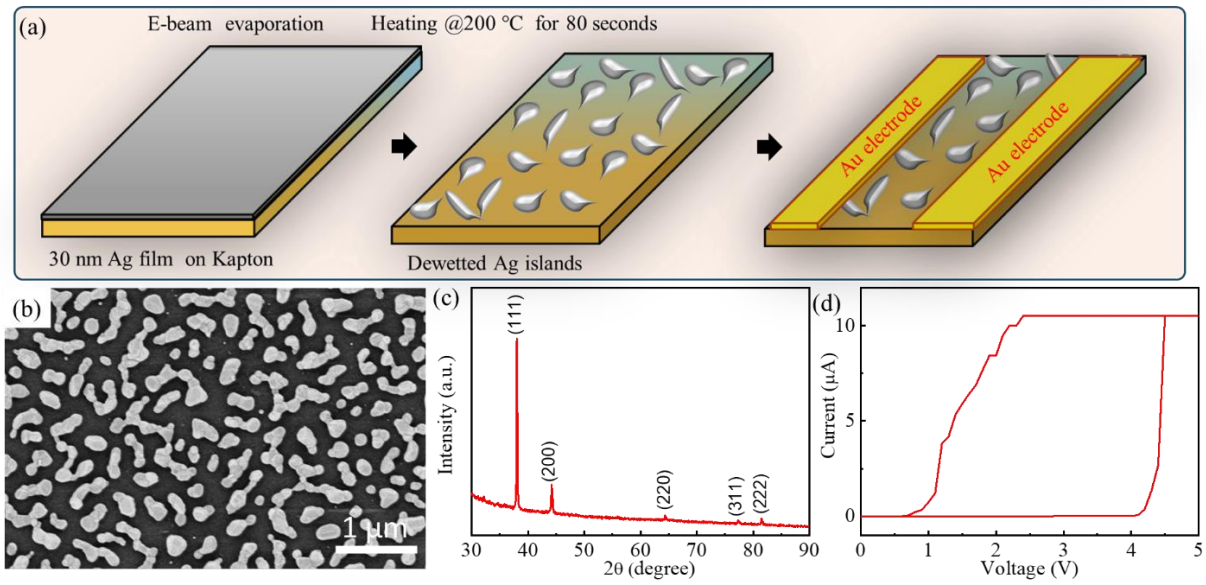

Figure IV.1: (a) Schematic of the stepwise fabrication of the flexible synaptic device containing dewetted Ag islands. (b) SEM image showing dewetted Ag islands with larger gaps. (c) XRD pattern confirming the presence of metallic Ag islands. (d) I-V characteristics show higher V_{th} for the device with Ag Islands.

The steps involved in fabricating the flexible synaptic device are shown schematically in Figure IV.1a. Briefly, a 30 nm of Ag film was first deposited on a flexible and high-temperature stable Kapton substrate, which subsequently was heated at an elevated temperature (200 °C) for 80 seconds to induce dewetting to form isolated Ag Island nanostructures (Figure IV.1a). The FESEM image in Figure IV.1b shows the morphology of the dewetted Ag on flexible substrate. Notably, the temperature was low enough to maintain the metallic nature avoiding oxidation (Figure IV.1c). The device exhibited a non-conducting or a high-resistive behavior lacking continuous paths for electron percolation. At the optimized temperature, sufficient stress was produced in the film overcoming the substrate adhesion, and resulting in the desired dewetting of the film [26]. Nonetheless, the device with the dewetted islands required a high threshold voltage ($V_{th} \sim 4.5$ V) for switching from a high resistance state (HRS) to a low resistance state (LRS) (Figure IV.1d), possibly due to the larger gaps between the islands (see Figure IV.1b). The substantially wide gaps reduce the effective electric field between the electrodes, thereby necessitating the use of higher voltages to cause the electromigration of Ag to bridge the islands.

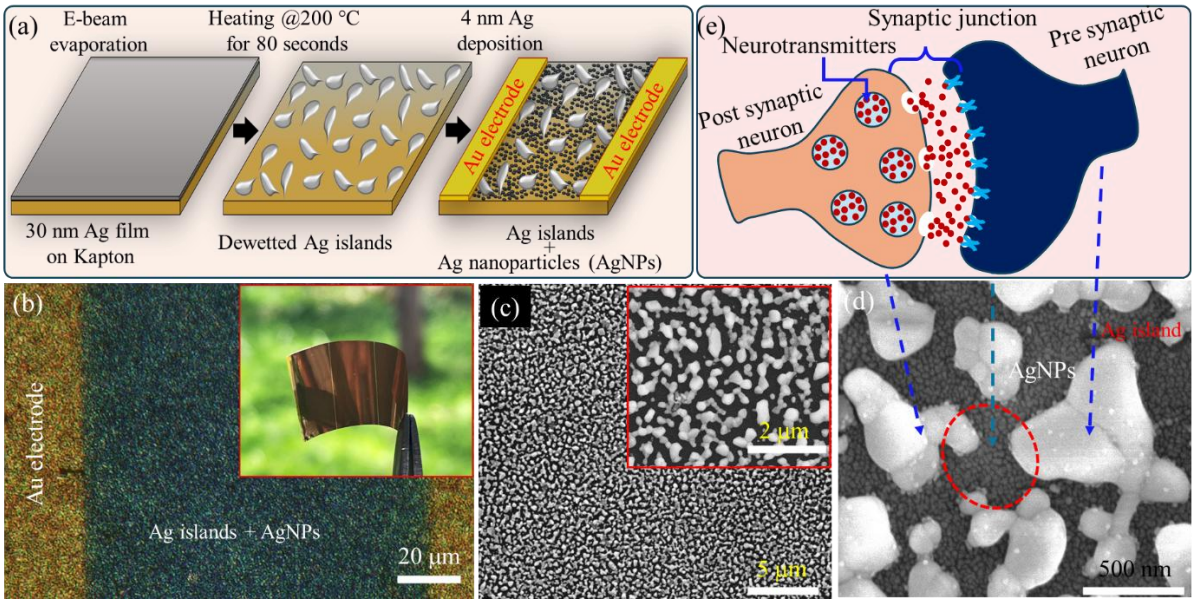

Figure IV.2: (a) Schematic of the stepwise fabrication of the flexible synaptic device containing dewetted Ag islands and Ag nanoparticles. (b) Optical microscopy image of the device with 100 µm Au gap electrodes; inset: photograph of the flexible device. (c) Low and (d) high magnification FESEM images depicting the hierarchical network structure of the Ag islands and Ag nanoparticles. (e) Schematic depicting a notional correlation between the synaptic device and biological synapse. The Ag islands are taken to resemble the bio-neural network, while the nanoparticles are notionally the neural fluid containing ions, which traverse at the synaptic junction potentiating the post-synaptic neuron.

To bring down the V_{th} value to be CMOS-compatible, a second Ag deposition was performed; however, the thickness was kept low (~ 4 nm) such that discrete and tiny Ag nanoparticles formed spontaneously (Figure IV.2a). The device architecture was completed following the gap-electrode formation, as seen in Figure IV.2b and the inset. From the FESEM images in Figure IV.2c and the inset, a random morphology of Ag islands of size 100 to 500 nm may be seen, while in Figure IV.2d, Ag nanoparticles (~ 20 nm) are seen distributed in between the islands. It is expected that the Ag nanoparticles assist the electromigration process in forming Ag filaments between the islands, thereby reducing the V_{th} value (see below). A biological analogy is drawn in Figures IV.2d and IV.2e, where the Ag islands resemble the bio-neural network, while the nanoparticles are notionally the neural fluid containing ions.

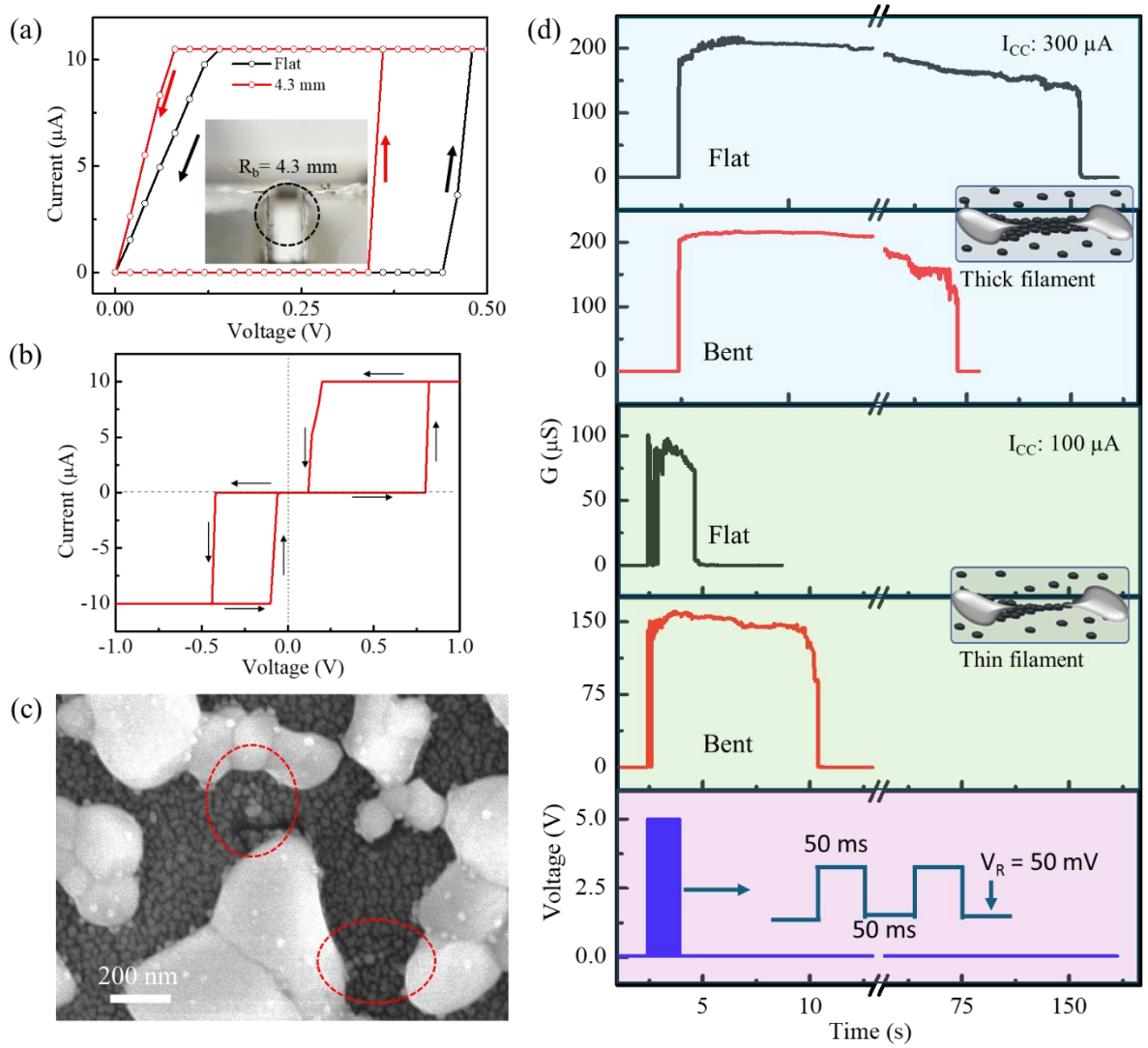

Figure IV.3: Synaptic behavior at flat and bent states: (a) I-V characteristics representing a threshold switching from HRS to LRS; inset is the photograph of a flexible device in the bent state. (b) The full DC I-V sweep of the device showing unipolar behavior. (c) FESEM image evidencing the connecting filament formation contributing to the LRS state. (d) STP to LTP transition with the increase in I_{CC} due to consolidation of the filament, as shown in the inset schematic.

I-V sweep measurements were performed on the two terminal flexible devices (Figure IV.3a) in flat and bent (bending radius, up to 4.3 mm) states. With the sweep range of 0 - 1 V, the device switched from HRS (~ GΩ) to LRS (~ kΩ) at V_{th} of 0.5 and 0.3 V for flat and bent states, respectively, the small decrement observed in the latter may be because of prior I-V sweeps in the flat state. Compared to the switching observed in Ag island film (without nanoparticles), interestingly, there is nearly one order lowering in the V_{th} upon incorporating the 4 nm nanoparticles in the intervening spaces. The full DC I-V sweep shows the unipolar behavior of the device where it switches to an LRS state for both positive and negative polarity (Figure IV.3b). With the application of an electric field, the

electromigration of Ag leads to the formation of continuous filament across the nanogaps, which switches the device to an LRS state. The FESEM image (Figure IV.3c) shows the traces of the filament formation after the device was subjected to the electric field. However, the movement is more localized due to the presence of intermittent nanoparticles, thereby resulting in a high on-off ratio of 10^6 at a comparatively much lower V_{th}. The memory evolution similar to biological synapse is further investigated by employing 20 consecutive 50 ms electrical pulses of amplitude 5 V while reading the conductance state at 50 mV (see Figure IV.3d). For a low current compliance (I_{CC}) of 100 µA, the device showed conductance retention of 1 and 6 seconds at flat and bent states, respectively, thereby emulating an STP behavior. With the increment in I_{CC} to 300 µA, we could see a transition to LTP behavior representing the conduction retention for a prolonged duration of 150 and 65 seconds in the respective states. A plausible reason for the transition is illustrated schematically in the insets of Figure IV.3d, which explains that a higher I_{CC} consolidates the filaments, which are less likely to be dissolved in the absence of the pulse train.

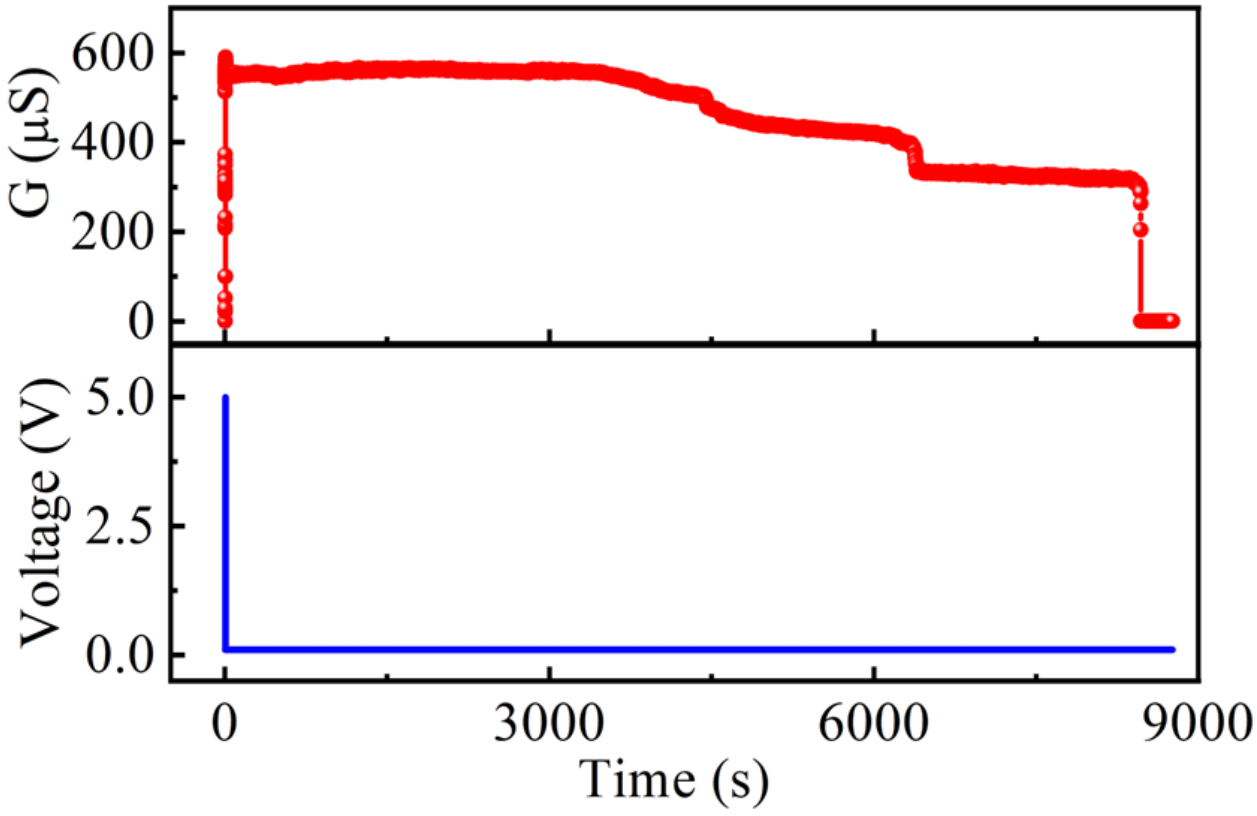

Figure IV.4: The LTP behavior of the device shows a retention of up to 8000 seconds.

By varying the spiking parameters, we can also achieve the hours of retention in our device. Figure IV.4 shows the device retaining its LRS state for up to 2.5 hrs with the application of 5 V 20 pulses at an ICC of 500 µA.

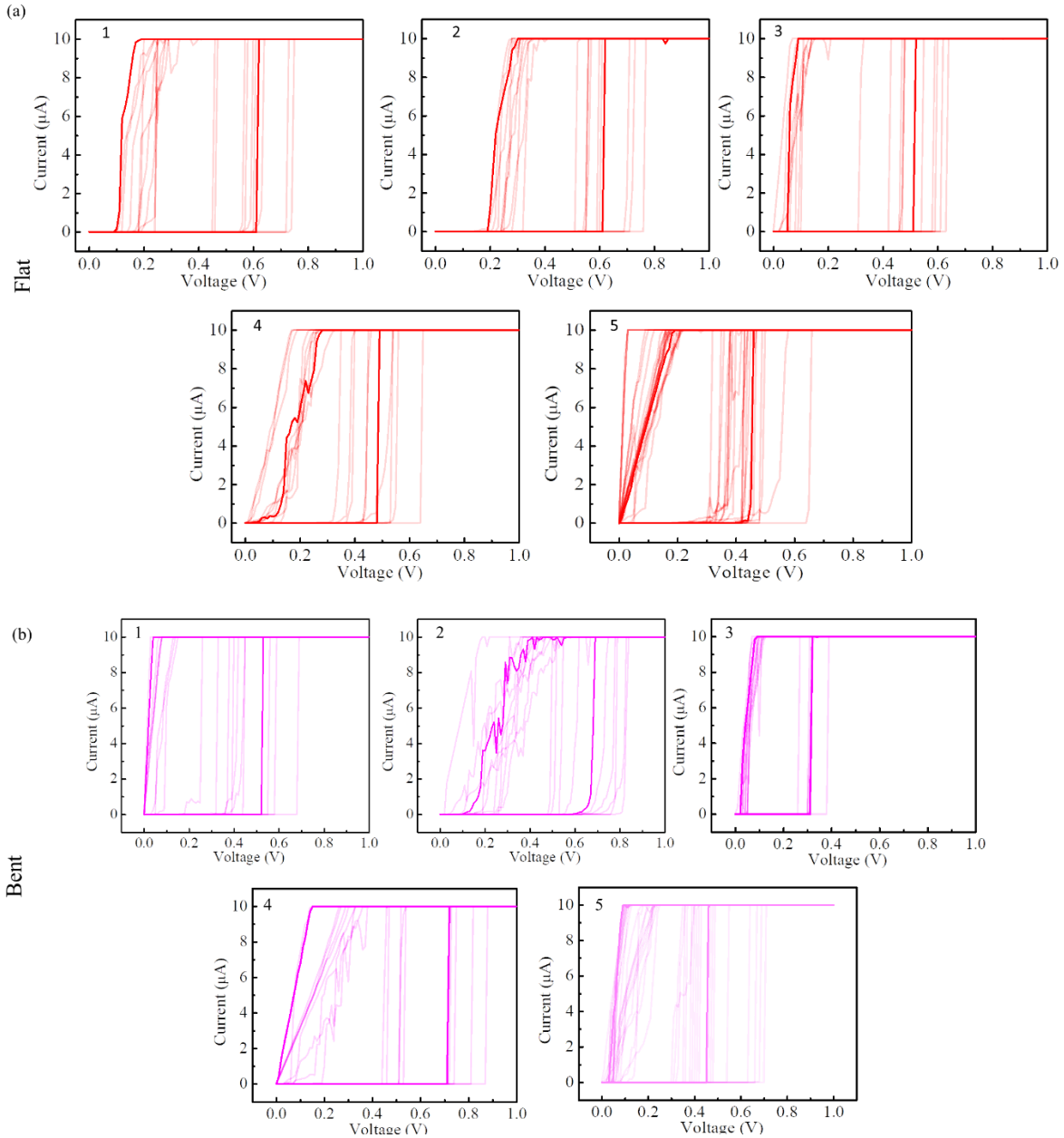

Figure IV.5: Device-to-device variability in the (a) flat state and (b) bent state. Threshold voltage variation with 10 I-V cycles for 5 different devices.

To show the device-to-device variability in the device, five different devices were fabricated. The threshold voltage variation was studied for these devices with multiple I-V sweeps in flat (Figure IV.5a) and bent (Figure IV.5b) states.

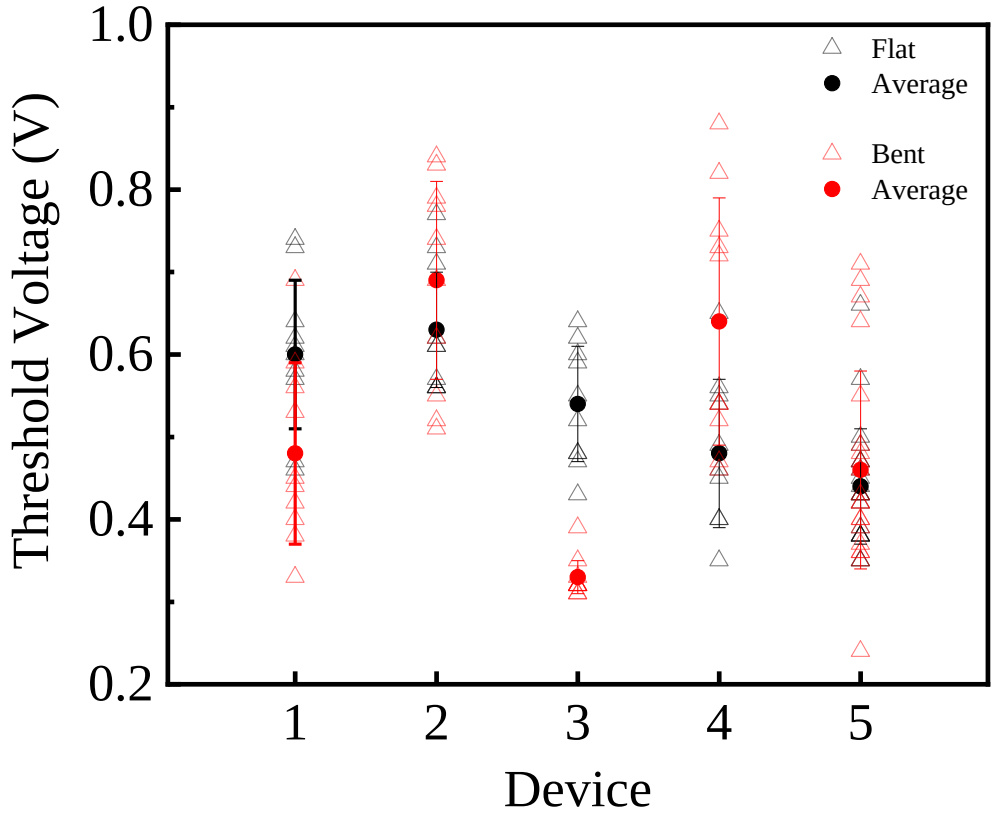

Figure IV.6: V_{th} variation in 5 different devices for 10 I–V cycles in both flat and bent states showing device-to-device variability

The device shows good device-to-device variability as the threshold voltage for all 5 devices was found to be nearly the same. Figure IV.6 shows all the I-V sweeps for 5 different devices in both flat and bent states.

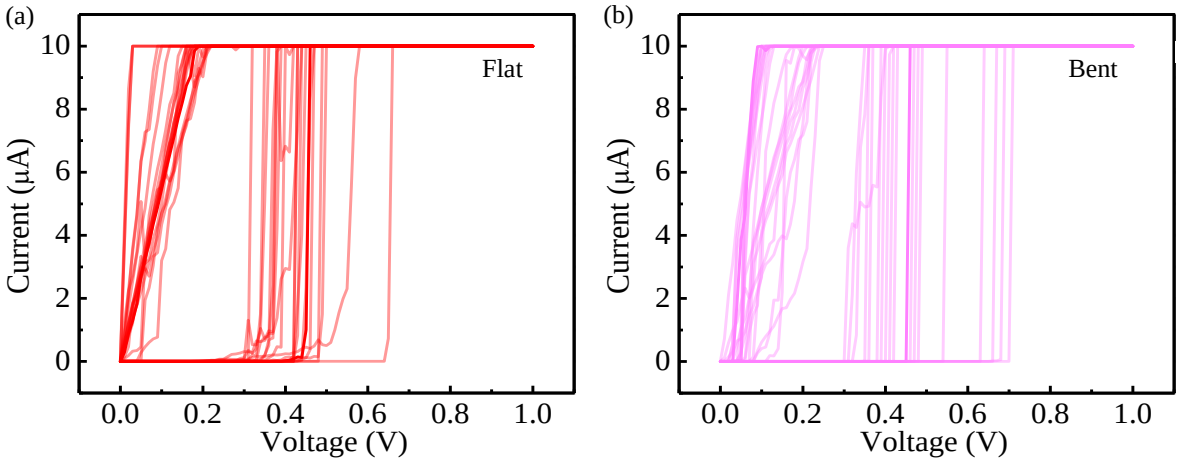

Figure IV.7: Cycle-to-cycle variability in the (a) flat state and (b) bent state. Threshold voltage variation with 10 I-V cycles.

The device also exhibits good cycle-to-cycle variability in both flat and bent states which is confirmed by 20 cycles of I-V sweeps showing minimal change in threshold voltage in flat (Figure IV.7a) and bent (Figure IV.7b) states.

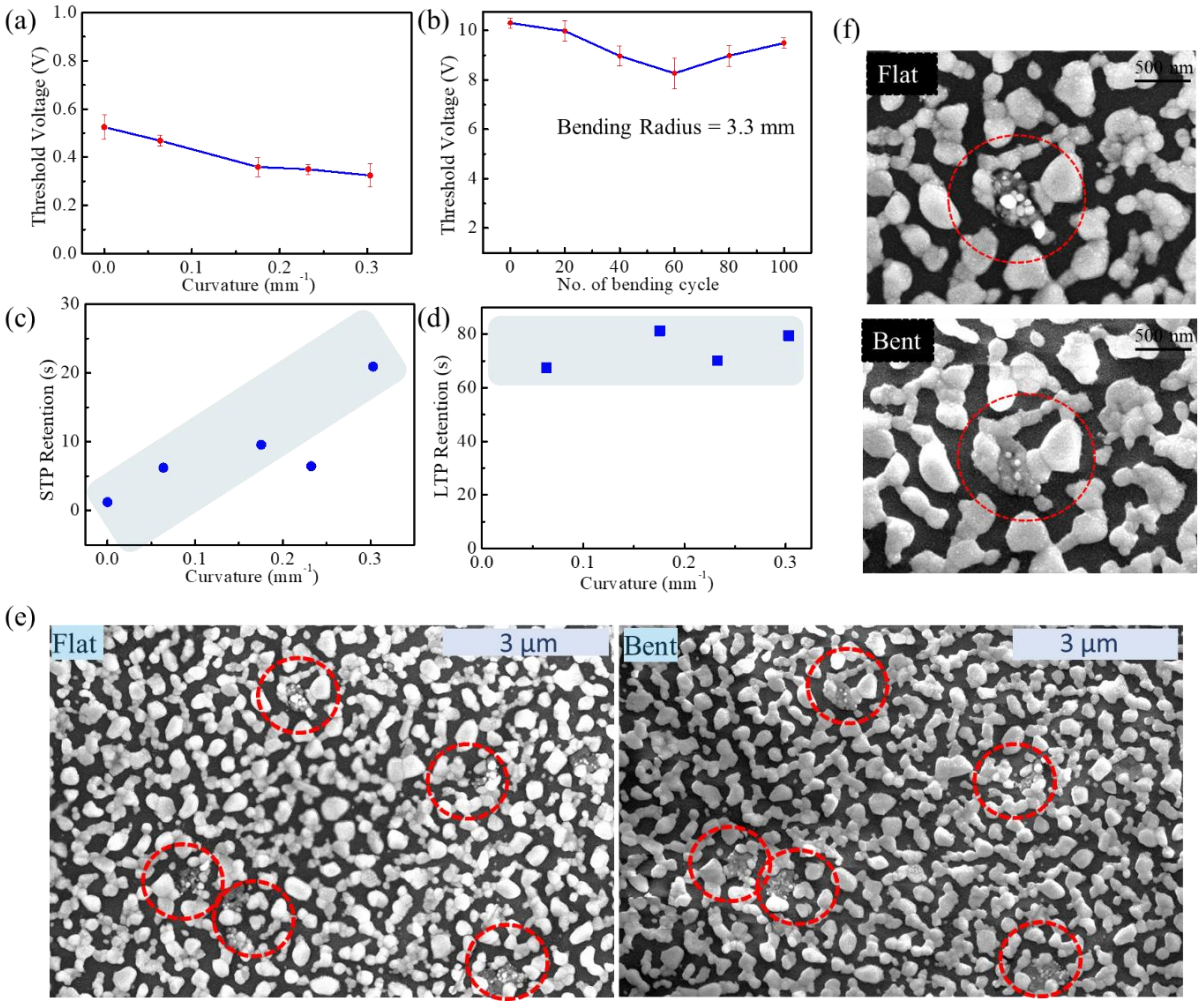

Figure IV.8: Variation in V_{th} with (a) different bending radii and (b) bending cycles. Both show a minimal change in V_{th}. (c) and (d) Histograms, respectively, indicating moderately enhanced STP and nearly unaffected LTP retention with increasing bending radii. (e) Low and (f) High magnification FESEM images collected after pulsing, highlighting the changes in morphology due to bending. These images depict that a few scattered particles (in a flat state) coalesce into the film due to bending, possibly leading to STP enhancement.

Characteristic invariability should be the inherent property of a flexible device at any given state. Therefore, various synaptic activities such as V_{th}, STP, and LTP retention in the flat and bent states (15.7 to 3.3 mm), are compared. As observed in Figure IV.8a, the V_{th} remains nearly unaffected, with a slightly decreasing tendency as the bending radius increases. Next, a cyclic endurance study is performed to find out the reliability of the device against extensive bending. The device was subjected to cyclic bending at ~ 3.3 mm radius, and after every 20 cycles, the Vth was measured. The corresponding plot (Figure

IV.8b) shows no significant variation in Vth even after 100 bending cycles, confirming the excellent endurance of the device. However, a higher threshold voltage was required as the device was kept idle for an extended period of time. Furthermore, the STP retention was found to be enhanced with the increasing bending radius (Figure IV.8c), while the LTP behavior remained unaltered (Figure IV.8d). To find out the underlying reason, FESEM images of the nanostructured morphology before and after bending were investigated (see Figures IV.8e-f). It was observed that some tiny Ag islands, which were found to be discrete in the flat state (Figure IV.8f), were coalesced into a film upon bending, possibly as a result of releasing the substrate-particle interfacial strain. This leads to a decrement in the resultant gap between the Au electrodes and therefore enhances the effective electric field, thereby resulting in threshold electromigration at a lower voltage, as observed in Figure IV.2a. The enhanced electric field also causes consolidation of filaments even at lower ICC values, and hence, the STP retention increases (Figure IV.8c). Nonetheless, no such enhancement was observed in the LTP (Figure IV.8d) since the already formed strong filaments at higher ICC are less likely to be further consolidated.

While carefully observing the conductance retention of the device, it was found that the device returned to the HRS state through discrete jumps. The discrete jumps observed during the end of retention were investigated in detail. The device was subjected to 20 pulses of 5 V at different I_{CC}, and a conductance response was monitored with a 50 mV reading voltage. The device switched to a higher conducting state and achieved STP and LTP states depending on the I_{CC} applied, as explained earlier. During the relaxation process, quantum conductance jumps of integral and half-integral multiple values were observed (Figure IV.9a), which can be expected even for non-magnetic materials[20]. The quantum conductance jumps are attributed to nanoscale Ag filaments formed between the two gold electrodes. The initial conductance of the device eventually reduced from $2G_0$ to G_0 and finally led to the HRS state. These quantum conductance plateaus were also observed in the bent state of the device. A similar set of pulsing was applied to achieve STP and LTP state, and the quantum conductance jumps were observed during retention measurements due to spontaneous filament decay. Quantum conductance jumps are missing in some places, which could possibly be due to the non-uniform degradation of the Ag filaments. The schematic representation shows the possible mechanism for the observed conductance jumps (Figure IV.9b). The quantum conductance $2G_0$ could arise

due to two atomic connections to the electrode [20], and with time, due to relaxation, it can lead to rupturing of one connected atom to result in the G_0 conductance.

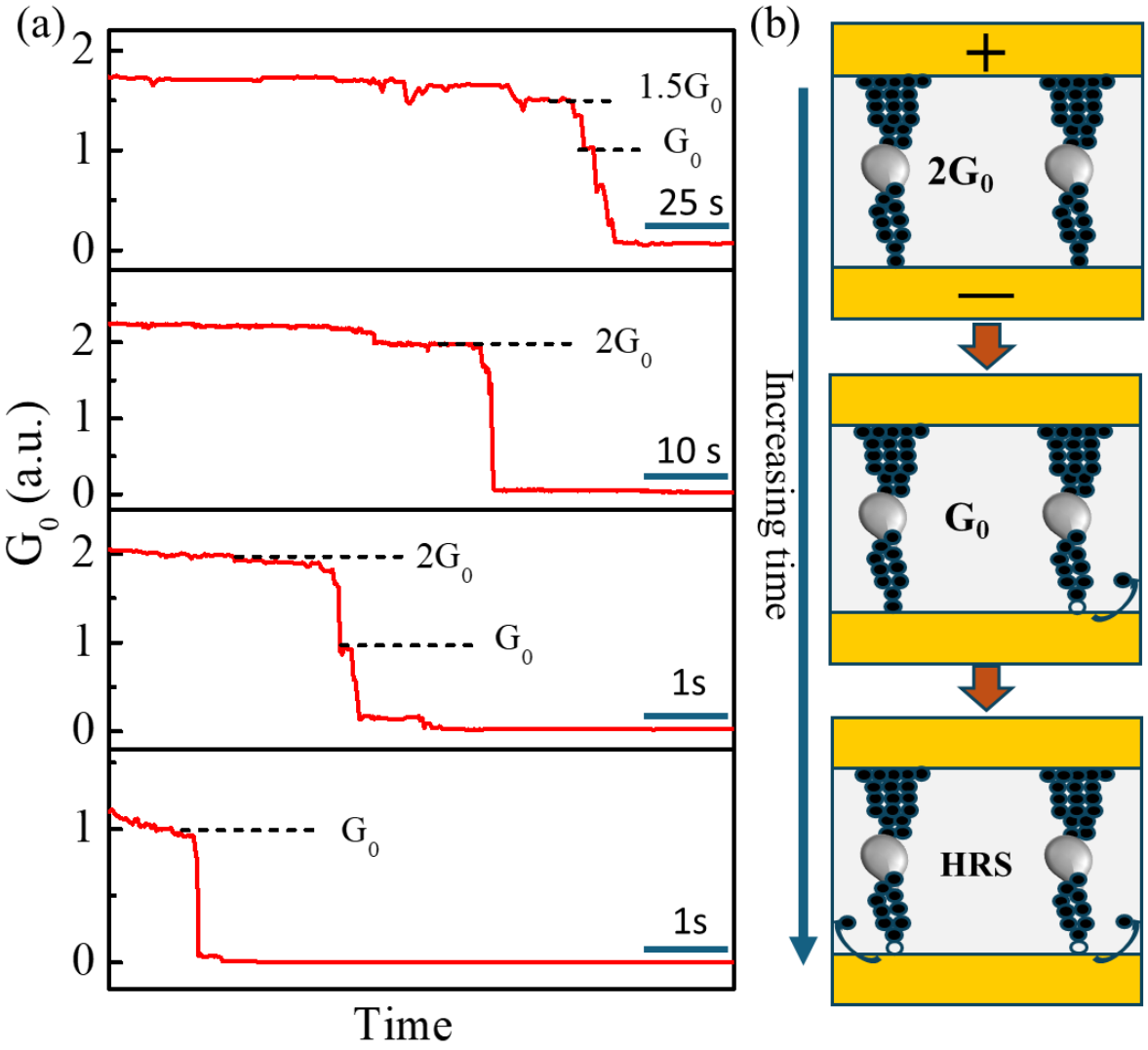

Figure IV.9: (a) Quantum conductance plateaus in STP and LTP states of the device at both flat and bent conditions. (b) Schematic depicting the breaking of atomic connections responsible for the quantum conductance jumps (G_0 = 77.5 µS) in STP and LTP states. $G_0 = 2e^2/h$ where h is Planks's constant and e is the electron charge, and a factor of 2 comes due to spin degeneracy[27].

With further progression of relaxation time, the remaining atomic connection also dissolves due to the volatile nature of the device, leading to another G_0 jump to the HRS state. This shows that by applying suitable I_{CC} and the set voltage, multiple higher quantum conductance states can be achieved during the relaxation process, and this could be an exclusive strategy to obtain multi-bit quantum memory systems. Similar observations have been made in the literature [28–32].

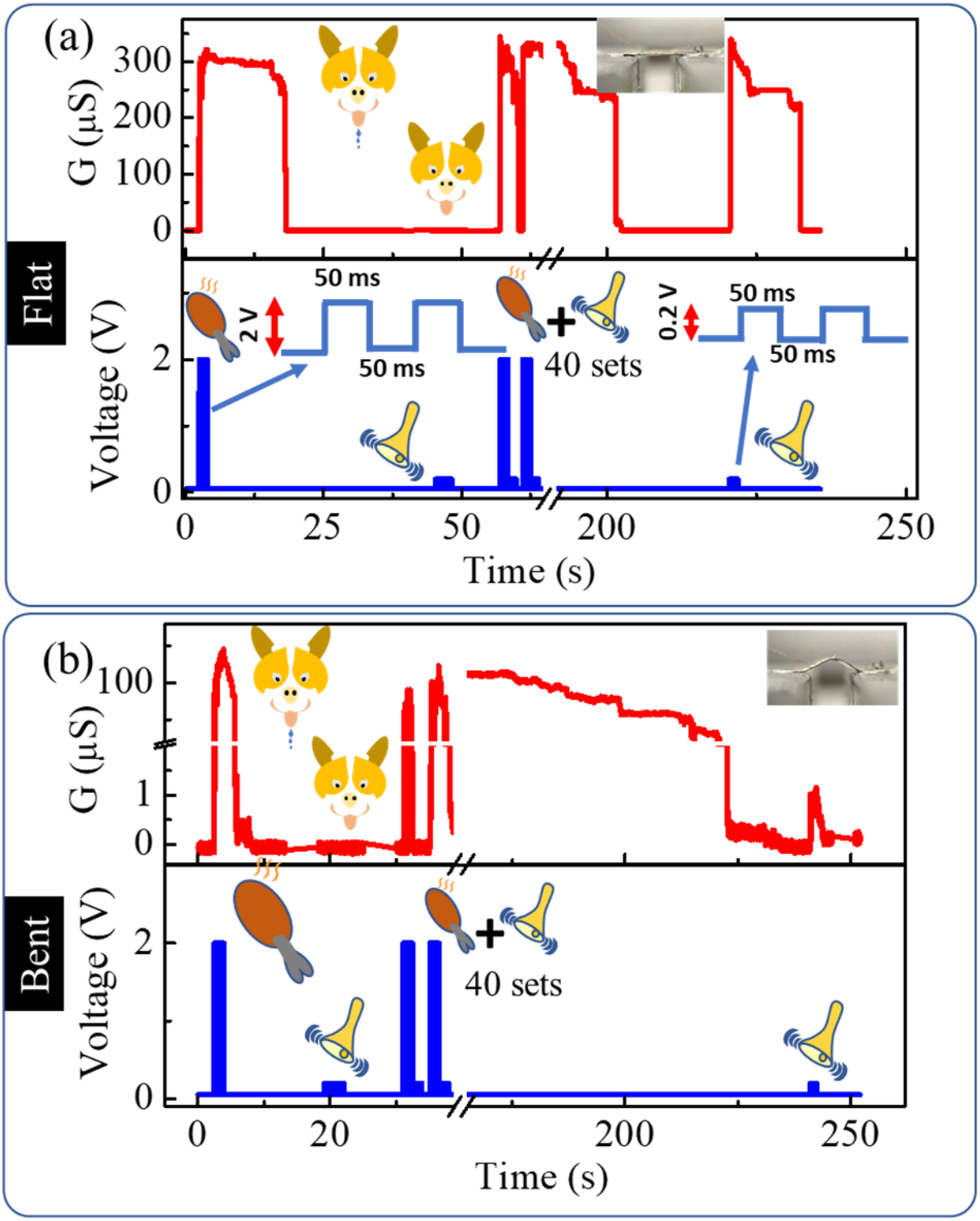

Figure IV.10: Emulation of classical conditioning of Pavlov's dog using the flexible device at (a) flat and (b) bent states. A train of food (2 V) and bell (0.2 V) pulses were applied to the device, and the corresponding output response was examined. Initially, the response was observed only for the food and not for the bell. However, upon developing an association of the food with the bell by applying 40 successive sets of pulses, the device (dog) showed a response for solely bell pulse as well.

Associative learning, also known as a Pavlovian reaction, is a very common phenomenon that we adopt knowingly or unknowingly to strengthen memory formation, which biologically can be correlated with the increment in weight of some intermediate shared synaptic junctions due to the association of two or more uncorrelated neuronal stimuli [33]. In the classical conditioning experiment by Pavlov, it was observed that a dog salivates as a response to the ring of a bell alone after associating the sound with food through adequate training. As part of state-of-the-art intelligence, device-level Pavlovian conditioning is emulated in the present synaptic system, as illustrated in Figures IV.10a and IV.10b at flat and bent states, respectively. Contextually, a 2 V pulse was selected as the food signal (slightly higher than the V_{th} value) to cause the unconditioned response, whereas a 0.2 V pulse was assigned to the bell to trigger a conditioned response. Initially, 20 sets of pulse trains representing food, each containing 20 pulses, were fed to the device. As a response, conductance jumps were perceived, indicating the formation of percolating filaments. However, no such response was observed when a train of bell pulse was applied since the voltage amplitude was way below V_{th}. To initiate the associative training, 40 sets of consecutive food and bell pulse trains were applied to the device. Post-training, the response could be invoked solely by the bell pulse, as shown in Figures IV.10a-b, demonstrating that the bell signal was successfully associated with the food signal. Importantly, the classical conditioning was unaffected when emulated in the bent state (5.7 mm bending radius), and to the best of our knowledge, a flex state Pavlovian conditioning is exemplified for the first time (Table IV.1). The underlying mechanism may be ascribed to a temporally stabilized forest of uneven filaments in the hierarchical nanogaps between the Ag islands when the electrical stimuli of varying amplitudes were consecutively applied [34].

Table IV.1: Comparison table of flexible synaptic devices.

Material	Terminal	Signal	Switching Threshold	Endurance	Level of flexibility (mm)	Applications in the bent state	Ref.
$Pt/WO_x/Ti$	2	E	2 V	✓	8	LTP/LTD, STP/LTP, PPF, STDP	[21]
ITO/PEDOT/PSS/ ITO	2	E	2 V	✓	5	Learning/Forgetting, LTP/LTD, PPF	[35]

PET/SiO2/ITO/MAEGST/ITO	3	E	-	✓	5	LTP/LTD	[36]
PEN/PIBET-A/Au/Ion Gel/Au	3	E	-	✓	2.5	LTP/LTD	[37]
Au/BFO/SRO/BTO/mica	2	E	20 V	✓	5	STDP	[38]
Pt/$HfAlO_x$/TaN	2	E	1 V	✓	5	LTP/LTD	[39]
PDMS/Au/TPU:Ag NPs/Au	2	E	0.8 V	✓	-	STP/LTP, LTP/LTD, Forgetting/Learning, SRDP	[22] (Strain based)
PET/Al_2O_3/ZrO2/Al_2O_3/MoS_2/TI	3	E + O	-	-	5	LTP/LTD	[40]
ITO/PEDOT:PSS/$Cs_3Cu_2I_5$/Au	2	E	0.1 V	-	5	Pattern Recognition, LTP/LTD, LTP	[23]
Ta/TiO_x/TaO_x/Ru	2	E	0.5 V	✓	2	STDP, P/D	[41]
Au/WO_x/Pt	2	E	1 V	-	13	Digit Recognition, P/D	[42]
Pt/BFO/LSMO/PDMS	2	E	4	✓	-	STDP, PPF	[43]
PI/Au/graphene/ion gel/Au	3	E+O	0.5 V	-	60°	PPF	[44]
Ag/WoolKeratin/ITO/PEN	2	E	-	✓	1.2	None	[18]
PEI/PEDOT: PSS	3	E	-	✓	-	None	[45]
PESAl/PV3D3/Cu	3	E	3.5 V	✓	4	None	[20]
PEN/(P3HT/PEO)/Ag	3	E+O	-	✓	5	None	[46]
Ag/HfO_x/Ti/PET	2	E	2 V	✓	7.5	None	[47]
Ag/Corn starch: PVDF/ITO	2	E	-	✓	120°	Digit Recognition, neural sensing, logic operation, and pressure detection	[48]
Ag/Mn-ZnO/ITO	2	E	0.6 V	-	10	None	[49]
glass/ITO/PVPy–Au@Ag (Non Volatile)	2	E	3 V	✓	10	None	[50]
Al/agarose@AuNPs/ITO-PEN (Non Volatile)	2	E	0.7 V	✓	4	None	[51]
ITO/HOFs@Au/Al (volatile)	2	E	3 V	-	3.1 °	None	[52]
Al/SA:Au NPs/ITO/glass (Non volatile)	2	E	3 V	-	-	None	[53]
Al/AM:Au NPs/ITO/glass (Non volatile)	2	E	2.5 V	-	-	None	[54]
Au/Dewetted-Ag/Au	**2**	**E**	**0.3 V**	✓	**3**	**STP/LTP, Quantum conductance, Associative Learning**	**Our Work ***

IV.5 Conclusions

To summarize, a two-terminal flexible synaptic device based on a self-formed dewetted Ag structure with a bimodal distribution was successfully fabricated. The device shows the switching due to the electromigration of Ag, which forms a conducting path. STP and LTP behaviors were successfully emulated in the flat as well as in bent states. A high-

magnification FESEM image provides evidence of filamentary path formation. Short-term and long-term retention of conductance shows half and full integer quantum conductance plateaus. Pavlov's dog conditioning was achieved in the flat and bent state of the device without the use of an external circuit. We have successfully emulated the cognitive behavior in the flexed state, showing potential for utilization in flexible electronics.

References

[1] Zhu J, Zhang T, Yang Y and Huang R 2020 A comprehensive review on emerging artificial neuromorphic devices *Appl. Phys. Rev.* **7** 011312

[2] Li J, Yang Y, Yin M, Sun X, Li L and Huang R 2020 Electrochemical and thermodynamic processes of metal nanoclusters enabled biorealistic synapses and leaky-integrate-and-fire neurons *Mater. Horizons* **7** 71–81

[3] Terabe K, Hasegawa T, Nakayama T and Aono M 2005 Quantized conductance atomic switch *Nature* **433** 47–50

[4] Milano G, Luebben M, Ma Z, Dunin-Borkowski R, Boarino L, Pirri C F, Waser R, Ricciardi C and Valov I 2018 Self-limited single nanowire systems combining all-in-one memristive and neuromorphic functionalities *Nat. Commun.* **9** 1–10

[5] Wang T Y, Meng J L, He Z Y, Chen L, Zhu H, Sun Q Q, Ding S J, Zhou P and Zhang D W 2020 Room-temperature developed flexible biomemristor with ultralow switching voltage for array learning *Nanoscale* **12** 9116–23

[6] Zhou Z, Zhao J, Chen A P, Pei Y, Xiao Z, Wang G, Chen J, Fu G and Yan X 2020 Designing carbon conductive filament memristor devices for memory and electronic synapse applications *Mater. Horizons* **7** 1106–14

[7] Pei Y, Zhou Z, Chen A P, Chen J and Yan X 2020 A carbon-based memristor design for associative learning activities and neuromorphic computing *Nanoscale* **12** 13531–9

[8] Wedig A, Luebben M, Cho D Y, Moors M, Skaja K, Rana V, Hasegawa T, Adepalli K K, Yildiz B, Waser R and Valov I 2016 Nanoscale cation motion in TaO_x, HfO_x and TiO_x memristive systems *Nat. Nanotechnol.* **11** 67–74

[9] Ohno T, Hasegawa T, Tsuruoka T, Terabe K, Gimzewski J K and Aono M 2011 Short-term plasticity and long-term potentiation mimicked in single inorganic synapses

Nat. Mater. **10** 591–5

[10] Sebastian A, Le Gallo M, Burr G W, Kim S, BrightSky M and Eleftheriou E 2018 Tutorial: Brain-inspired computing using phase-change memory devices *J. Appl. Phys.* **124** 111101

[11] Kim K M, Jeong D S and Hwang C S 2011 Nanofilamentary resistive switching in binary oxide system; A review on the present status and outlook *Nanotechnology* **22** 254002

[12] Majumdar S, Tan H, Qin Q H and van Dijken S 2019 Energy-Efficient Organic Ferroelectric Tunnel Junction Memristors for Neuromorphic Computing *Adv. Electron. Mater.* **5** 1–10

[13] Mulaosmanovic H, Chicca E, Bertele M, Mikolajick T and Slesazeck S 2018 Mimicking biological neurons with a nanoscale ferroelectric transistor *Nanoscale* **10** 21755–63

[14] Wang J, Cao G, Sun K, Lan J, Pei Y, Chen J and Yan X 2022 Alloy electrode engineering in memristors for emulating the biological synapse *Nanoscale* **14** 1318–26

[15] Chekol S A, Menzel S, Ahmad R W, Waser R and Hoffmann-Eifert S 2022 Effect of the Threshold Kinetics on the Filament Relaxation Behavior of Ag-Based Diffusive Memristors *Adv. Funct. Mater.* **32** 2111242

[16] Milano G, Pedretti G, Fretto M, Boarino L, Benfenati F, Ielmini D, Valov I and Ricciardi C 2020 Brain-Inspired Structural Plasticity through Reweighting and Rewiring in Multi-Terminal Self-Organizing Memristive Nanowire Networks *Adv. Intell. Syst.* **2** 2000096

[17] Barbera S La, Vuillaume D and Alibart F 2015 Filamentary Switching : Synaptic Plasticity through Device Volatility *ACS Nano* **9** 941–9

[18] Shi C, Lan J, Wang J, Zhang S, Lin Y, Zhu S, Stegmann A E, Yu R, Yan X and Liu X Y 2020 Flexible and Insoluble Artificial Synapses Based on Chemical Cross-Linked Wool Keratin *Adv. Funct. Mater.* **30** 1–11

[19] Yu R, Yan Y, Li E, Wu X, Zhang X, Chen J, Hu Y, Chen H and Guo T 2021 Bi-mode

electrolyte-gated synaptic transistor via additional ion doping and its application to artificial nociceptors *Mater. Horizons* **8** 2797–807

[20] Jang B C, Kim S, Yang S Y, Park J, Cha J H, Oh J, Choi J, Im S G, Dravid V P and Choi S Y 2019 Polymer Analog Memristive Synapse with Atomic-Scale Conductive Filament for Flexible Neuromorphic Computing System *Nano Lett.* **19** 839–49

[21] Lin Y, Zeng T, Xu H, Wang Z, Zhao X and Liu W 2018 Transferable and Flexible Artificial Memristive Synapse Based on WO_x Schottky Junction on Arbitrary Substrates *Adv. Electron. Mater.* **4** 1800373

[22] Yang M, Zhao X, Tang Q, Cui N, Wang Z, Tong Y and Liu Y 2018 Stretchable and conformable synapse memristors for wearable and implantable electronics *Nanoscale* **10** 18135–44

[23] Yang J M, Jung Y K, Lee J H, Kim Y C, Kim S Y, Seo S, Park D A, Kim J H, Jeong S Y, Han I T, Park J H, Walsh A and Park N G 2021 Asymmetric carrier transport in flexible interface-type memristor enables artificial synapses with sub-femtojoule energy consumption *Nanoscale Horizons* **6** 987–97

[24] Bannur B and Kulkarni G U 2020 On synapse intelligence emulated in a self-formed artificial synaptic network *Mater. Horizons* **7** 2970–7

[25] Bannur B, Yadav B and Kulkarni G U 2022 Second-Order Conditioning Emulated in an Artificial Synaptic Network *ACS Appl. Electron. Mater.* **4** 1552–7

[26] Quan J, Zhang J, Qi X, Li J, Wang N and Zhu Y 2017 A study on the correlation between the dewetting temperature of Ag film and SERS intensity *Sci. Rep.* **7** 1–12

[27] Nandakumar S R, Minvielle M, Nagar S, Dubourdieu C and Rajendran B 2016 A 250 mV Cu/SiO_2/W Memristor with Half-Integer Quantum Conductance States *Nano Lett.* **16** 1602–8

[28] Tsuruoka T, Hasegawa T, Terabe K and Aono M 2012 Conductance quantization and synaptic behavior in a Ta_2O_5-based atomic switch *Nanotechnology* **23** 435705

[29] Tappertzhofen S, Valov I and Waser R 2012 Quantum conductance and switching kinetics of AgI-based microcrossbar cells *Nanotechnology* **23** 145703

[30] Krishnan K, Muruganathan M, Tsuruoka T, Mizuta H and Aono M 2017 Quantized

conductance operation near a single-atom point contact in a polymer-based atomic switch *Jpn. J. Appl. Phys.* **56** 1–5

[31] Gao S, Zeng F, Chen C, Tang G, Lin Y, Zheng Z, Song C and Pan F 2013 Conductance quantization in a Ag filament-based polymer resistive memory *Nanotechnology* **24** 335201

[32] Aga F G, Woo J, Song J, Park J, Lim S, Sung C and Hwang H 2017 Controllable quantized conductance for multilevel data storage applications using conductive bridge random access memory *Nanotechnology* **28** 115707

[33] Fearing F, Pavlov I P and Anrep G V. 1929 Conditioned Reflexes. An Investigation of the Physiological Activity of the Cerebral Cortex *J. Am. Inst. Crim. Law Criminol.* **20** 153

[34] Bannur B and Kulkarni G U 2020 On synapse intelligence emulated in a self-formed artificial synaptic network *Mater. Horizons* **7** 2970–7

[35] Wang T Y, Meng J L, He Z Y, Chen L, Zhu H, Sun Q Q, Ding S J, Zhou P and Zhang D W 2019 Fully transparent, flexible and waterproof synapses with pattern recognition in organic environments *Nanoscale Horizons* **4** 1293–301

[36] Qin W, Kang B H and Kim H J 2021 Flexible Artificial Synapses with a Biocompatible Maltose – Ascorbic Acid Electrolyte Gate for Neuromorphic Computing *ACS Appl Mater Interfaces.* **13** 34597-34604

[37] Zhao Y, Su C, Shen G, Xie Z, Xiao W, Fu Y, Inal S, Wang Q, Wang Y, Yue W, McCulloch I and He D 2022 Donor Engineering Tuning the Analog Switching Range and Operational Stability of Organic Synaptic Transistors for Neuromorphic Systems *Adv. Funct. Mater.* **32** 1–11

[38] Sun H, Luo Z, Zhao L, Liu C, Ma C, Lin Y, Gao G, Chen Z, Bao Z, Jin X, Yin Y and Li X 2020 $BiFeO_3$-Based Flexible Ferroelectric Memristors for Neuromorphic Pattern Recognition *ACS Appl. Electron. Mater.* **2** 1081–9

[39] Wang T Y, Meng J L, Rao M Y, He Z Y, Chen L, Zhu H, Sun Q Q, Ding S J, Bao W Z, Zhou P and Zhang D W 2020 Three-Dimensional Nanoscale Flexible Memristor Networks with Ultralow Power for Information Transmission and Processing

Application *Nano Lett.* **20** 4111–20

[40] Wang T, Meng J, He Z, Chen L, Zhu H, Sun Q, Ding S, Zhou P and Zhang D W 2020 Ultralow Power Wearable Heterosynapse with Photoelectric Synergistic Modulation *Adv. Sci.* **7**, 1903480

[41] Li J, Hao C, Guo S, Li Y, Ren J, Zhou L and Zhao J 2021 Flexible Ta/TiO_x/TaO_x/Ru memristive synaptic devices on polyimide substrates *Nanotechnology* **32** 335205

[42] Zhang L, Tang Z, Yao D, Fan Z, Hu S, Sun Q J, Tang X G, Jiang Y P, Guo X, Huang M, Zhong G and Gao J 2022 Synaptic behaviors in flexible Au/WO_x/Pt/mica memristor for neuromorphic computing system *Mater. Today Phys.* **23** 100650

[43] Zhao Z, Abdelsamie A, Guo R, Shi S, Zhao J, Lin W, Sun K, Wang J, Wang J, Yan X and Chen J 2022 Flexible artificial synapse based on single-crystalline $BiFeO_3$ thin film *Nano Res.* **15** 2682–8

[44] Liu S, He X, Su J, Cao B, Rao L, Li C, Yang X and Xin X 2022 A Light-Stimulus Flexible Synaptic Transistor Based on Ion-Gel Side-Gated Graphene for Neuromorphic Computing *Adv. Photonics Res.* **3** 2200174

[45] Van De Burgt Y, Lubberman E, Fuller E J, Keene S T, Faria G C, Agarwal S, Marinella M J, Alec Talin A and Salleo A 2017 A non-volatile organic electrochemical device as a low-voltage artificial synapse for neuromorphic computing *Nat. Mater.* **16** 414–8

[46] Zhang S and Xu W 2020 All-printed ultra-flexible organic nanowire artificial synapses *J. Mater. Chem. C* **8** 11138–44

[47] Zhu S, Sun B, Zhou G, Guo T, Ke C, Chen Y, Yang F, Zhang Y, Shao J and Zhao Y 2023 In-Depth Physical Mechanism Analysis and Wearable Applications of HfO_x-Based Flexible Memristors *ACS Appl. Mater. Interfaces* **15** 5420–31

[48] Sun B, Chen Y, Zhou G, Zhou Y, Guo T, Zhu S, Mao S, Zhao Y, Shao J and Li Y 2023 A Flexible Corn Starch-Based Biomaterial Device Integrated with Capacitive-Coupled Memristive Memory, Mechanical Stress Sensing, Synapse, and Logic Operation Functions *Adv. Electron. Mater.* **9** 2201017

[49] Xue Q, Hang T, Liang J, Chen C C, Wu Y, Ling H and Li M 2022 Nonvolatile resistive

memory and synaptic learning using hybrid flexible memristor based on combustion synthesized Mn-ZnO *J. Mater. Sci. Technol.* **119** 123–30

[50] Zhou L, Mao J Y, Ren Y, Yang J Q, Zhang S R, Zhou Y, Liao Q, Zeng Y J, Shan H, Xu Z, Fu J, Wang Y, Chen X, Lv Z, Han S T and Roy V A L 2018 Biological Spiking Synapse Constructed from Solution Processed Bimetal Core–Shell Nanoparticle Based Composites *Small* **14** 1–10

[51] Kim Y, An J S, Lee D, Ryu S Y, Hwang Y C, Kim D H and Kim T W 2023 Biocompatible memristive device based on an agarose@gold nanoparticle-nanocomposite layer obtained from nature for neuromorphic computing *Sci. Rep.* **13** 1–9

[52] Zhang C, Li Y, Yu F, Wang G, Wang K, Ma C, Yang X, Zhou Y and Zhang Q 2023 Visual growth of nano-HOFs for low-power memristive spiking neuromorphic system *Nano Energy* **109** 108274

[53] Wang L, Xie J and Wen D 2023 Forming-free plant resistive random access memory based on the Coulomb blockade effect produced by gold nanoparticles *Phys. Chem. Chem. Phys.* 18132–8

[54] Wang L, Li J and Wen D 2023 Amylum Resistive Random Access Memory Based on the Quantization Effect of Gold Nanoparticles *ACS Appl. Electron. Mater.* **5** 397–405

Chapter VA

A Stretchable Neuromorphic Device Mimicking Antinociception Behavior

Summary

This study introduces a novel biomimetic neuromorphic device that functions as a mechanosensor in the low strain range and exhibits excellent neuromorphic functionalities at higher strains. The device, featuring a stretchable self-healing design with a hierarchical Ag microwire network on a PDMS substrate, emulates brain-inspired behaviors such as conductance switching and synaptic plasticity. Through electromigration-induced Ag filament formation, the device achieves ultra-high sensitivity, with potential applications in self-adaptive devices and intelligent systems. Furthermore, the device demonstrates versatile cognitive functionalities including classical conditioning and antinociception, marking a significant advancement in bio-inspired artificial systems.

VA.1 Introduction

The human body possesses numerous defensive mechanisms to protect itself from various noxious stimuli that can cause pain and even injury. Upon exposure to harmful stimuli, such as elevated temperature, mechanical strain and so on, nociceptors, which are distributed throughout the nervous system, activate themselves to transmit a warning signal to the brain via the spinal cord[1]. The brain consisting of $\sim 10^{15}$ synapses then processes these signals and takes necessary motor actions to avoid harm to the body. Efforts have been made to draw inspiration from such self-adaptive intelligent systems to emulate brain-like processing at the device level, while fundamentally moving away from the conventional von Neumann computation methods[2]. In this context, nociception behavior in neuromorphic systems has been reported in the literature using either electrical[3–15] or optical pulses[16–21], a relatively higher amplitude pulse representing a harmful stimulus. Some examples exploit external signals from integrated sensors[22–30]. For instance, Yu *et al.* integrated a piezo-resistor to generate input to a synaptic transistor, showing an approach to perform nociception[27]. Similarly, Li *et al.* integrated a temperature sensor with a synaptic transistor for temperature

perception[24]. However, in such instances, the neuromorphic device works rather passively with regard to sensing the harming signal.

Actively mimicking nociception wherein a neuromorphic device directly experiences the external stimulus (pain), remains largely unexplored, and is thus, the subject matter of this article. A few literature examples are listed in Table 1 in the discussion. Contextually, Xu *et al.* reported a stretchable neuromorphic transistor for pain perception using strain as a damaging stimulus[32]. Likewise, a neuromorphic temperature-responsive electric skin has been exploited by Wang *et al.* to emulate the nociception behavior[33]. However, such devices often feature a three-terminal geometry or possess complex structures with additional terminals making it challenging in highly scaled neuromorphic arrays[34]. In contrast, two-terminal devices are widely used in high-scaled memristor crossbar arrays due to their straightforward design, low power consumption, and compact footprint[35]. Importantly, many of the devices listed in Table 1 are non-filamentary and therefore are disadvantageous in several aspects including the absence of integration and firing, poor on/off ratio, requirement of high operating voltage, inadequate memory retention, and so on[36,37]. Conversely, two-terminal neuromorphic devices with Ag as active material have been explored extensively to perform complex cognitive behaviors requiring ultra-low operating energy[38–42]. Consequently, there is a need of the hour to develop a scalable two-terminal system operable at controllable low threshold voltages for mimicking not only the nociceptive behavior but also other higher-order cognitive learnings.

Habituation particularly in the context of pain is intriguing. Human body undergoing repetitive noxious stimuli often adopts it through habituation. For example, when our body senses pain at a modest level quite frequently, one of the common reactions observed is the diminishing of the pain perception, commonly known as antinociception[43]. Such second-order learning behavior can be triggered by various reasons such as fear, shock, and also under the influence of sedatives[44]. Antinociception is often crucial for instance in a post-operative scenario, and therefore generally contributes to the overall well-being of the body[45]. The same is also tied to self-healing ability, regaining sensitivity to external stimuli, and so on[46]. Surprisingly, emulating higher-order antinociception is less common in the literature.

Here, a two-terminal neuromorphic device which employs a Ag microwire network as the active element formed on a stretchable PDMS substrate by the crack-templating method is reported. Crack-templating has proven to be a versatile method for producing various device architectures including large-area transparent conducting electrodes[47,48] and even strain sensors[49–51]. The present device is responsive to the strain and exhibits neuromorphic functionalities that emerge under the influence of mechanical followed by electrical strain. Beyond a threshold strain ($\geq$1.84%, in the given instance) active element becomes electrically open, where it was exploited to initiate a neuromorphic regime. Thus, when activated with electrical pulsing, the device is found to emulate short- and long-term potentiations (STP and LTP), and strain-dependent plasticity with 6-order enhancement in sensitivity in the potentiated state. Besides classical conditioning, importantly, the device exhibits high sensitivity to harmful stimuli (higher strain) mimicking nociception. The device illustrates three distinct stages of pain perception namely, nociception, habituation and antinociception, each representing crucial aspects of pain response. As the pain exceeds the tolerance level, a breakdown regime is also identifiable. The transition between the three stages observed during training sets of pain highlights the device's characteristics of adaptation and learning. Notably, the unique self-healing ability of the device plays a pivotal role in performing such complex tasks.

VA.2 Scope of the present investigation

This thesis chapter explores the design, fabrication, and characterization of a novel biomimetic neuromorphic device with dual functionalities as a mechanosensor and a neuromorphic circuit. The investigation focuses on understanding the device's electromigration-induced conductance-switching mechanism and its potential applications in emulating brain-inspired behaviors. Additionally, the study investigates the device's strain-dependent plasticity adaptation, aiming to control its operating electrical range for self-adaptive devices in intelligent systems. Furthermore, the thesis explores the device's cognitive functionalities, including classical conditioning, nociception, and antinociception, providing insights into its potential applications in advanced brain-inspired technologies. Overall, the work contributes to establishing the device as a fundamental building block for future intelligent systems capable of emulating complex cognitive functions.

VA.3 Experimental methods

Device fabrication

The device was fabricated using the crack templating method on a PDMS substrate.[51] Initially, a crackle precursor was prepared by dissolving an acrylic resin in IPA:water solution (85:15 V/V%) at a concentration of 0.3 g/mL, followed by ultrasonication for 15 minutes at room temperature. Next, stretchable substrates were prepared by mixing PDMS elastomer (Sylgard) and a curing agent at a ratio of 10:1, and subsequently curing at a temperature of 90 °C for 40 minutes. Afterwards, the as-prepared substrate was cut into 2×2 cm^2 pieces and treated with oxygen plasma to increase the surface energy[52]. Thereafter, the crackle precursor solution was uniformly spin-coated onto the substrate at 1000 rpm for 60 seconds. Desiccation of the precursor film resulted in the desired template with interconnected cracks having an average width of 50 μm. Later, 30 nm Ag was deposited on it in a thermal evaporator (ATS 500, HHV, India) fitted with a piezoelectric digital thickness monitor. The following template lift-off in IPA yielded an interconnected Ag microwire network. Ag epoxy was used to take out the electrode contacts.

For the systematic strain application, the device was mounted on a screw gauge with least count of 0.01 mm. The strain induced on the device was calculated using the following equation [53]:

$$\text{Strain (\%)} = \varepsilon\ (\%) = \frac{\Delta L}{L} \times 100$$

where ΔL is the change in the length with applied strain and L is the initial length specifically the distance between the two Ag epoxy contacts. For cantilever-related studies, a steel ruler clamped at one end to a holder was used while the other end hosting the device was left free.

Characterizations

Optical microscopy images were collected using a Keyence microscope (VHX 7000). A field emission scanning electron microscope (FESEM) (Thermofisher Apreo 2S) was employed to visualize the nanogap formation upon strain application. Electrical

characterizations were performed using a Keithley 2450 unit while mounting the device on a screw gauge for strain application.

Numerical simulation

The numerical analysis was carried out using COMSOL Multiphysics 6.2. The geometry was constructed by generating an interpolation curve derived from contour plots extracted from FESEM images. To achieve high precision in the simulation results, an extremely fine physics-controlled mesh was employed.

The electric field distribution was determined by solving Gauss's law, mathematically expressed as:

$$\nabla . \boldsymbol{D} = \rho_V$$

Where $\boldsymbol{D}$ represents the electric displacement field, and ρ_V is the volume charge density (which, in our case, is zero). The relationship between the electric displacement field $\boldsymbol{D}$ and electric field $\boldsymbol{E}$ is given by:

$$\boldsymbol{D} = \epsilon \boldsymbol{E}$$

Here, ϵ denotes the permittivity of the material (For silver, the value at zero frequency is taken as -20000 + 10000i [1]). A potential difference of 2 V was applied across the gap formed in the Ag wire due to the applied mechanical strain.

VA.4 Results and discussion

The device being one of its kind, a conceptual working principle is schematically illustrated in Figure VA.1 representing distinct operational ranges of the dual-functional device, as a strain sensor in a low strain range and as a neuromorphic device under higher strain, as detailed below. The low and high resistance states (LRS and HRS) in the strain first regime are denoted as R_{LRS} and R_{HRS}, respectively. Whereas the resistance states encountered in the neuromorphic potentiated regime are distantly different and termed, N_{LRS} and N_{HRS}. This differentiation in terminology highlights the multifaceted nature of resistance states under various operational ranges.

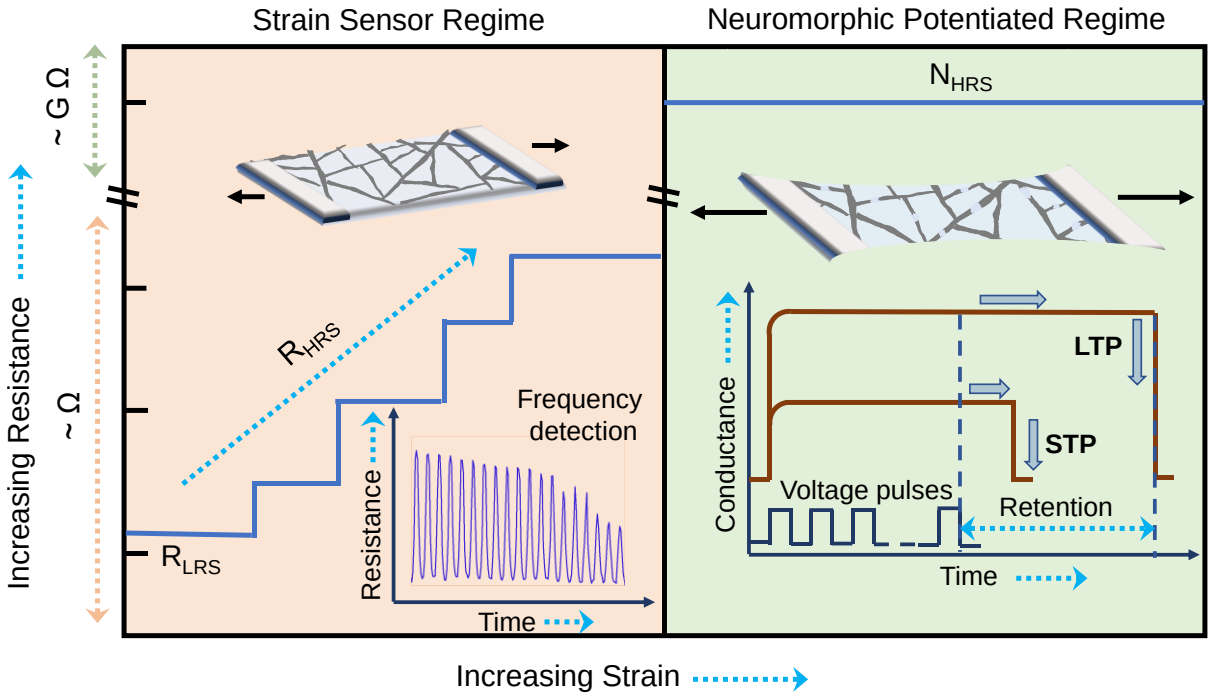

Figure VA.1: Activation of neuromorphic regime. Schematic representation of the strain-induced electrical response from a percolating Ag microwire network. In the low strain range (left panel), the device works as a strain sensor as a result of partial breaking of the network. With increasing strain (right panel), the device becomes nonconducting, where it is made to serve as a neuromorphic system. By feeding in electrical pulses, the device is activated to neuromorphic low resistance states (N_{LRS}) enabling emulation of synaptic activities.

The device fabrication entails various key steps (see Figure VA.2a) starting from the formation of interconnected microcracks (shown in the optical microscopy image in Figure VA.2b) in a sacrificial desiccated film on a pre-formed PDMS substrate (see the Experimental section for details). The step was followed by Ag deposition via thermal evaporation and lifting-off of the crack template in IPA to bring about a complimentary structure comprising of Ag microwire network, as shown in optical microscopy images in Figure VA.2c and inset. The fabrication was completed by taking electrical contacts out from the remote ends of the network. Due to the micro-sized feature of the Ag wires, the device is visibly transparent (T ~ 74%), as clearly seen in the plot in Figure VA.2d and the overlaid photograph. At first, the sensitivity of the device to strain was examined by fixing it onto a screw gauge (with Ag contacts strategically positioned outside the strain area) to induce strain while continuously monitoring the device resistance. The as-prepared device exhibited LRS (~ 100 Ω) due to the percolating Ag microwire network connecting the electrodes. With the increasing strain (ε), it showed a relative change in resistance ($\Delta R/R_0 = (R-R_0)/R_0$ where R_0 and R are the resistances at relaxed and strained states).

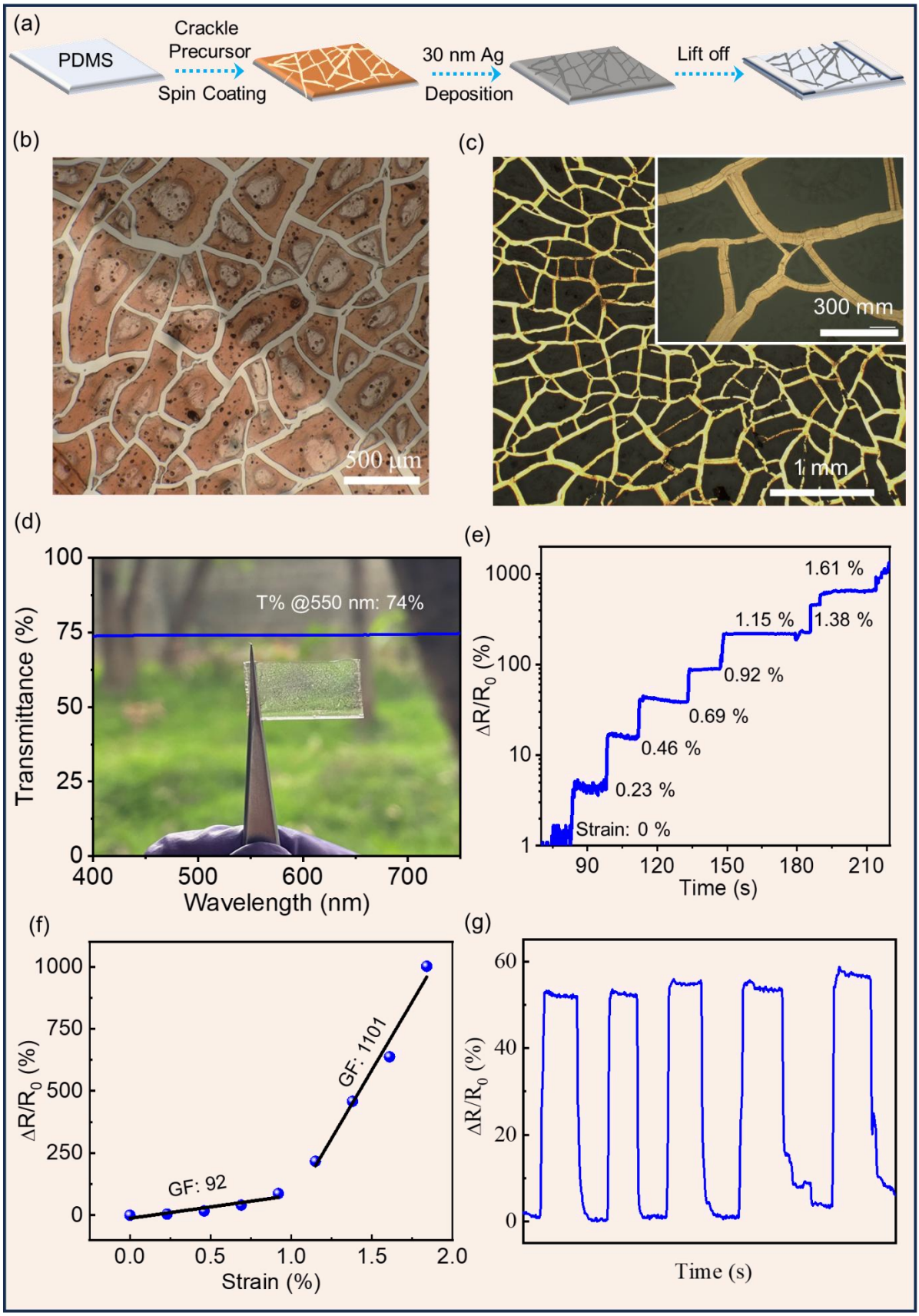

Figure VA.2: Strain sensitivity (a) Schematic of the fabrication protocol involving precursor coating on a stretchable substrate to form a desiccated crackle template, followed by Ag deposition and template lift-off. (b) Optical Microscopy image of the micro-crack network achieved after crackle precursor spin coating. (c) Optical

Microscopy image of Ag microwire network (reflective) with inset showing a magnified view. (d) Visible transmittance (T) overlaid with a photograph of the device. (e) Strain-dependent change in resistance of the device. (f) Two linear regimes with different gauge factors (GF) in low and high strain ranges. (g) Repeated cycles of resistance change at 0.69% strain.

Depending upon the strain value, resistance switches to various R_{HRS} states, as depicted in Figure VA.2e. The variation in R_{HRS} attained upon successive strain application follows a linear trend to result in a gauge factor (GF) of 92 in the strain range $0 < \varepsilon < 0.92$, while at higher strains ($1.15 < \varepsilon < 1.84$), the GF increased significantly beyond 1100 (Figure VA.2f). The application and removal of strain cause respectively the opening and closing of nanogaps across the Ag microwire network resulting in a change in resistance and this is realisable over repeated cycles (Figure VA.2g)[51].

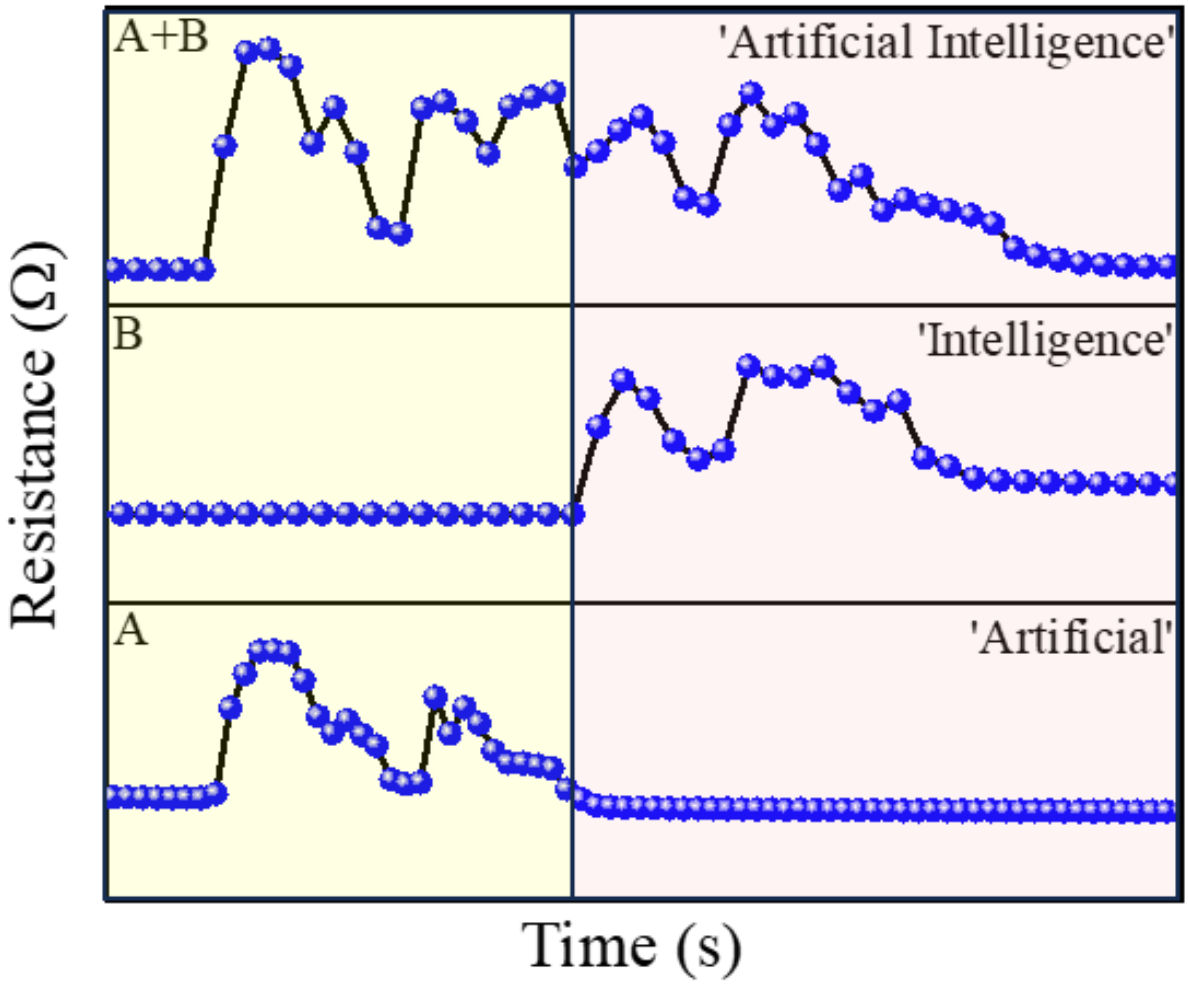

Figure VA.3: Speech recognition: distinguished resistance pattern generations by the device while playing the words 'artificial' (A) and 'intelligence' (B) individually and consecutively (A+B) on a cell phone speaker hosting the device, giving rise to (A) + (B) = (A+B). The inset shows a photograph of the device placed on the speaker.

The strain sensing capability of the device was extended to speech recognition where it detected individual letters pronounced through a speaker and precisely tracked the vibrations associated with it, the latter serving as external strain (Figure VA.3). The device is exploited in speech recognition applications. To demonstrate so, it was mounted on a cell phone speaker to capture the response of spoken words. The aim was to distinctly record the response of two words 'Artificial (A)' and 'Intelligence (B)' through the resistance change produced in the device. A constant voltage bias was employed by a source meter to record the resistance change. Initially, the word 'Artificial' (represented by A) was played and the intricate resistance change produced by the word was recorded. Next, the word 'intelligence' (represented by B) was played and recorded in a similar manner. Finally, both the words were played consecutively, and it produced the sum of the patterns produced by A and B. This functionality highlights its potential to capture subtle acoustic details with precision. Leveraging its inherent flexibility and high sensitivity, the device was further explored for the detection of the frequency of a cantilever, affirming the adaptability of the device in various sensing applications (Figure VA.4). To perform cantilever frequency detection, the device was mounted on a one-edge clamped cantilever (sturdy steel scale) (as shown in Figure VA.4a) and a deflection was induced to the free end resulted in a damped oscillation that in turn, gives rise to resistance change in the device (see Figure VA.4b). As the cantilever length varied systematically, it gave rise to distinct frequencies each corresponding to a different cantilever length as depicted in Figure VA.4b All the corresponding curves used for the frequency calculation are shown in Figure VA.4c-f. Previous studies from the laboratory have brought out successful instances of such applications[50,51].

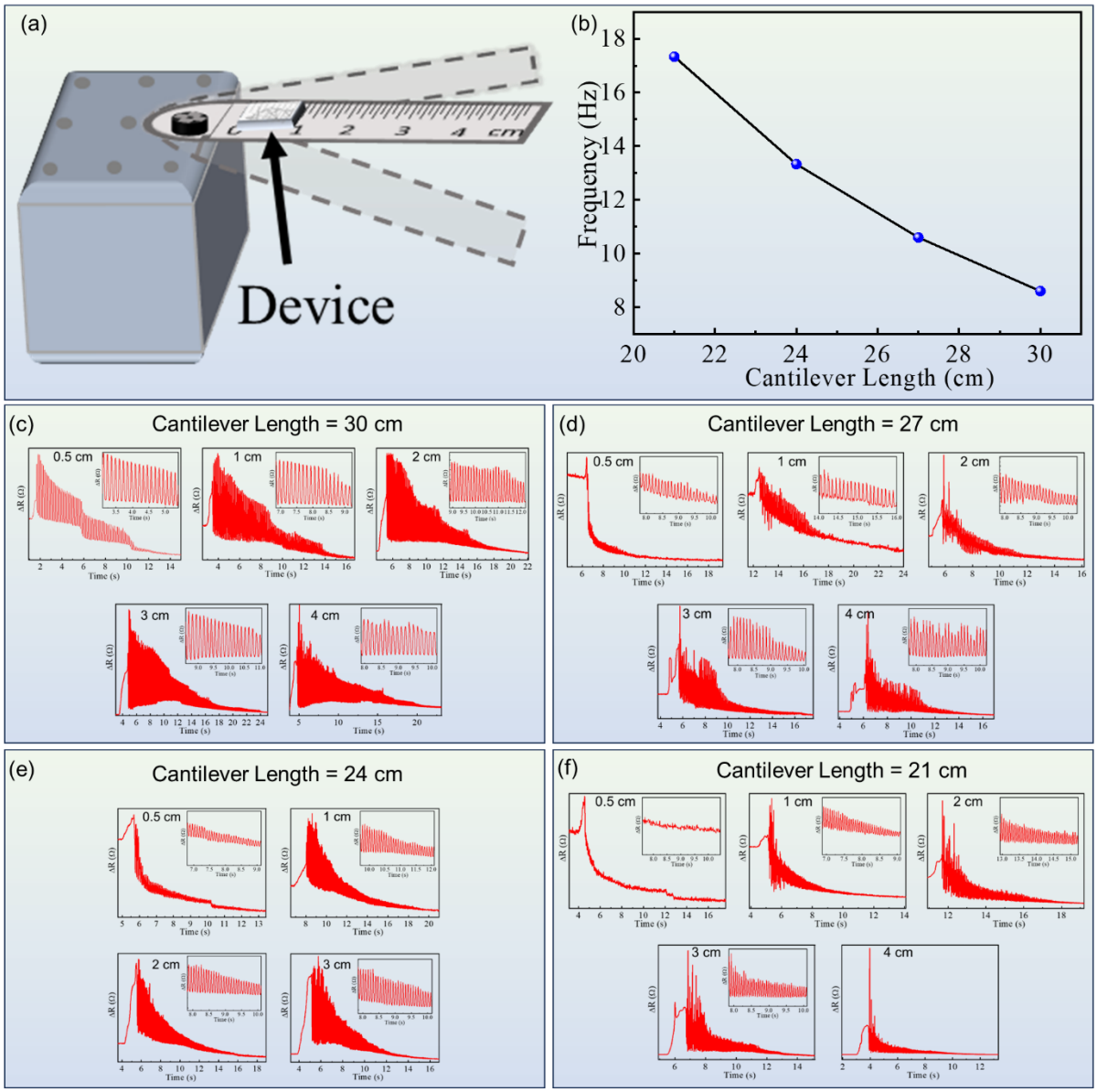

Figure VA.4: Mechanical frequency detection: precise identification of the length-dependent natural frequency of a cantilever subjected to mechanical vibration. (a) Schematic of the experimental setup where the device is placed on a cantilever. (b) Variation of the frequency with the cantilever length. Corresponding response of the sensor subjected to damped oscillations at (c) 30 cm (d) 27 cm (e) 24 cm (f) 21 cm cantilever length with an initial deflection from 0.5 cm to 4 cm. Insets are the corresponding enlarged oscillation patterns.

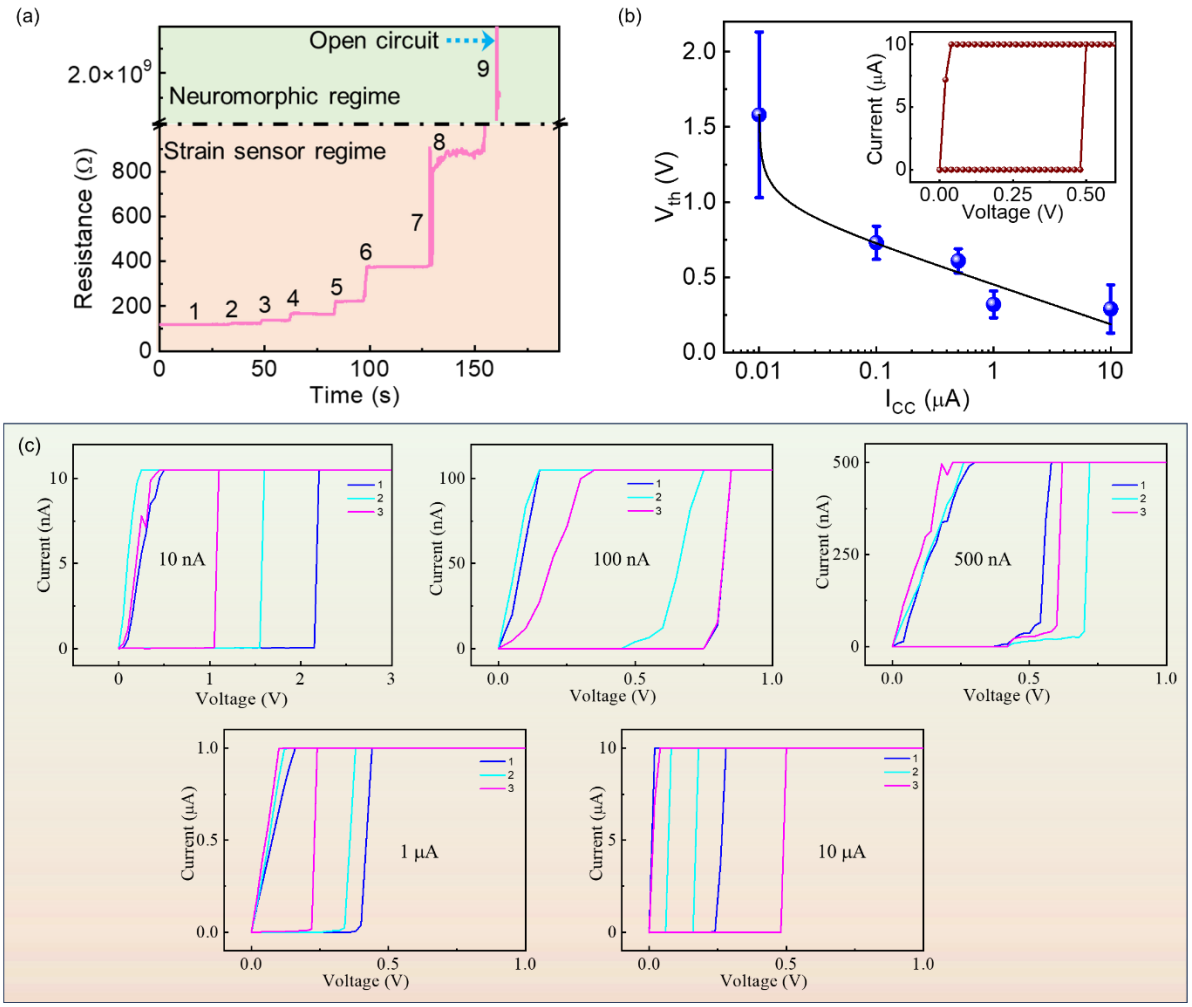

Figure VA.5: Neuromorphic regime (a) Plot showing the strain-induced transition from R_{LRS} to various R_{HRS}, each step represents the increasing strain of 0.23%. The numbers from 1 to 8 fall in the strain sensor regime while number 9 is in the neuromorphic working regime. (b) Variation of threshold voltage (V_{th}) with the change in current compliance (I_{CC}) at 0% ΔS. The inset shows the I-V switching behavior at I_{CC} of 10 μA. (c) Corresponding I-V sweeps showing threshold switching at the different I_{CC} values.

Figure VA.5a illustrates the R_{LRS} state (indicated by 1) alongside other R_{HRS} states (2 to 8) brought about by stepwise (0.23%) incremental strain. Further increment in strain (1.84% and beyond) renders the device electrically open (OC) designated as N_{HRS}, which is the HRS of the neuromorphic regime or neuromorphic inactivated regime of the device. Thus, with the present device, a strain value of 1.84% serves as the reference for neuromorphic measurements such that an additional strain is counted as the incremental strain, ΔS. During forward I-V sweeps (inset of Figure VA.5b), the N_{HRS} undergoes a volatile resistive switching to N_{LRS} beyond a certain threshold voltage (V_{th}) and returns to the N_{HRS} with a substantial hysteresis. The formation of a conducting path across the nanogaps is accountable for the observed switching behavior which is elaborated later. The I-V sweeps were performed at different I_{CC} values (10 nA to 10 μA) and the variation of V_{th} was

studied (Figure VA.5c). It showed a decrement in V_{th} with the increasing I_{CC} as depicted in Figure VA.5b.

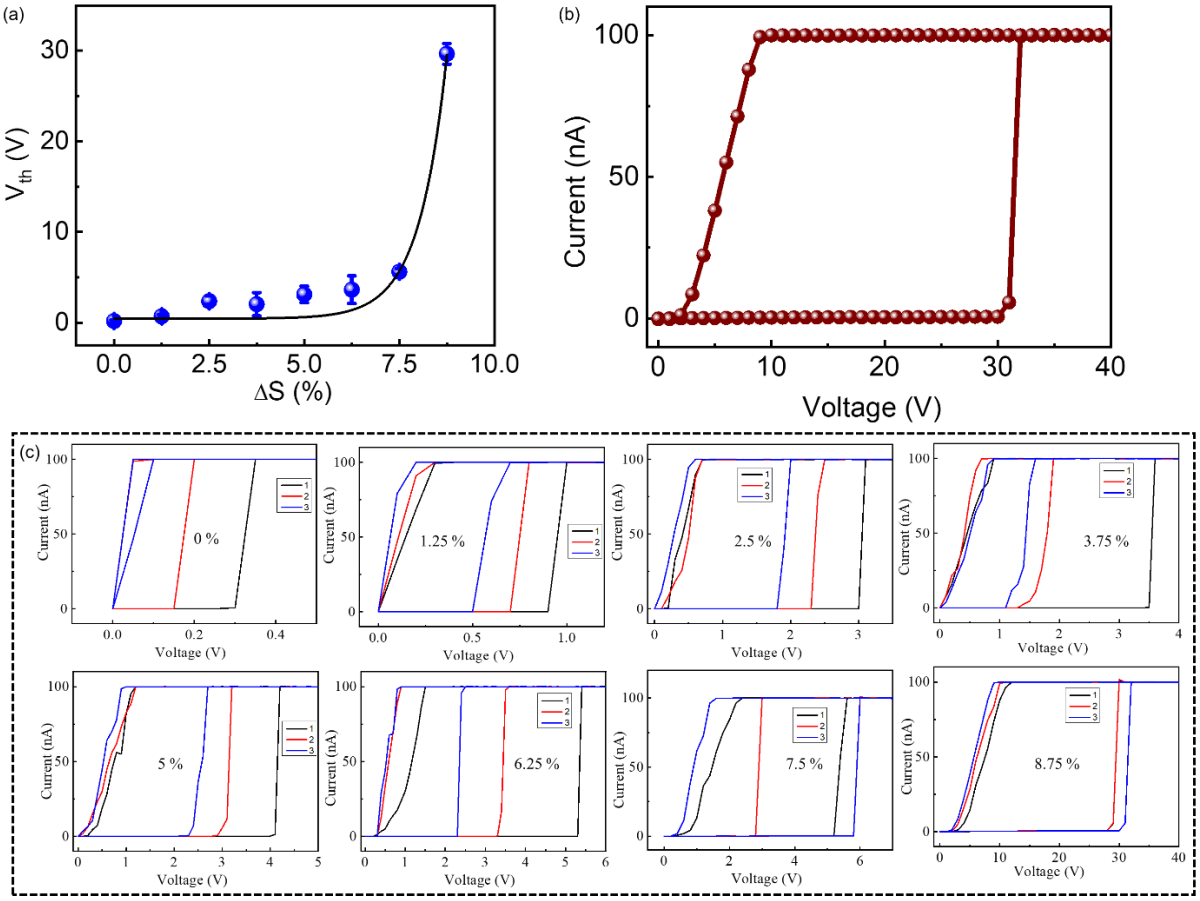

Figure VA.6: Strain-dependent switching (a) Variation in V_{th} with strain in the neuromorphic regime. (b) I-V loop under an incremental strain, ΔS of 8.75%. (c) Corresponding I-V sweeps at various ΔS values. Error bars represent the standard deviation in V_{th}.

The V_{th} variation was also examined with different levels of applied ΔS, as shown in Figure VA.6a and c. As ΔS increased, larger nanogaps were formed requiring a higher V_{th} to bridge the extended gaps. Thus, by varying the strain, V_{th} can be desirably tuned. This also helps in self-healing the device to regain its functionality after a large deformation or breakdown.

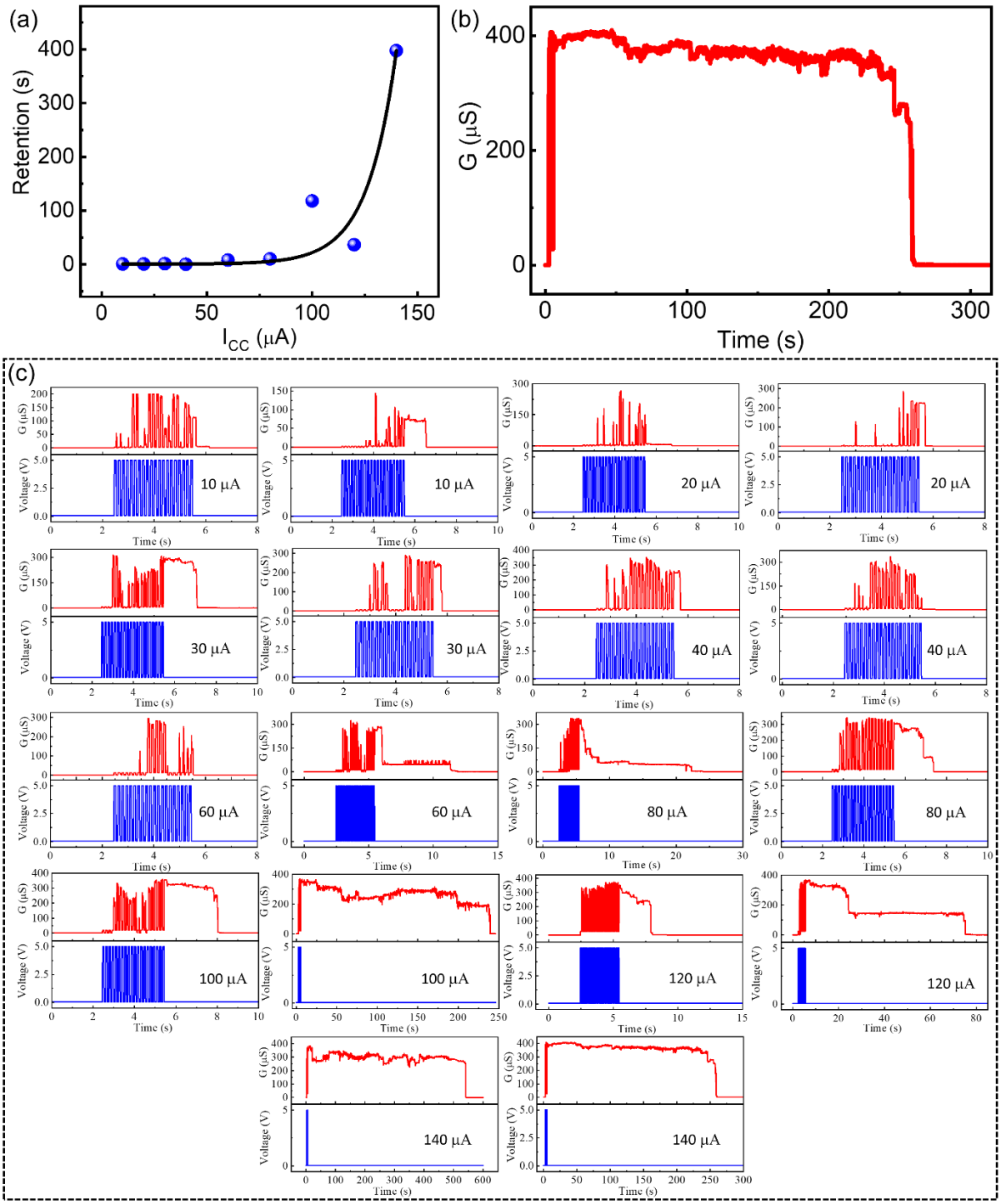

Figure VA.7: Compliance governed plasticity (a) Variation of the conductance retention in the potentiated state with increasing I_{CC}. (b) Conductance retention behavior of the device at I_{CC} = 140 μA. (c) Corresponding retention curves measured at different I_{CC} values.

In addition, the plasticity behavior was investigated by applying 20 pulses of 5 V at various I_{CC} while monitoring the conductance retention with a reading voltage of 10 mV (Figure VA.7a). The device exhibits a STP behavior at lower I_{CC} and transitions to LTP at

elevated I_{CC} (Figure VA.7a). The device shows retention up to 250 seconds at 140 µA I_{CC} (Figure VA.7b).

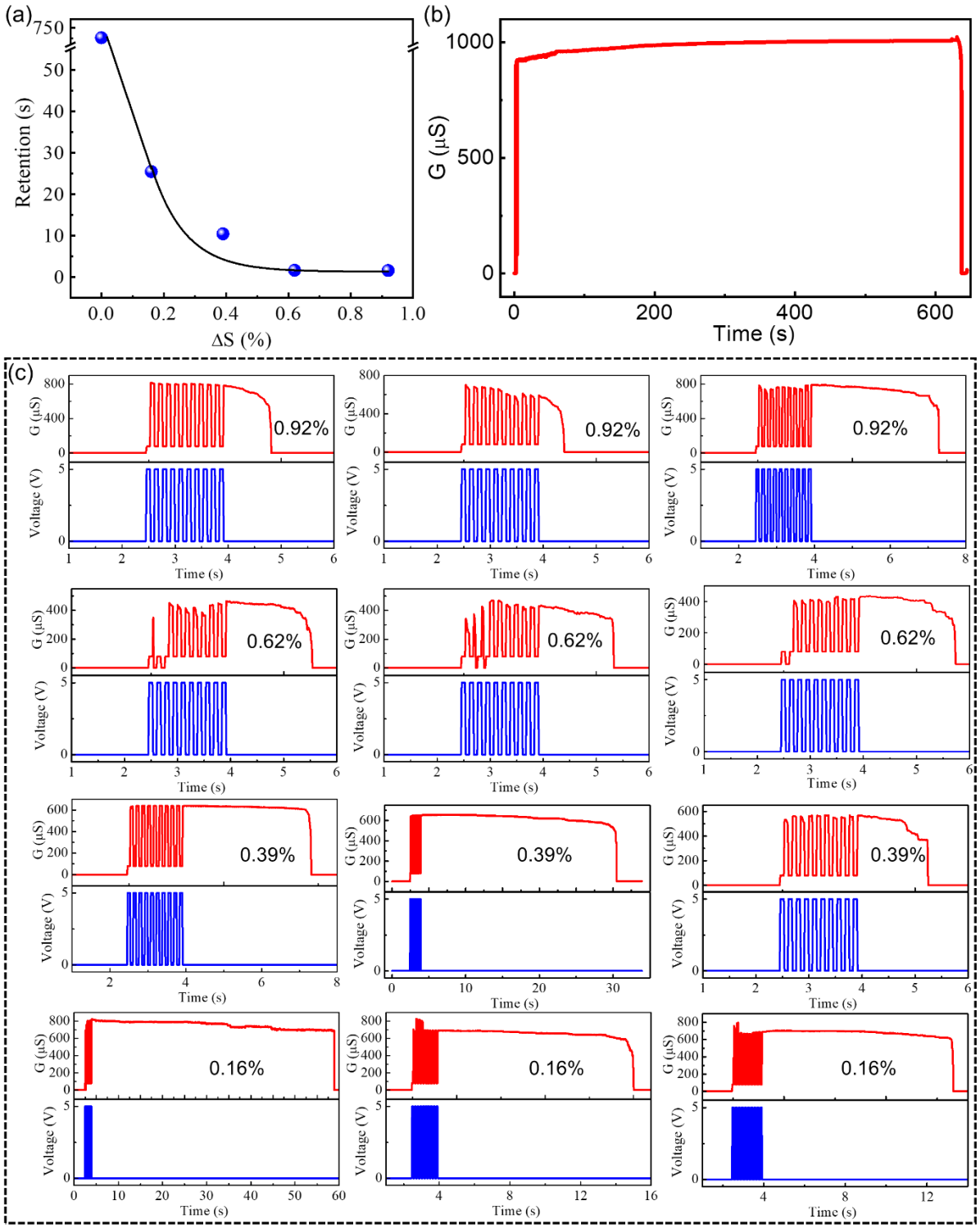

Figure VA.8: Strain-dependent plasticity (a) Variation of the conductance retention in the potentiated state with increasing ΔS. (b) Conductance retention behavior of the device at 0% ΔS.(c) Corresponding retention curves measured at different ΔS values.

Similar retention characterizations were also conducted at different ΔS values (Figure VA.8a). The device shows retention up to 600 seconds at 0% ΔS value (Figure VA.8b). However, for a similar pulsing condition, the device retention decreases as the strain increases (Figure VA.8c). This implies that the learning capability of the device effectively decreases at higher strain. This behavior is akin to human cognition. Under stress, for example, an individual's ability to read and absorb information may be adversely affected.

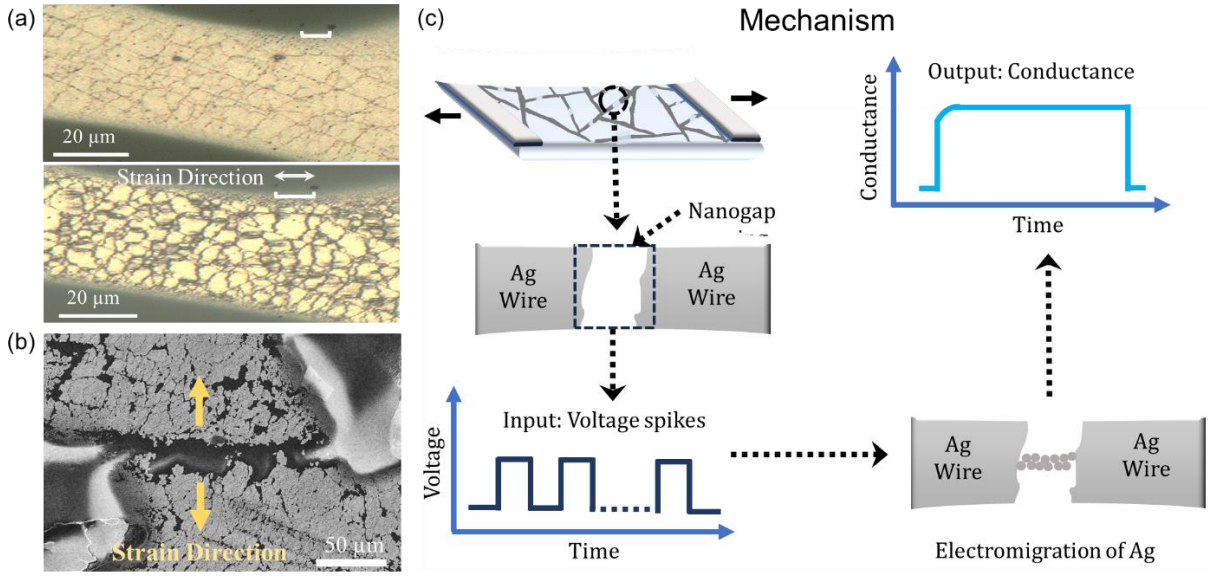

Figure VA.9: Working mechanism (a) Optical microscopy images of the device before and after the strain application. (b) SEM image depicting the formation of gaps with the application of strain. (c) Schematic explaining the working mechanism of the device. An applied strain to the device stimulates nanogaps in the Ag microwire network to form N_{HRS}. With the application of electrical pulses, conducting paths appear in those gaps due to growing nanofilaments, leading to N_{LRS} and other synaptic activities.

Mechanistically, the whole process may be understood as follows. The applied strain induces several nanogaps along the stretching direction, as evidenced in the optical image in Figure VA.9a and the FESEM image in Figure VA.9b. The application of voltage pulses triggers the electromigration of Ag[54] across these gaps. The process leads to the formation of conduction bridges or nanofilaments, thereby decreasing the resistance of the device (see the schematic representation of the working mechanism in Figure VA.9c). A higher I_{CC} leads to enhanced electromigration facilitating the formation of strong filaments which enable the device to retain the LRS for a longer time as illustrated in Figure VA.7a[39]. Also, higher strain hosting larger nanogaps may trigger the formation of long but weak filaments during pulsing, leading to limited retention or STP, thereby elucidating strain-dependent plasticity (see Figure VA.8a).

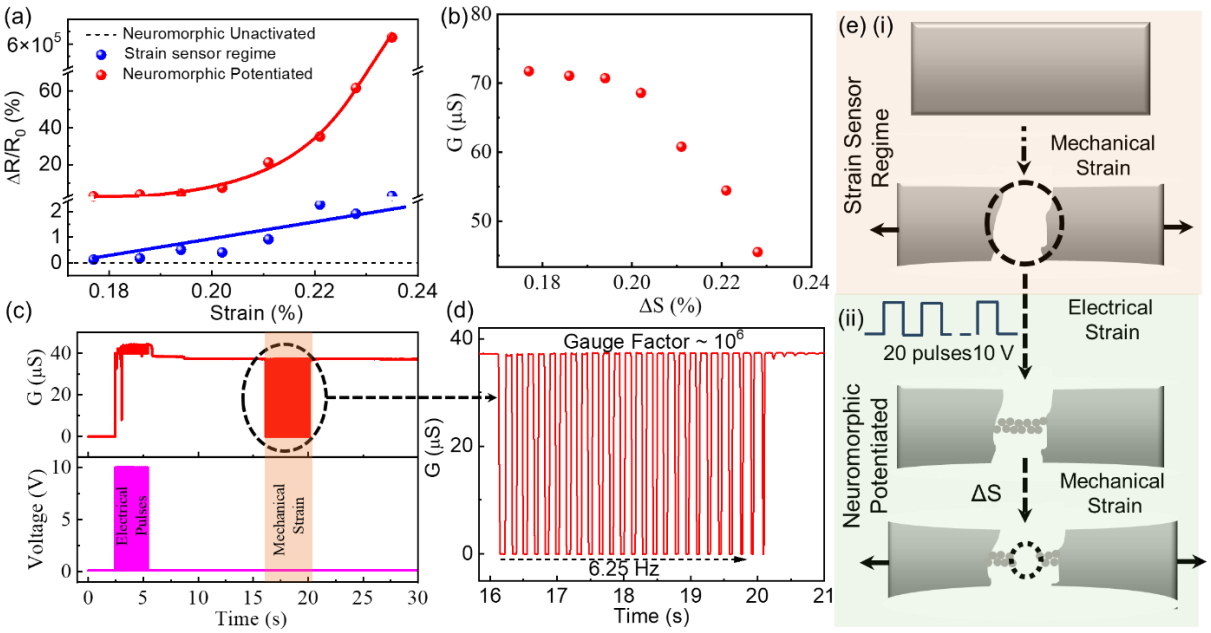

Figure VA.10: Sensitivity enhancement (a) Plot representing that the strain sensitivity increases manyfold at its neuromorphic potentiated state. (b) The conductance variation with ΔS in the neuromorphic potentiated regime. (c) Oscillatory strain (0.25%) application to the potentiated device. (d) A zoomed-in plot representing enhanced GF. The periodic oscillation of N_{HRS} and N_{LRS} resulted in a frequency of 6.25 Hz. (e) Schematic representation of the mechanism for the enhanced GF in the potentiated state.

Interestingly, the device in a potentiated state exhibits much higher sensitivity. For validation, the device was kept on a cantilever (see Figure VA.4a) and deflections were applied to induce different levels of strain. This experiment was conducted at three distinct operating regimes, namely the strain sensor regime, neuromorphic inactivated as well as neuromorphic potentiated regime (see Figure VA.10a). In the strain sensor regime, the device experienced minimal resistance change of ~ 2% at 0.23% strain. This is due to an ohmic conduction in the low strain range. On the other hand, no resistance change was detected in the inactivated regime, as the device was already in the open circuit (OC) state. Contrastingly, the potentiated device (using 20 pulses of 10 V) exhibited a remarkable improvement in sensitivity by up to 30 times! More specifically, the resistance change increased exponentially attaining a sharp increase in sensitivity of the order of 10^5 at a strain of 0.24%. This could be attributed to a widening of the nanogaps upon straining the device, where the exponential variation might be due to the conduction via tunnelling[55], as supported by the observed conductance values (Figure VA.10b) are below the quantum conductance (G_o, 77.5 μS).

The enhanced sensitivity was also observed in another set of experiments where instead of giving an incremental deflection, the potentiated device was subjected to oscillatory ΔS

(a deflection of 5 cm amounts to 0.25% strain). This mechanical modulation triggered a fascinating periodic switching of the conductance state between N_{LRS} and N_{HRS} as illustrated in Figure VA.10c. While doing so, the device generates digital states such as 0 (N_{HRS}) and 1 (N_{LRS}) with a certain frequency (Figure VA.10d). The frequency of the periodic switching was observed to be 6.25 Hz which is close to the theoretically calculated frequency (6.52 Hz) of the cantilever. The theoretical frequency of cantilever oscillation was calculated using the equation[56]:

$$\omega = 1.875^2 \left(\frac{Eh^2}{12\rho L^4}\right) \text{ rad s}^{-1}$$

where E is Young's modulus (Nm^{-2}), h is the thickness of the cantilever (m), ρ is the density of the cantilever-material (kg m^{-3}) and L is the length of the cantilever (m). In the present experiment, the cantilever is a "steel scale" having E = 2.1 × 10^{11} N m^{-2}, h = 0.00047 m, ρ = 7850 kg m^{-3}, and L = 0.245 m. Therefore, the calculated circular natural frequency for the cantilever beam is.

$$\omega = 41.0 \text{ rad s}^{-1} = 6.52 \text{ Hz}$$

The device, previously demonstrating the analog states now exhibits the capability to generate digital states of 1 and 0 under oscillatory strain. This highlights its adaptability for use in both digital and analog applications. The device producing periodic 1 and 0 states can also act as a ring oscillator, a crucial component used in clock generators, ensuring synchronization in the communication network[57]. The enhanced sensitivity could be ascribed to the active participation of narrow filaments formed across the nanogaps in the potentiated state. Figure VA.10e depicts the mechanism underlying the enhanced GF in the potentiated device. In the pristine device (Figure VA.10e(i)), strain triggers the formation of nanogaps in the Ag wire of width being in the micron range. Whereas, in the potentiated device (Figure VA.10e(ii)), the nanofilaments, being the weakest points across the network, majorly participate in the strain response. Therefore, unlike the micro-sized wires, nanofilaments break at a much lower strain, amplifying the overall GF.

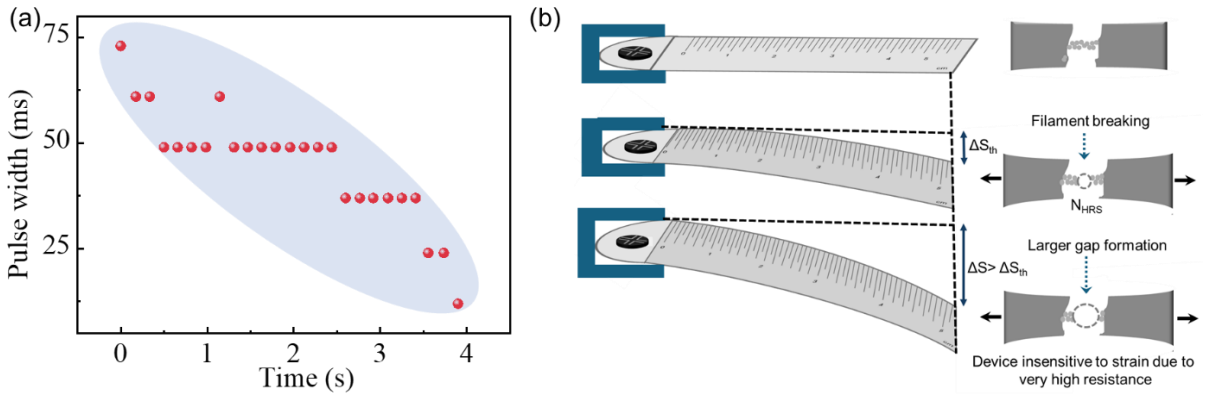

Figure VA.11: Oscillation damping (a) Variation in the oscillatory pulse width with oscillation damping time. (b) Schematic explanation of the mechanism of the device during oscillatory strain.

The oscillation of a cantilever typically manifests as damped oscillation, wherein the amplitude of the oscillation gradually diminishes and eventually ceases, attributed to the dissipative effect of air resistance[58]. Surprisingly, here the oscillations produce the periodic square waveforms in which the width of the waveform goes on decreasing (Figure VA.11a). The decrement of width with time shows the damping detected by the device. Also, after a certain point of time, the periodic square waveforms were not detected (Figure VA.10d). This threshold may be understood as the minimum deflection (d_{th}) causing minimum strain ΔS (ΔS_{th}) to break filaments causing the device to switch to N_{HRS}. The ΔS value applied in Figure VA.11b is larger than the ΔS_{th} due to which the device produces periodic switching. However, once the oscillation dampens the ΔS decreases below ΔS_{th} resulting in the diminishing of the 0 to 1 transition (schematically depicted in Figure VA.11b). The GF calculated using the resistance change during the periodic switching was found to be ~ 10^6, a few orders higher compared to that of a non-potentiated counterpart.

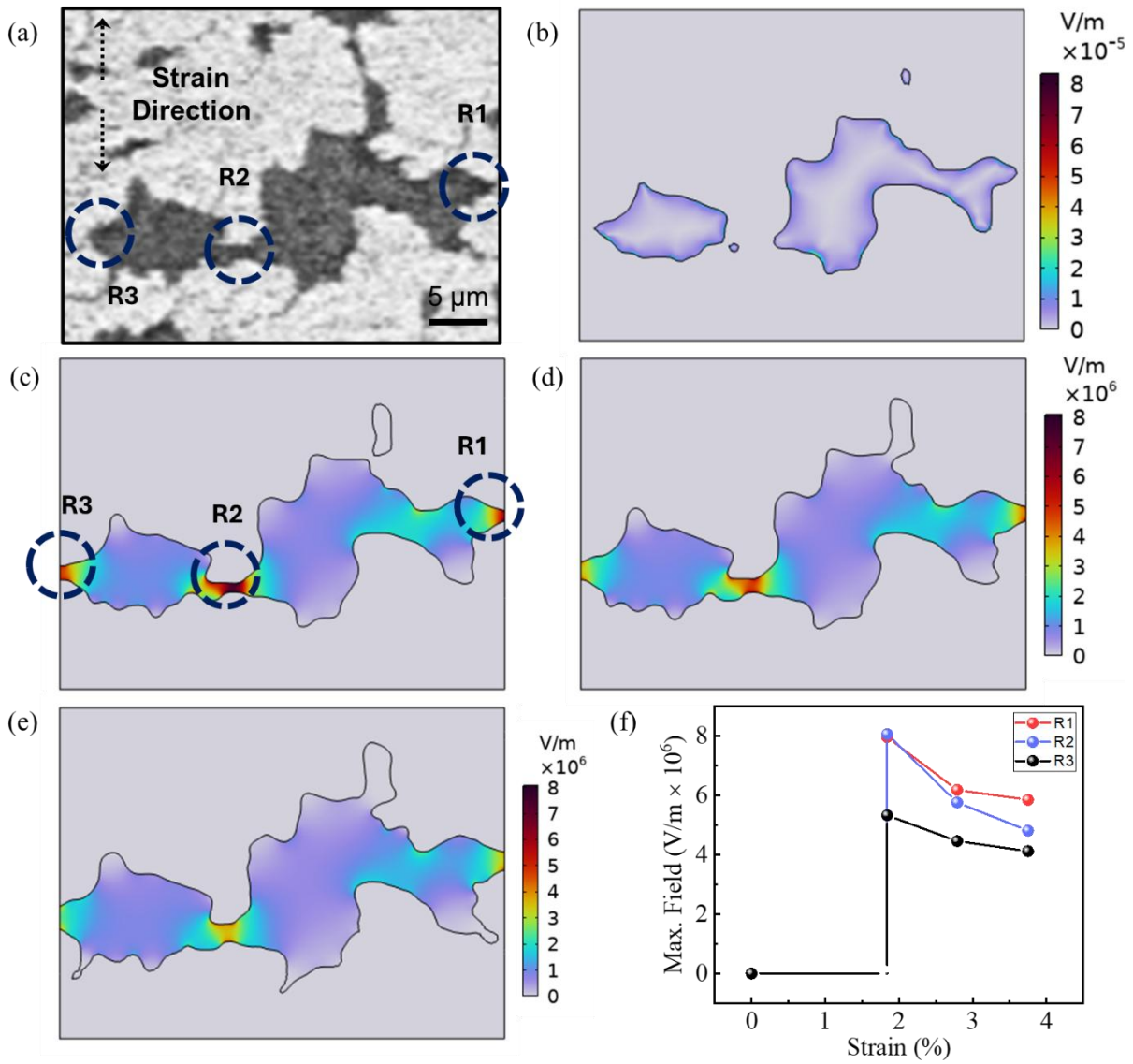

Figure VA.12: COMSOL simulation depicting electric field distribution across strain-induced gaps (a) SEM image illustrating gap formed due to applied strain of 3.75 %. Electric field distribution at 2 V across the gap, visualized at strain values of (b) 0 %, (c) 1.84 %, (d) 2.79 %, and (e) 3.75 %. (The gap in (e) corresponds to the SEM image (a), whereas the gaps in (d), (c), and (b) were generated by eroding the preceding gaps using Python's erosion operation.) (f) Variation of maximum electric field within regions R1, R2, and R3 (marked in (a) and (c)) with strain.

To elucidate the mechanism of filament formation, electric field simulations using COMSOL were conducted. Figure VA.12a displays a magnified SEM image of the gap formed in the Ag wire due to applied mechanical strain. When voltage is applied, the electric field in localized regions with minimal gaps (denoted as R1, R2, and R3 in Figure VA.12a) between Ag electrodes experiences substantial intensification (refer to Figures VA.12c-e). Based on the observed field distribution, a mechanistic explanation for filament formation in nanogaps within Ag wires is proposed. Upon the application of a potential difference, the electric field within these nanogaps surpasses the breakdown

strength of air (3×10^6 V/m). However, the peak field strength diminishes with increasing strain, as shown in Figure VA.12f. This trend is expected, as larger gaps form at higher strain values. This intensified electric field can cause air ionization or breakdown[59,60]. The resultant ionized air molecules are then accelerated towards the opposing electrode, colliding with other air molecules along their trajectory and generating an ionic wind[61]. This ionic wind has the potential to initiate an electrical arc or spark between two Ag electrodes[62]. The high local current density and point heating induced by the electric arc lead to transient explosions of small volumes of metals, accompanied by the production of Ectons[63,64]. The expelled Ag nanoparticles are then driven towards the region of the strongest electric field, effectively bridging the gap in the Ag wire and establishing conductive filamentary paths.

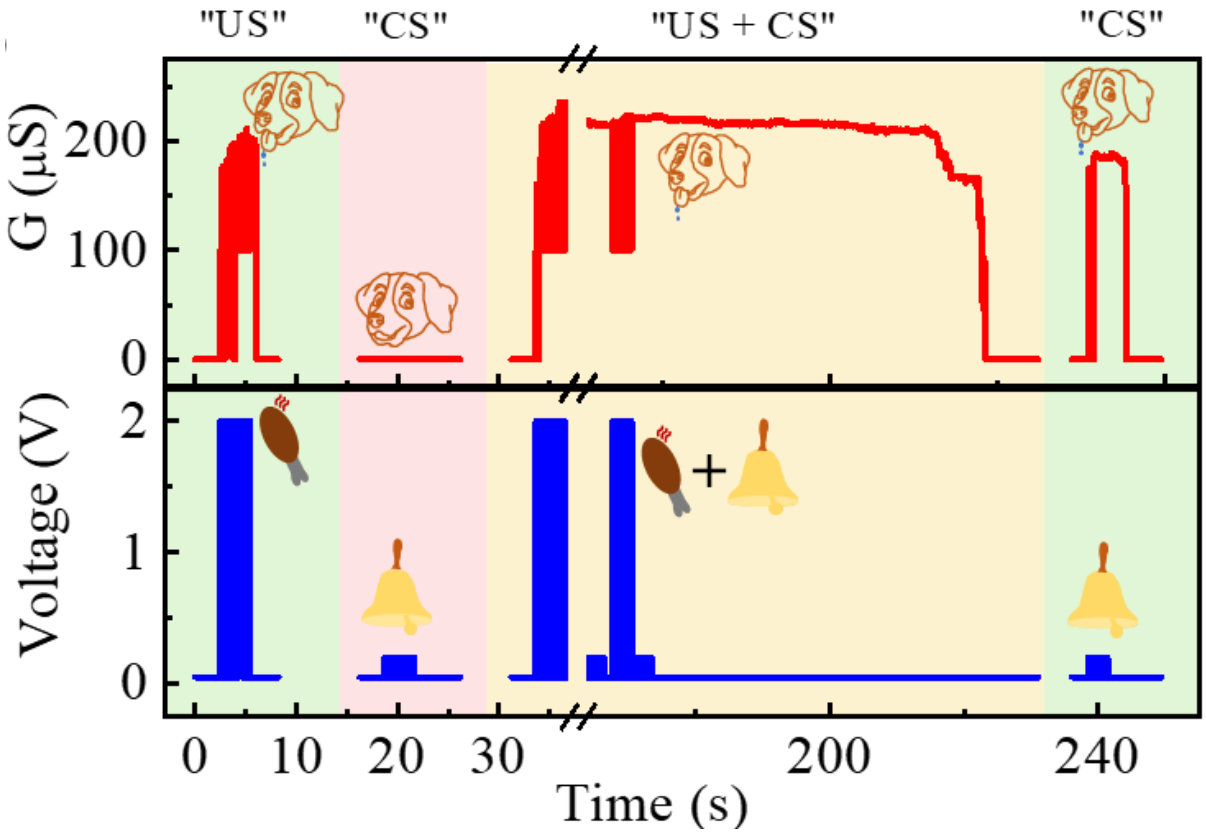

Figure VA.13: Classical conditioning. Simulating the classical conditioning by applying 2 and 0.2 V pulses as food and bell, respectively.

Following the above validation, the device was further exploited to emulate brain-inspired cognitive actions. In the niche, classical conditioning is extensively studied in the literature and is considered a benchmark experiment for neuromorphic devices[65]. The classical conditioning emulation using the device process involved simultaneous training with stronger (2 V) and weaker (0.5 V) pulses, where the latter alone is incapable of

producing a response. Herein, optimum voltage pulses were utilized as food (2 V) and bell (0.5 V) to perform the device-level classical conditioning while monitoring the response using a reading voltage of 50 mV. Food stimulus is the unconditional stimulus (US) which always generates a complete response contrasting to the bell or the conditional stimulus (CS) which is expected to generate a response only after the conditioning.

The device was first subjected to a sequence of food pulses which generated a conductance response depicting the unconditional reaction (Figure VA.13). When the device was subjected to a sequence of bell pulses, no response was observed. Next, 20 sets of food and bell pulse sequences were applied successively. Post-training, the application of bell signals generated the conditional response, indicating a successful emulation of classical conditioning (Figure VA.13). The ability showcases the potential of the device for emulating fundamental cognitive processes.

Additionally, second-order cognitive learning, namely antinociception or habituation to pain has also been accomplished for the first time at the device level since it responds uniquely to strain, unlike the conventional ones. In this context, a scenario can be imagined where a person is given pain by beating him with a stick frequently (Figure VA.14a). If the scenario repeats, the person experiences pain for the initial few days, but over time, gets habituated and shows no response to pain. The strain-responsive device has been exploited to emulate such complex cognitive learning while using strain as the pain stimulus, as demonstrated in Figure VA.14b-e. To begin with, ΔS of 0.25% was applied to a potentiated device (1), resulting in a sharp drop in the conductance (2 to 3), representing the response to pain or nociceptive behavior (Figure VA.14b). However, when the strain was removed, the conductance recovered (4 to 5), but to a reduced level compared to the initial value. The reduction is defined as the pain sensation (pain: percentage change in the conductance with respect to the potentiated state), which decreased (5 to 6) gradually in the absence of strain, illustrating forgetting or recovering from the pain sensation. During this recovery, the strain was applied again, causing the device to go back to HRS (6 to 7), marking the second nociception.

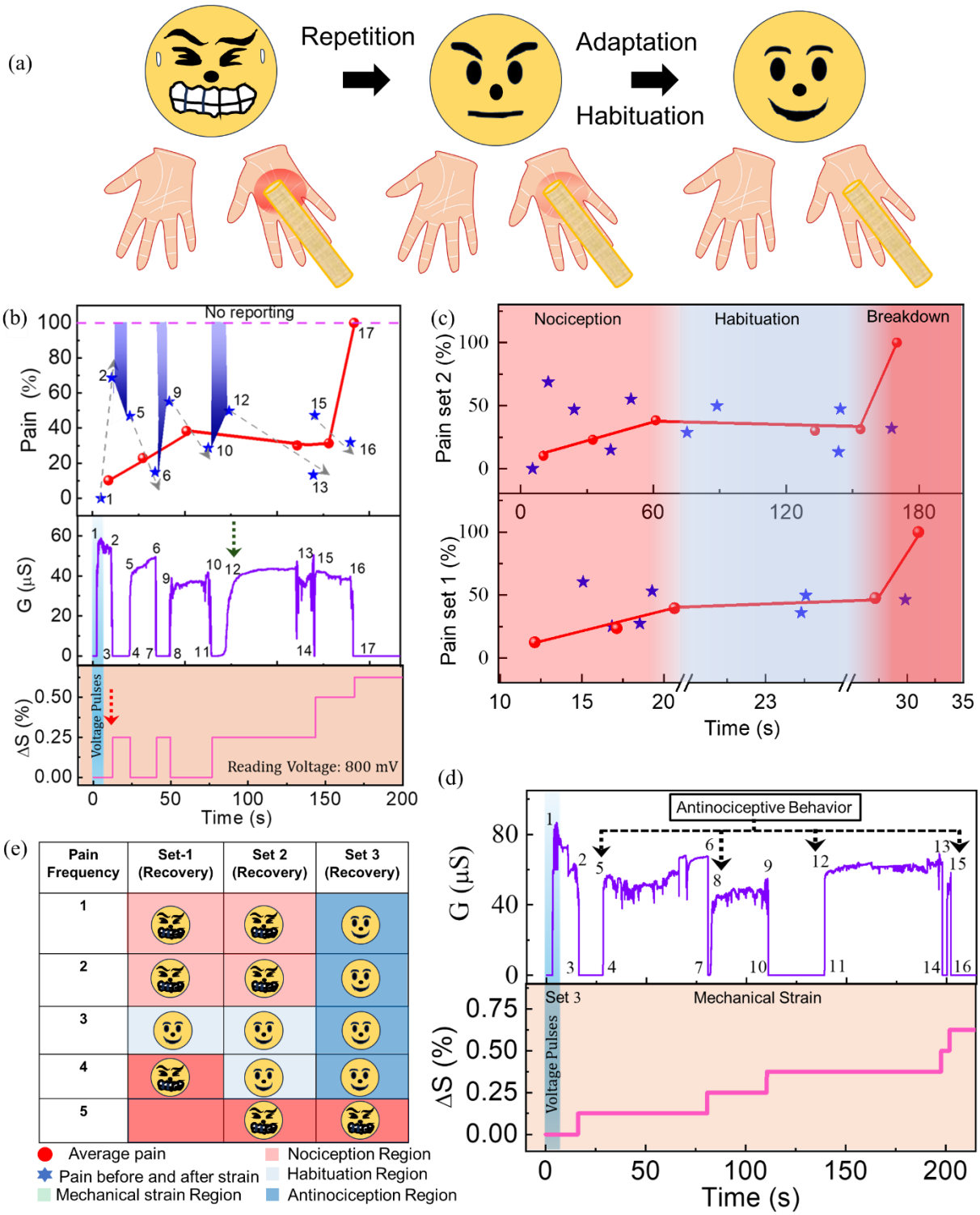

Figure VA.14: Nociception and antinociception behavior (a) Schematic representation of the pain habituation, also known as antinociception. (b) Conductance variation with time upon repetitive strain application of varied magnitudes, representing pain (defined as the conductance decrement from the ΔS=0 potentiated state) habituation followed by breakdown beyond an unbearable pain (no reporting). (c) The evolution of pain from two repetitive data sets, differentiating nociception, habituation, and breakdown regimes. (d) The conductance recovery of the device under strain, depicts self-healing and antinociception, a second-order cognitive learning. (e) Table showing the

recovery under strain for 3 different sets of measurements, portraying a transition from pain sensation to habituation and adaptation.

After the strain removal (8), the pain increased (9) compared to the previous cycle, depicting a high impact of the pain affecting the recovery from pain (9 to 10). Upon further application of strain, the device switched to HRS (11) but importantly, recovered the conductance (12) despite the strain being present. This implies the first impression of antinociception. When the average conductance in each cycle was plotted against time (red curve in Figure VA.14b), a plateau was observed representing the habituation. After the sensitization, further increment in strain (13) could not affect the conductance, showing the increased habituation to the pain. However, beyond a certain limit ($\Delta S \sim 0.625\%$), the device failed to hold the conductance state (17), depicting unbearable pain and a permanent damage state. The repeated experiment (see Figure VA.14c) also validated a similar trend of initial pain feeling (regime 1), followed by habituation due to antinociception (regime 2) and then breakdown (regime 3). After the two sets of training when the device was subjected to strain in set 3 (Figure VA.14d), the conductance recovered with every application of strain until the breakdown. The behavior represents a strong antinociception and self-healing of the device. As tabulated and summarized in Figure VA.14e, the three sets of training clearly indicate a transition from nociceptive to antinociceptive behavior through habituation.

The multifunctional device's ability to tune its resistance via inducing external strain in the network enables it to be one of the most suited wearable artificial synaptic networks (ASNs). Higher strain triggers the formation of many nanogaps across the percolating nanowire resembling structural similarities to a biological neural network, nanogaps being the synaptic cleft while the intermediate microwires serve as the neurons. The GF enhanced to $\sim 10^6$ in the potentiated state outperforming most of the reported literature[66–68]. The transition from being conducting to non-conducting beyond a certain strain range can be compared to the nociceptive action of biological neurons, where external stress be it thermal, mechanical, or chemical can trigger a sudden reflex in the body.

Table VA.1: Comparison Table for the devices performing nociception behavior.

No.	Active material	2- or 3-terminal (Electrical/ Optical)	Nociception is performed using signals of			Ref.	Applications performed
			One type	Two types			
				External sensors integrated	Dual input devices		
1	ZrO_x	2 (E)	✓	-	-	[3]	Leaky integrate and fire
2	HfO_x	2 (E)	✓	-	-	[4]	-
3	ITO	3 (E)	✓	-	-	[8]	-
4	$MAPbBr_3$	2 (E)	✓	-	-	[9]	-
5	MoS_2	2 (E)	✓	-	-	[10]	-
6	TaO_x	3 (E)	✓	-	-	[11]	-
7	Sodium alginate	3 (E)	✓	-	-	[12]	-
8	Ni-ZNO	2 (E)	✓	-	-	[13]	-
9	$MoSe_2$	2 (E)	✓	-	-	[14]	-
10	$MAPbI_3$	2 (E)	✓	-	-	[15]	-
11	TiO_2 nanobelt	2 (E)	✓	-	-	[5]	-
12	SiO_x:Ag	2 (E)	✓	-	-	[6]	-
13	TiO_2	2 (E)	✓	-	-	[7]	-
14	$MAPbI_3$:Ag	2 (E)	✓	✓	-	[31]	-
15	ATO	2 (O)	✓	-	-	[16]	-
16	ITO	3 (O)	✓	-	-	[17]	-
17	PMMA: Azo-Au NPs	2 (O)	✓	-	-	[18]	-
18	SONP	3 (O)	✓	-	-	[19]	Classical conditioning
19	C8-BTBT	2 (O)	✓	-	-	[20]	-
20	ZnO/NiO	2 (O)	✓	-	-	[21]	-
21	PDVT-10	3 (E)	-	✓	-	[22]	-
22	Bi_2Se_3	2 (E)	-	✓	-	[23]	-

23	Xanthan gum	3 (E)	-	✓		[24]	-
24	FK-800	2 (E)	✓	✓	-	[25]	-
25	NbO_x	2 (E)	-	✓	-	[26]	-
26	PDVT-10	3 (E)	✓	✓	-	[27]	-
27	Chitosan	3 (E)	-	✓	-	[28]	-
28	h-BN	2 (E)	✓	✓	-	[29]	-
29	VO_2	2 (E)	-	✓		[30]	-
30	PQT-12/PEO	3 (E)	-	-	✓	[32]	-
31	S-CNT	3 (E)	-	-	✓	[33]	Classical Conditioning, Self- healing
32	**Ag**	**2** (E)	✓		✓	**This Work**	**Classical Conditioning, Self-healing, Adaptation, Nociception behavior, Antinociception behavior**

VA.5 Conclusions

In summary, this study introduces a novel biomimetic neuromorphic device serving as a mechanosensor in the low strain range, while exhibiting excellent neuromorphic functionalities at the higher strain. The stretchable self-healing device involving a hierarchical Ag microwire network was formed on a PDMS substrate by a self-formed crack templating method facilitating cost-effectiveness, fabrication ease, and scalability. In the neuromorphic domain, brain-inspired functionalities such as conductance switching, STP, LTP, and so on could be emulated successfully. The mechanism relies on the formation of Ag filaments between the nano-gaps due to electromigration under appropriate electrical conditions. The potentiated device showed a six-order high sensitivity compared to the pristine device, establishing a positive synergy between the sensing and the potentiated domain for attaining ultra-high sensitivity. The enhancement could be attributed to the participation of nano-filaments in the sensitivity. A further

study on strain-dependent plasticity adaptation shows a new pathway for controlling the operating electrical range, that could be exploited in self-adaptive devices in intelligent systems. Such exclusive properties were explored in mimicking various first and second-order cognitive learnings namely classical conditioning, nociception, and antinociception. The device showed habituated behavior when underwent repetitive strain stimulus by restoring the LRS conductance despite being under strain, exemplifying the first empirical demonstration of antinociception in a bio-inspired artificial system. The versatility demonstrated in this work not only establishes the device as a fundamental building block for advanced brain-inspired technologies but also paves the way for the development of intelligent systems capable of emulating complex cognitive functions.

References

[1] Nikolenko V N, Shelomentseva E M, Tsvetkova M M, Abdeeva E I, Giller D B, Babayeva J V., Achkasov E E, Gavryushova L V. and Sinelnikov M Y 2022 Nociceptors: Their Role in Body's Defenses, Tissue Specific Variations and Anatomical Update *J. Pain Res.* **15** 867–77

[2] Zhu J, Zhang T, Yang Y and Huang R 2020 A comprehensive review on emerging artificial neuromorphic devices *Appl. Phys. Rev.* **7** 011312

[3] Yang J H, Mao S C, Chen K T and Chen J S 2023 Emulating Nociceptive Receptor and LIF Neuron Behavior via ZrO_x-based Threshold Switching Memristor *Adv. Electron. Mater.* **9** 2201006

[4] Kim Y, Kwon Y J, Kwon D E, Yoon K J, Yoon J H, Yoo S, Kim H J, Park T H, Han J W, Kim K M and Hwang C S 2018 Nociceptive Memristor *Adv. Mater.* **30** 1–7

[5] Xiao M, Shen D, Futscher M H, Ehrler B, Musselman K P, Duley W W and Zhou Y N 2020 Threshold Switching in Single Metal-Oxide Nanobelt Devices Emulating an Artificial Nociceptor *Adv. Electron. Mater.* **6** 1–12

[6] Yoon J H, Wang Z, Kim K M, Wu H, Ravichandran V, Xia Q, Hwang C S and Yang J J 2018 An artificial nociceptor based on a diffusive memristor *Nat. Commun.* **9** 1–9

[7] Sahu M C, Jena A K, Mallik S K, Roy S, Sahoo S, Ajimsha R S, Misra P and Sahoo S 2023 Reconfigurable Low-Power TiO_2 Memristor for Integration of Artificial Synapse and Nociceptor *ACS Appl. Mater. Interfaces* **15** 25713–25

[8] Feng G, Jiang J, Zhao Y, Wang S, Liu B, Yin K, Niu D, Li X, Chen Y, Duan H, Yang J, He J, Gao Y and Wan Q 2020 A Sub-10 nm Vertical Organic/Inorganic Hybrid Transistor for Pain-Perceptual and Sensitization-Regulated Nociceptor Emulation *Adv. Mater.* **32** 1–11

[9] John R A, Yantara N, Ng S E, Patdillah M I Bin, Kulkarni M R, Jamaludin N F, Basu J, Ankit, Mhaisalkar S G, Basu A and Mathews N 2021 Diffusive and Drift Halide Perovskite Memristive Barristors as Nociceptive and Synaptic Emulators for Neuromorphic Computing *Adv. Mater.* **33** 1–13

[10] Dev D, Shawkat M S, Krishnaprasad A, Jung Y and Roy T 2020 Artificial Nociceptor Using 2D MoS_2Threshold Switching Memristor *IEEE Electron Device Lett.* **41** 1440–3

[11] Chen K T, Shih L C, Mao S C and Chen J S 2023 Mimicking Pain-Perceptual Sensitization and Pattern Recognition Based on Capacitance- and Conductance-Regulated Neuroplasticity in Neural Network *ACS Appl. Mater. Interfaces* **15** 9593–9603

[12] Li Y, Yin K, Diao Y, Fang M, Yang J, Zhang J, Cao H, Liu X and Jiang J 2022 A biopolymer-gated ionotronic junctionless oxide transistor array for spatiotemporal pain-perception emulation in nociceptor network *Nanoscale* **14** 2316–26

[13] Khan R, Rehman N U, Ilyas N, Sfina N, Barhoumi M, Khan A, Althubeiti K, Otaibi S Al, Iqbal S, Rahman N, Sohail M, Ullah A, Del Rosso T, Zaman Q, Ali Khan A, Abdullaev S S and Khan A 2022 Threshold switching in nickel-doped zinc oxide based memristor for artificial sensory applications *Nanoscale* **15** 1900–13

[14] Duan H, Wang D, Gou J, Guo F, Jie W and Hao J 2023 Memristors based on 2D $MoSe_2$ nanosheets as artificial synapses and nociceptors for neuromorphic computing *Nanoscale* **15** 10089–96

[15] Patil H, Kim H, Kadam K D, Rehman S, Patil S A, Aziz J, Dongale T D, Ali Sheikh Z, Khalid Rahmani M, Khan M F and Kim D K 2023 Flexible Organic-Inorganic Halide Perovskite-Based Diffusive Memristor for Artificial Nociceptors *ACS Appl. Mater. Interfaces* **15** 13238–48

[16] Kumar M, Kim H S and Kim J 2019 A Highly Transparent Artificial Photonic Nociceptor *Adv. Mater.* **31** 1–9

[17] Feng G, Jiang J, Li Y, Xie D, Tian B and Wan Q 2021 Flexible Vertical Photogating Transistor Network with an Ultrashort Channel for In-Sensor Visual Nociceptor *Adv. Funct. Mater.* **31** 1–12

[18] Zhou L, Zhang S R, Yang J Q, Mao J Y, Ren Y, Shan H, Xu Z, Zhou Y and Han S T 2020 A UV damage-sensing nociceptive device for bionic applications *Nanoscale* **12** 1484–94

[19] Wei H, Ni Y, Sun L, Yu H, Gong J, Du Y, Ma M, Han H and Xu W 2021 Flexible electro-optical neuromorphic transistors with tunable synaptic plasticity and nociceptive behavior *Nano Energy* **81** 105648

[20] Shi X, Liu W, Xu Y, Jin C, Zhang G, Shi Y, Huang H, Sun J and Yang J 2023 Ultraviolet-selective organic phototransistors for low-power skin-inspired nociceptor *Nano Energy* **110** 108372

[21] Bhatnagar P, Nguyen T T, Kim S, Seo J H, Patel M and Kim J 2021 Transparent photovoltaic memory for neuromorphic device *Nanoscale* **13** 5243–50

[22] Wu X, Li E, Liu Y, Lin W, Yu R, Chen G, Hu Y, Chen H and Guo T 2021 Artificial multisensory integration nervous system with haptic and iconic perception behaviors *Nano Energy* **85** 106000

[23] Shi Y, Hua Q, Dong Z, Wang B, Dai X, Niu J, Cui Z, Huang T, Wang Z L and Hu W 2023 Neuro-inspired thermoresponsive nociceptor for intelligent sensory systems *Nano Energy* **113** 108549

[24] Li F Z, Liu H R, Guo J M, Zhou X Y, Liu K K, Liang L Z, Pei X Y, Zhou F C, Huang F, Wang H and Liu Y H 2022 An Artificial Thermal Nociceptor Based on Xanthan Gum-Gated Synaptic Transistors to Emulate Human Thermal Nociception *Adv. Intell. Syst.* **4** 1–8

[25] Xu X, Cho E J, Bekker L, Talin A A, Lee E, Pascall A J, Worsley M A, Zhou J, Cook C C, Kuntz J D, Cho S and Orme C A 2022 A Bioinspired Artificial Injury Response System Based on a Robust Polymer Memristor to Mimic a Sense of Pain, Sign of Injury, and

Healing *Adv. Sci.* **9** 1–11

[26] Zhu J, Zhang X, Wang M, Wang R, Chen P, Cheng L and Liu Q 2022 An Artificial Spiking Nociceptor Integrating Pressure Sensors and Memristors *IEEE Electron Device Lett.* **43** 962–5

[27] Yu R, Yan Y, Li E, Wu X, Zhang X, Chen J, Hu Y, Chen H and Guo T 2021 Bi-mode electrolyte-gated synaptic transistor via additional ion doping and its application to artificial nociceptors *Mater. Horizons* **8** 2797–807

[28] Yu F, Yu F, Yu F, Cai J C, Cai J C, Cai J C, Zhu L Q, Zhu L Q, Sheikhi M, Sheikhi M, Zeng Y H, Zeng Y H, Guo W, Guo W, Ren Z Y, Ren Z Y, Xiao H, Xiao H, Ye J C, Ye J C, Lin C H, Wong A B and Wu T 2020 Artificial Tactile Perceptual Neuron with Nociceptive and Pressure Decoding Abilities *ACS Appl. Mater. Interfaces* **12** 26258–66

[29] Ding G, Chen R S, Xie P, Yang B, Shang G, Liu Y, Gao L, Mo W A, Zhou K, Han S T and Zhou Y 2022 Filament Engineering of Two-Dimensional h-BN for a Self-Power Mechano-Nociceptor System *Small* **18** 1–15

[30] Xia Q, Qin Y, Qiu P, Zheng A and Zhang X 2022 A bio-inspired tactile nociceptor constructed by integrating wearable sensing paper and a VO_2 threshold switching memristor *J. Mater. Chem. B* **10** 1991–2000

[31] Im I H, Baek J H, Kim S J, Kim J, Park S H, Kim J Y, Yang J J and Jang H W 2023 Halide Perovskites-based Diffusive Memristors for Artificial Mechano-Nociceptive System *Adv. Mater.* **2307334** 1–13

[32] Xu Y, Liu D, Dai S, Zhang J, Guo Z, Liu X, Xiong L and Huang J 2024 Stretchable and neuromorphic transistors for pain perception and sensitization emulation *Mater. Horiz.* **11** 958–68

[33] Wang Y, Liu D, Zhang Y, Fan L, Ren Q, Ma S and Zhang M 2022 Stretchable Temperature-Responsive Multimodal Neuromorphic Electronic Skin with Spontaneous Synaptic Plasticity Recovery *ACS Nano* **16** 8283–8293

[34] Yan X, Qian J H, Sangwan V K and Hersam M C 2022 Progress and Challenges for Memtransistors in Neuromorphic Circuits and Systems *Adv. Mater.* **34** 1–18

[35] Xia Q and Yang J J 2019 Memristive crossbar arrays for brain-inspired computing

Nat. Mater. **18** 309–23

[36] Kim M K, Park Y, Kim I J and Lee J S 2020 Emerging Materials for Neuromorphic Devices and Systems *iScience* **23** 101846

[37] Banerjee W 2020 Challenges and applications of emerging nonvolatile memory devices *Electron.* **9** 1–24

[38] Bannur B, Yadav B and Kulkarni G U 2022 Second-Order Conditioning Emulated in an Artificial Synaptic Network *ACS Appl. Electron. Mater.* **4** 1552–7

[39] Yadav B, Mondal I, Bannur B and Kulkarni G U 2023 Emulating learning behavior in a flexible device with self-formed Ag dewetted nanostructure as active element. *Nanotechnology* **35** 015205

[40] Bannur B and Kulkarni G U 2020 On synapse intelligence emulated in a self-formed artificial synaptic network *Mater. Horizons* **7** 2970–7

[41] Rao T S, Mondal I, Bannur B and Kulkarni G U 2023 A scalable solution recipe for a Ag-based neuromorphic device *Discov. Nano* **18** 124

[42] Attri R, Mondal I, Yadav B, Kulkarni G U and Rao C N R 2024 Neuromorphic devices realised using self-forming hierarchical Al and Ag nanostructures: towards energy-efficient and wide ranging synaptic plasticity *Mater. Horiz.* **11** 737–46

[43] Harris J A 1996 Descending antinociceptive mechanisms in the brainstem: Their role in the animal's defensive system *J. Physiol. Paris* **90** 15–25

[44] Butler R K and Finn D P 2009 Stress-induced analgesia. *Prog. Neurobiol.* **88** 184–202

[45] Jhaveri M D, Sagar D R, Elmes S J R, Kendall D A and Chapman V 2007 Cannabinoid CB_2 receptor-mediated anti-nociception in models of acute and chronic pain *Mol. Neurobiol.* **36** 26–35

[46] Wan Q, Wan C, Wu H, Yang Y, Huang X, Zhou P, Chen L, Wang T Y, Li Y, Xue K H, He Y H, Miao X S, Li X, Xie C, Chen H, Song Z, Wang H, Hao Y, Zhang J, Huang J, Ren Z Y, Zhu L Q, Du J, Ge C, Liu Y, Ding G, Zhou Y, Han S T, Wang G, Yu X, Chen B, Chu Z, Wang L, Xia Y, Mu C, Lin F, Chen C, Cheng B, Xing Y, Zeng W, Chen H, Yu L, Indiveri G and Qiao N 2022 2022 roadmap on neuromorphic devices and applications

research in China *Neuromorphic Comput. Eng.* **2** 042501

[47] Kiruthika S, Gupta R, Rao K D M, Chakraborty S, Padmavathy N and Kulkarni G U 2014 Large area solution processed transparent conducting electrode based on highly interconnected Cu wire network *J. Mater. Chem. C* **2** 2089–94

[48] Govind R K, Mondal I, Baishya K, Ganesha M K, Walia S, Singh A K and Kulkarni G U 2022 Large-Area Fabrication of High Performing, Flexible, Transparent Conducting Electrodes Using Screen Printing and Spray Coating Techniques *Adv. Mater. Technol.* **7** 2101120

[49] Li P, Zhao Y, Ma J, Yang Y, Xu H and Liu Y 2020 Facile Fabrication of Ultraflexible Transparent Electrodes Using Embedded Copper Networks for Wearable Pressure Sensors *Adv. Mater. Technol.* **5** 1900823

[50] Gupta N, Rao K D M, Srivastava K, Gupta R, Kumar A, Marconnet A, Fisher T S and Kulkarni G U 2018 Cosmetically Adaptable Transparent Strain Sensor for Sensitively Delineating Patterns in Small Movements of Vital Human Organs *ACS Appl. Mater. Interfaces* **10** 44126–33

[51] Mondal I and Kulkarni G U 2022 Lithography-Free Fabrication of Periodic Metal Network for Ultra-Sensitive Transparent and Unidirectional Strain Sensor in Health-Monitoring Applications *Adv. Mater. Interfaces* **9** 1–9

[52] Tennico Y H, Koesdjojo M T, Kondo S, Mandrell D T and Remcho V T 2010 Surface modification-assisted bonding of polymer-based microfluidic devices *Sensors Actuators, B Chem.* **143** 799–804

[53] Nag A, Simorangkir R B V B, Valentin E, Björninen T, Ukkonen L, Hashmi R M and Mukhopadhyay S C 2018 A Transparent Strain Sensor Based on PDMS-Embedded Conductive Fabric for Wearable Sensing Applications *IEEE Access* **6** 71020–7

[54] Masuda H and Kizuka T 2014 Distance control of electromigration-induced silver nanogaps. *J. Nanosci. Nanotechnol.* **14** 2436–40

[55] Sánchez-Romate X X F and Prolongo A J S and S G 2016 Smart Coatings with Carbon Nanoparticles *Intech* vol 11 p 13

[56] Nie B, Li X, Shao J, Li X, Tian H, Wang D, Zhang Q and Lu B 2017 Flexible and

Transparent Strain Sensors with Embedded Multiwalled Carbon Nanotubes Meshes. *ACS Appl. Mater. Interfaces* **9** 40681–9

[57] Preston D J, Jiang H J, Sanchez V, Rothemund P, Rawson J, Nemitz M P, Lee W-K, Suo Z, Walsh C J and Whitesides G M 2019 A Soft Ring Oscillator *Sci. Robot.* **4** 1–9

[58] Li A, Ma L, Keene D, Klingel J, Payne M and Wang X 2016 Forced oscillations with linear and nonlinear damping *Am. J. Phys.* **84** 32–7

[59] Peek F W 1920 *Dielectric phenomena in high voltage engineering* (New York, London)

[60] Germer L H 1959 Electrical Breakdown between Close Electrodes in Air *J. Appl. Phys.* **30** 46–51

[61] Qu J, Zeng M, Zhang D, Yang D, Wu X, Ren Q and Zhang J 2021 A review on recent advances and challenges of ionic wind produced by corona discharges with practical applications *J. Phys. D. Appl. Phys.* **55** 153002

[62] Mohanty S, Bhushan B, Das A K and Dixit A R 2019 Production of hard and lubricating surfaces on miniature components through micro-EDM process *Int. J. Adv. Manuf. Technol.* **105** 1983–2000

[63] Islamov R S and Krishtafovich Y A 2013 Lifetime and erosion of silver-based wire electrodes in an ultracorona in air *J. Electrostat.* **71** 109–15

[64] G.A. Mesyats 1997 Ectons and their Role in Electrical Discharges in Vacuum and Gases **07** C4-93-C4-112

[65] Zhang H, Zeng H, Priimagi A and Ikkala O 2020 Viewpoint: Pavlovian Materials—Functional Biomimetics Inspired by Classical Conditioning *Adv. Mater.* **32** 1906619

[66] Yan W, Fuh H R, Lv Y, Chen K Q, Tsai T Y, Wu Y R, Shieh T H, Hung K M, Li J, Zhang D, Ó Coileáin C, Arora S K, Wang Z, Jiang Z, Chang C R and Wu H C 2021 Giant gauge factor of Van der Waals material based strain sensors *Nat. Commun.* **12** 6–14

[67] Liu Z, Qi D, Guo P, Liu Y, Zhu B, Yang H, Liu Y, Li B, Zhang C, Yu J, Liedberg B and Chen X 2015 Thickness-Gradient Films for High Gauge Factor Stretchable Strain Sensors *Adv. Mater.* **27** 6230–7

[68] Kumaresan Y, Mishra S, Ozioko O, Chirila R and Dahiya R 2022 Ultra-High Gauge Factor Strain Sensor with Wide-Range Stretchability *Adv. Intell. Syst.* **4** 1–9

Chapter VB

Designing a Tactile Neuromorphic Device using Strain as Input Stimulus

Summary

This study explores the development of a two-terminal strain-sensitive neuromorphic device that mimics human tactile sensory functions. The device features a network of gold microwires partially embedded in a PDMS matrix, designed to respond to mechanical stimuli. It demonstrates various neuromorphic functionalities such as short-term plasticity (STP), long-term plasticity (LTP), spike-rate-dependent plasticity (SRDP), spike-amplitude-dependent plasticity (SADP), and paired-pulse facilitation (PPF) with a response closely resembling biological systems. The study addresses the challenges of integrating sensing and memory units without complex electronic interfaces, offering potential advancements in neuroprosthetics and other applications.

VB.1 Introduction

The human brain, renowned as the most complex structure in the known universe, accomplishes a multitude of tasks with a seamless blending of processing and memory units, leading to an efficiency akin to conducting an exaflop (10^{18}) of mathematical operations per second while consuming a mere 20 watts of power[1]. Motivated by the versatility of the human brain, a variety of artificial neuromorphic devices have been reported to create bio-inspired architectures[2]. Also, the human cognition system encompasses a variety of sensory functions, including tactile[3], visual[4], auditory[5], gustatory[6], and olfactory[7] perception, which allows individuals to identify and understand various stimuli. Inspired by biological sensing mechanisms, efforts have been made to create neuromorphic devices capable of simultaneously sensing, storing, and processing information efficiently[8–10]. Among the array of sensing systems available, biomimetic tactile sensors, also known as mechanoreceptors, stand out. These sensors gather information such as pressure, texture, vibration, temperature, and even pain through direct contact with surrounding objects. These physical stimuli are converted into electrical signals that are then relayed among neurons through synapses, ultimately reaching the central nervous system for interpretation[11]. Their potential applications

in robotics, prosthetics, and wearable devices have garnered significant interest. Numerous studies have explored ways to replicate biological tactile sensing. One way is to integrate a tactile sensor with external memory and computing units by a sophisticated interface electronic circuit. For instance, Jiang *et al*. illustrated a tactile sensory nerve through the fusion of a tactile sensor with an ion-gel gated transistor functioning as a synaptic device connected via a spike coding circuit[12]. Also, Wang *et al*. have integrated a polyurethane sponge sensor with a chitosan-based memristor, allowing information to be sensed, memorized, and processed[13]. The other way is to make one sandwiched geometry encompassing the sensing unit and memory unit without the need for interface electronics. For example, Wang *et al*. showcased a pressure-sensitive device that integrates a tactile sensor with a flexible hafnium oxide memristor array, enabling simultaneous sensing and computation[14], and Jiang *et al*. have demonstrated a combined tactile sensing device based on piezo-OLED array and piezo memristor array[15].

However, these artificial tactile sensing structures entail complex electronic interfaces for data conversion and transmission between the sensor and synaptic device, leading to increased latency and energy consumption[16]. Also, the integrated sensor and memristor design encounter challenges related to accuracy, scalability, precision, and limited computational power[15]. These challenges are exacerbated in large-scale multifunctional systems. As a result, there is a significant requirement for a system with dual functionality that can both sense mechanical stimuli and exhibit neuromorphic behavior simultaneously, making it the focal point of interest in this article.

In this study, a two-terminal strain-sensitive neuromorphic device, which consists of a highly interconnected network of Au microwires serving as the active element, partially embedded in a PDMS matrix is reported. Here, the strain applied to the device serves as a direct input stimulus to realize various neuromorphic functionalities, including the STP, LTP, SRDP, SADP, and the PPF index, which is obtained very close to the biological systems (232%). Such insights will drive the development of technologies capable of emulating human sensory functions, thereby propelling the evolution of next-generation neuroprosthetics systems.

VB.2 Scope of the present investigation

The investigation focuses on creating a neuromorphic device capable of both sensing mechanical stimuli and exhibiting neuromorphic behavior simultaneously. It involves the design and fabrication of a two-terminal strain-sensitive system using gold microwires and a PDMS matrix. The study aims to characterize the device's response to different types of stimuli and evaluate its neuromorphic functionalities. Additionally, the research explores the potential applications of this technology in next-generation neuroprosthetics systems and other areas requiring biomimetic sensory functions.

VB.3 Experimental methods

Device fabrication procedure

(i) Formation of crackle template

A commercially available acrylic resin was diluted with a 15:85% volume of water: IPA to make a concentration of 1 g/ml. The mixture was rigorously ultrasonicated for 30 minutes and subsequently spin-coated at 1000 rpm for 100 seconds on a Si(100) n-type substrate having an area of 1.5×1.5 cm^2. After drying, the coated layer developed cracks of approximately 2 μm, forming a sacrificial crackle template for metal deposition (Figure VB.1a).

(ii) Electroless deposition of Au

Solutions of 17 mg of chloroauric acid ($HAuCl_4$) in 2 ml of water and 1.1 ml of hydrofluoric acid (HF) in 1.9 ml of water were prepared and mixed together to form an Au electroless solution having a concentration of 10 mM. The crackle template developed on the Si substrate was dipped in the Au electroless solution for 2 minutes, causing the deposition of Au in the interconnected crack regions. Then, the sacrificial layer of crackle precursor was removed by gently washing with chloroform, and a highly interconnected Au network on the Si substrate was obtained (Figure VB.1a). The measured thickness of the Au network was 65 nm.

(iii) Transferring the Au network to PDMS

Commercially available (Dowsil) precursors to PDMS, i.e., vinyl-terminated siloxane prepolymer (base material) and siloxane cross-linking agent (curing agent), were mixed in 1:10 mixing ratios (curing agent: base material). The mixture was stirred well and degaussed by placing it in a vacuum desiccator for 30 min to remove bubbles. The degaussed mixture was poured on the master pattern, which is the Au network on the Si

substrate, and cured at 80°C for 1 hour. After curing, the PDMS layer was peeled off, and the Au network semi-embedded in the PDMS was obtained (Figure VB.1a). The device fabrication was finalized by deploying Cu wires as contacts on the Au-embedded PDMS using Ag epoxy, which was dried for 30 minutes at 80°C on the hot plate.

Device characterization

Highly magnified optical microscopy images of a desiccated crack template and Au wire network embedded within PDMS were taken by the Keyence VHX 7000 system. UV-Vis-NIR spectroscopy, conducted with the CARY SERIES instrument from Agilent, assessed the transmittance of the device. Electrical characteristics were evaluated with a source measurement unit (SMU) Keithley 2450 under ambient conditions, with the device mounted on a programmable stage featuring automated translational movement for strain application, run using a Python routine.

VB.4 Results and discussion

Resistive strain sensors, utilizing the elastic properties of polydimethylsiloxane (PDMS), are widely acknowledged for their ability to bend and stretch. These sensors demonstrate a change in electrical properties in response to mechanical deformations[17]. In this study, a strain-based neuromorphic device composed of a highly interconnected Au network semi-embedded in PDMS, with the fabrication strategy inspired by previous work from the laboratory illustrated in Figure VB.1a[18]. Briefly, the fabrication of the device included crackle lithography, which produced a sacrificial crackle template for the electroless Au deposition in the microcracks. Following the Au deposition, the sacrificial template was lifted off, resulting in an interconnected Au network on the Si substrate, which acted as the master pattern for PDMS. PDMS solution with the desired ratio of curing agent to base was poured onto this master pattern, cured, and peeled off. After peeling off, the Au network came off with the PDMS, resulting in a highly interconnected Au network semi-embedded in PDMS (Figure VB.1b-c). To complete the design and enable communication with external electrical appliances, two Cu wires were affixed with Ag epoxy at the device edges to serve as electrodes (details in the experimental section). The microscale size of the Au network contributes to a remarkable transparency of ~70% for these devices (Figure VB.1d). The inset of Figure VB.1d provides a digital image of the device mounted on a strain sensor apparatus. Unlike conventional strain-responsive neuromorphic devices that convert mechanical stimuli (like strain, pressure, etc.) to

electrical signals before processing[19], shown as path 1(green) in Figure VB.1e, the present device utilizes strain as a direct stimulus (Path 2, blue) to the neuromorphic device.

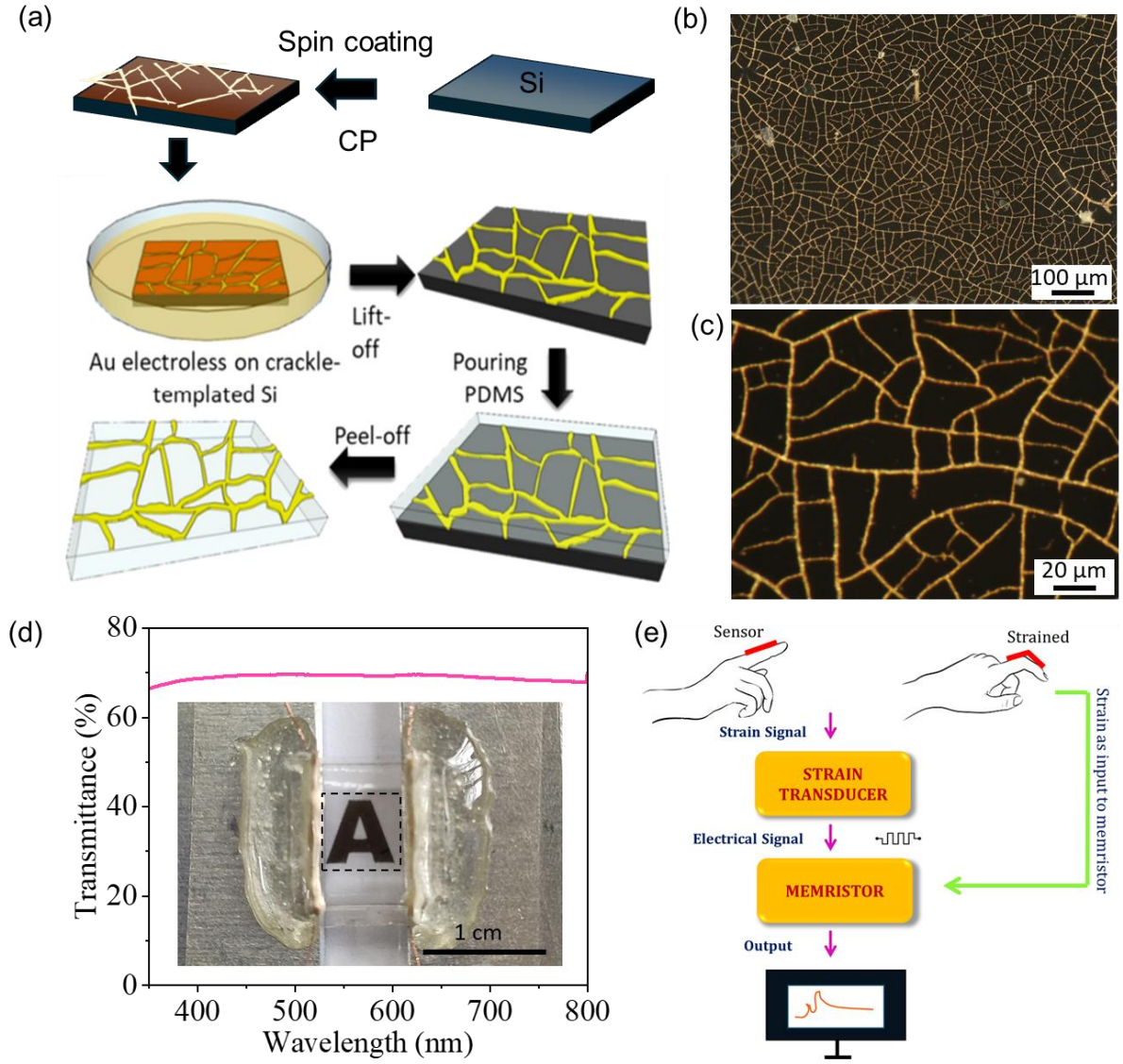

Figure VB.1. (a) Schematic illustrating the fabrication process of Au wire network embedded in PDMS substrate. (b) Optical microscopy image (reflection mode) of highly interconnected Au wire network embedded in PDMS substrate. (c) Magnified view of the network with wire thickness ranging between 1 - 2 µm. (d) The transmittance spectrum in the visible range illustrates ~70% transmission through the device. Inset shows the image of the device with the letter 'A' below. (e) Schematic illustrating how strain is employed directly as input to the device. Path 2 (Purple) operates without any additional circuitry to convert strain into an electrical pulse (Path 1, Green) before feeding into the device.

The application of strain results in the change in resistance (ΔR), regarded as the output from the device. Hence, this device works with strain as input and opens up new avenues for the paradigm of neuromorphic devices, represented by a schematic in Figure VB.1e.

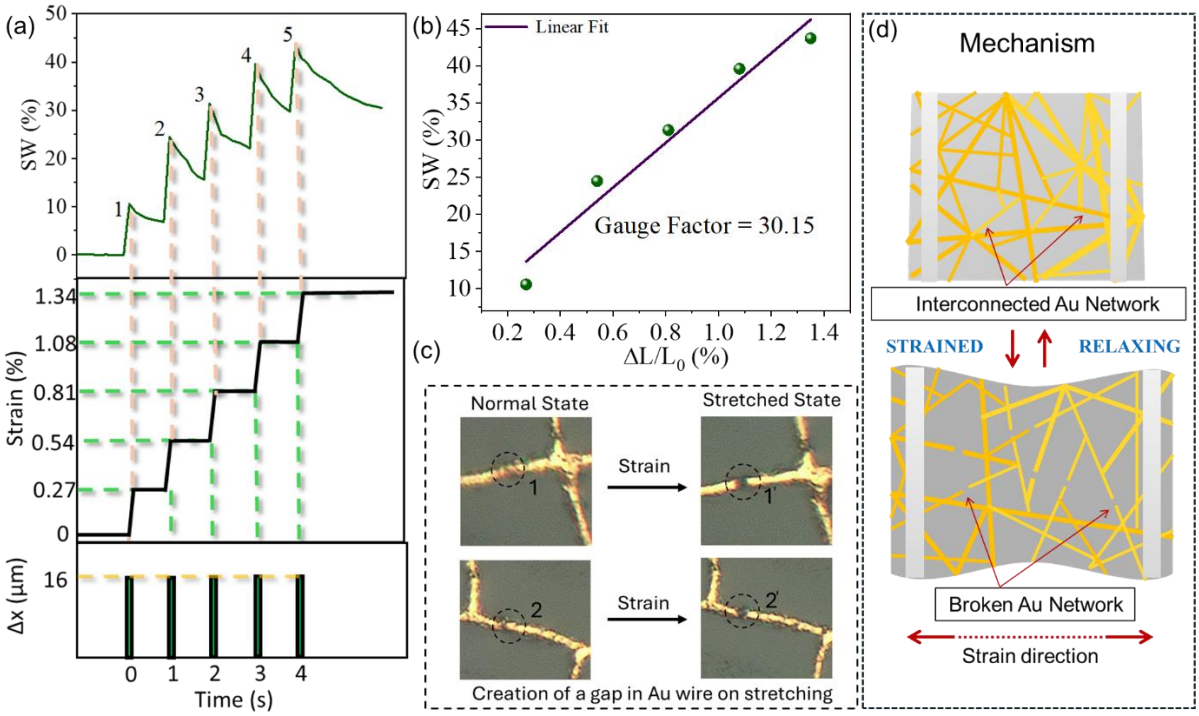

Figure VB.2: (a) Plot representing the variation in synaptic weight (SW, ΔR/R0) of the device when the strain sensor apparatus is subjected to displacement pulses with a pulse interval of 1 s, amplitude (Δx) of 16 μm, and a pulse width of ~0.5 s (strain (ε): 0.27%). (b) SW shows a linear variation with applied strain for device D1 (Δt of 1 s, Δx of 16 μm and ε is 0.27%). The gauge factor derived from the slope stands at 30.15. (c) Optical microscopy images of the device in normal and stretched states showing nano/micro gap formation in the Au wires on applying the strain. (dashed circles 1,2 in the normal state and 1́,2 in the stretched state). (d) Schematic depicting the mechanism of the device upon application of strain.

The fabricated device was mounted on a stage with automated translational movement programmed using Python. The displacement (Δx) provided in the x-direction causes the application of strain on the device. The displacement-induced strain was calculated using the formula provided below.

$$\text{Strain (\%)} = \varepsilon\ (\%) = \Delta x/x \times 100, \qquad (1)$$

Where Δx is the change in distance, and x is the initial distance between the electrodes42. The displacement of 16 μm generated a strain of ~ 0.27% in the device, calculated using equation 1. The device was subjected to five successive displacement pulses of 16 μm with 1s intervals, resulting in the enhancement of strain with each pulse applied to the device. The applied strain causes a significant change in the resistance of the device, which is defined as

$$\text{Synaptic weight (SW)} = \Delta R/R_0\ , \qquad (2)$$

where ΔR is the change in the resistance due to the application of strain and R0 is the initial resistance of the device. The resistance was constantly monitored at a bias voltage using a source meter. The peaks 1, 2, 3, 4, and 5 in Figure VB.2a represent the change in SW after each displacement pulse. This SW plotted against the strain shows a linear variation with a gauge factor of 30.15, which favors the intended application (Figure VB.2b). The gauge factor was calculated using the following equation,

$$\text{Gauge Factor (GF)} = \Delta R/(R_0 \times \varepsilon) \quad (3)$$

where ε is the input strain calculated using eqn.1[20]. Optical microscopy was employed to compare the device in both its normal and stretched states. The morphological transformation of the Au wire under strain is distinctly observable at designated locations marked as 1 and 2 in the normal state and 1̓ and 2̓ in the stretched state (see dashed circles in Figure VB.2c. In the normal state, Au wires form an interconnected network connecting the electrodes that establish a path for the current flow between the electrodes, resulting in a pristine device attaining a low-resistance state. However, upon application of displacement pulse, the Au wires undergo stretching, forming nm- to μm-sized gaps, depending on the amplitude of the pulse. This leads to a sudden and sharp increase in device resistance. After the removal of the pulse, the device returns to a low-resistance state gradually by bridging the gaps formed, facilitated by the flexible PDMS support as illustrated schematically in Figure VB.2d. Before complete relaxation, the application of another pulse further elevates the resistance state. Notably, this increase was more pronounced as the device was not relaxed due to the small time interval between pulses. To study the observed behavior in detail, the device was subjected to pulses with varying time intervals. The inspiration for device functionality comes from biological synapses, where transmission of synaptic signals between two neurons involves the release and transfer of neurotransmitters from the presynaptic neuron to the postsynaptic neuron triggered by the action potential (Figure VB.3a). The release of neurotransmitters induces a change in synaptic weight, which contributes to the formation and the modulation of memory[21]. The change in resistance (ΔR) generated by the input displacement pulse of the device emulates the modification of synaptic weight by the action potential. Therefore, the response (ΔR) of the device to displacement pulse application can be considered analogous to the functioning of the biological synapses (Figure VB.3b). Paired Pulsed Facilitation (PPF) is a crucial synaptic function

that occurs when a presynaptic neuron receives rapid successive stimuli. In such cases, the postsynaptic output gets amplified for the later stimulus, demonstrating the temporal correlation between the neuronal circuits[22].

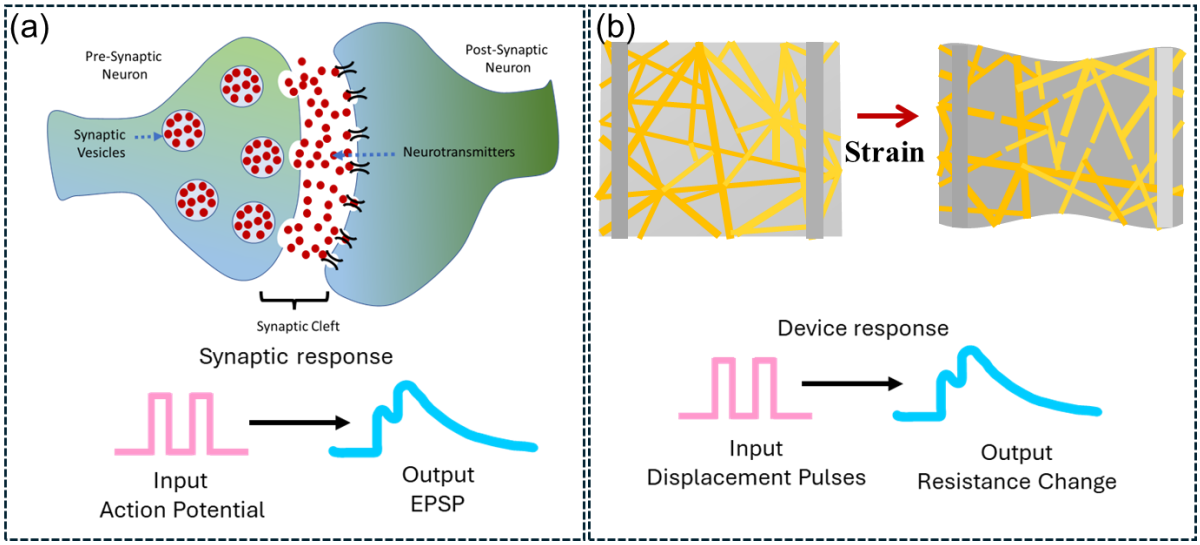

Figure VB.3: (a) Schematic illustrating the signal transmission between pre- and post-synaptic neurons in a biological synapse through the release of neurotransmitters. The pre- and post-synaptic responses in biological neurons are analogous to the displacement pulse as input, causing a change in resistance as output, respectively. (b) The resistance change arises due to the application of strain on the device.

Figure VB.4a illustrates the variation of SW by applying five successive displacement pulses at different time intervals (Δt, 1 to 5 s). At shorter time intervals, a significant enhancement in resistance was observed. This is attributed to insufficient time for the device to relax before the subsequent pulse, showcasing an observable PPF effect. Conversely, with longer time intervals, the device has more time to relax to a lower resistance value facilitated by the underlying flexible PDMS matrix. Consequently, the PPF behavior is suppressed due to this extended relaxation period. The peak value of SW of all five peaks were extracted from Figure VB.4a at each time interval and plotted against time in Figure VB.4b, which follows a linear trend. The SW was higher at lower intervals and decreased with increments in time intervals demonstrating time interval or Spike rate-dependent plasticity (SRDP) in the device. To examine the impact of displacement pulse amplitude on this phenomenon, experiments at other amplitudes were carried out, specifically 22 μm (ε, 0.37%) and 25 μm (ε, 0.42%) applied to the device. Figure VB.4c illustrates the variation of slopes derived from the peak value of SW over time for all three amplitudes. Notably, all slopes tend to decrease as Δt increases. Furthermore, there is an

observable increasing trend in slopes at higher amplitude values, suggesting an enhanced impact of pulse amplitude on the studied behavior.

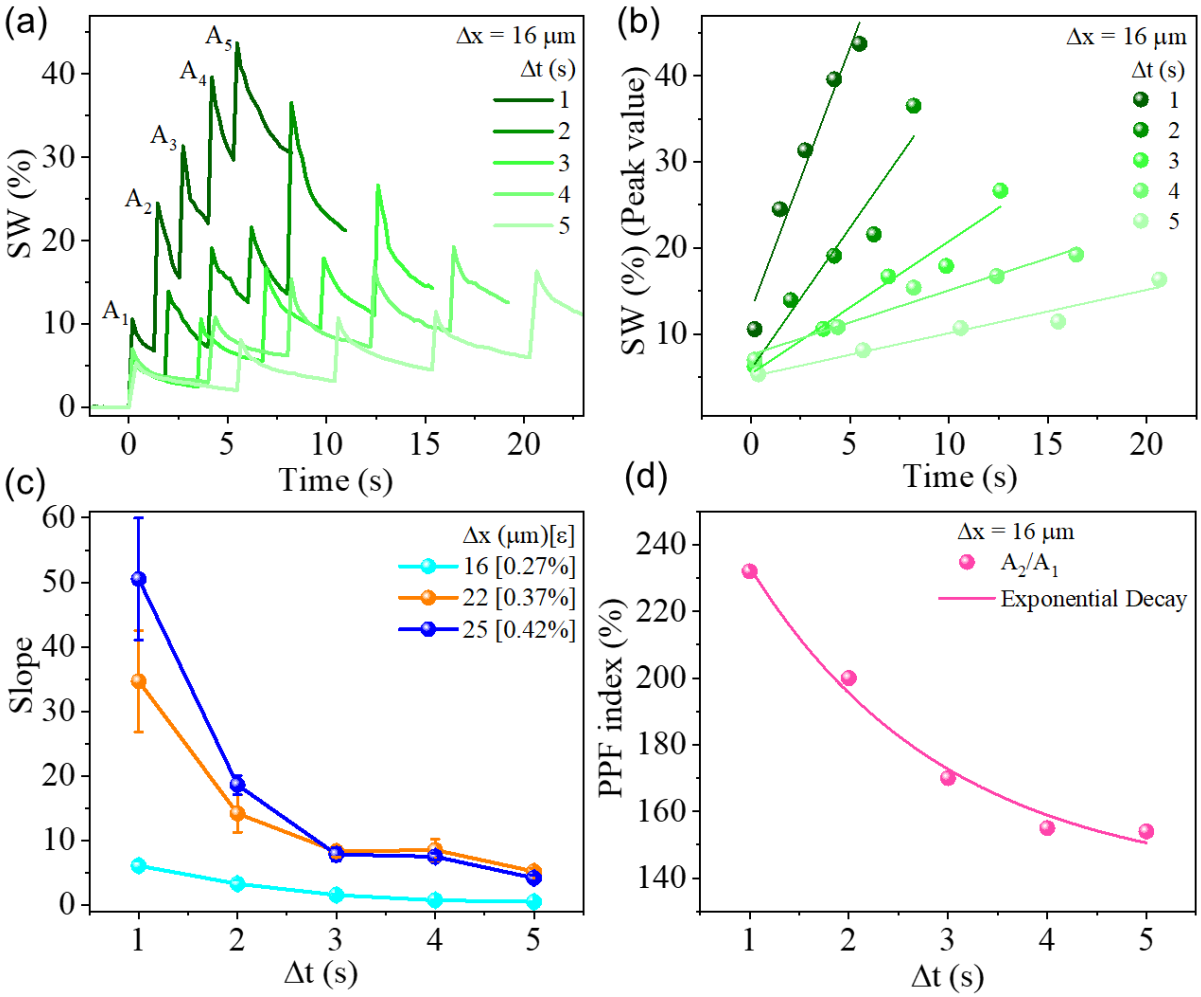

Figure VB.4: a) Change in SW of device when displacement pulses are applied at varying time intervals (Δt, 1 to 5 s) at a strain of 0.27% (Δx, 16 μm). (b) Variation in the peak value of SW with time for different Δt. The device shows a higher change in peak resistance at lower Δt values, depicting PPF behavior. (c) The slope obtained from the curve of variation of the peak value of SW with time is plotted at each pulse time interval for three pulse amplitudes Δx of 16, 22, and 25 μm and strain of 0.27%, 0.37%, and 0.42%, respectively. (d) Variation of PPF index with Δt fitted with an exponential decay curve.

As the amount of displacement pulse amplitude applied on the device increases, there will be more pronounced nano/micro gap formation in Au wires due to higher stretching, resulting in a higher resistance change value. The degree of enhancement in resistance due to the second pulse is explained in terms of the PPF index[23], which is given by the eqn:

$$\text{PPF index (\%)} = (A_2/A_1) \times 100 \qquad (4)$$

Where A_1 and A_2 are the peak resistance at the first and second pulse, respectively. PPF index shows a decreasing trend with time intervals and fits well with an exponential decay behavior[24]. Surprisingly, the PPF index value is more than 200%, which is comparable to the biological PPF index[22]. (Figure VB.4d). It corresponds to an enhancement in the strength of synaptic transmission in response to closely timed signals, effectively replicating the temporal correlation between neurons.

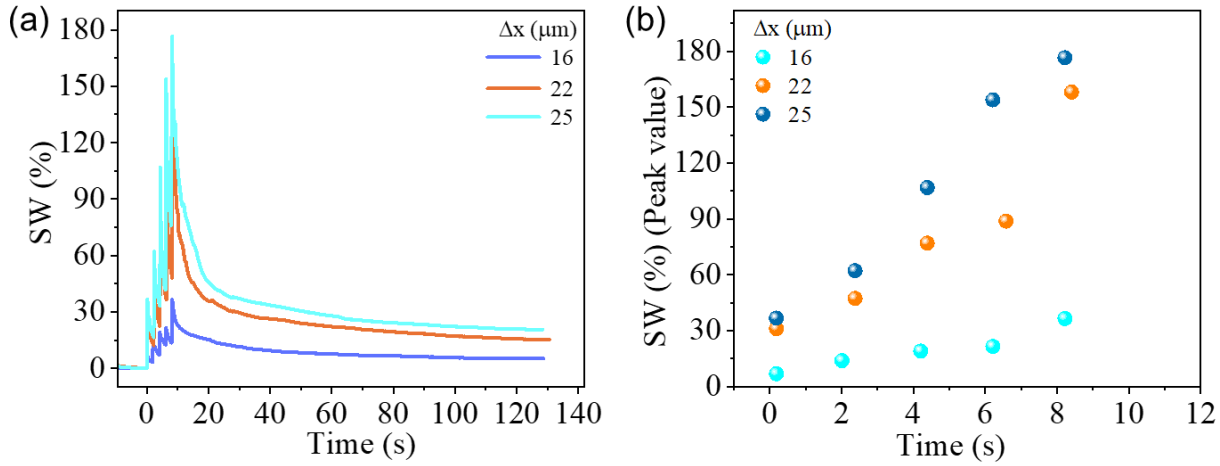

Figure VB.5: Variation of SW of the device with time at different displacement amplitudes depicting Spike amplitude dependent plasticity (SADP). (b) The peak values of SW plotted against time.

As the applied displacement pulses significantly influence the functionality of these devices, the amplitude of the pulse can also be utilized to replicate the plasticity observed in learning and memory in biological neurons. The phenomenon, known as Spike amplitude-dependent plasticity (SADP), showcases the ability to adjust plasticity based on spike amplitude[25]. The synaptic weight shows significant enhancement with an increase in the amplitude of displacement pulse from 16 μm (ε, 0.27%) to 25 μm (ε, 0.42%) attributed to the formation of larger micro/nanogaps in Au wires (Figure VB.5a). Consequently, this device can replicate the transition from STP to LTP by elevating the amplitudes of applied displacement pulses (Figure VB.5b).

Depending on the synaptic strength, the plasticity can manifest as short-term plasticity (STP), characterized by a transient increase that diminishes quickly after stimulation ceases, or long-term plasticity (LTP), involving strong changes in synaptic communication lasting for an extended period of time.

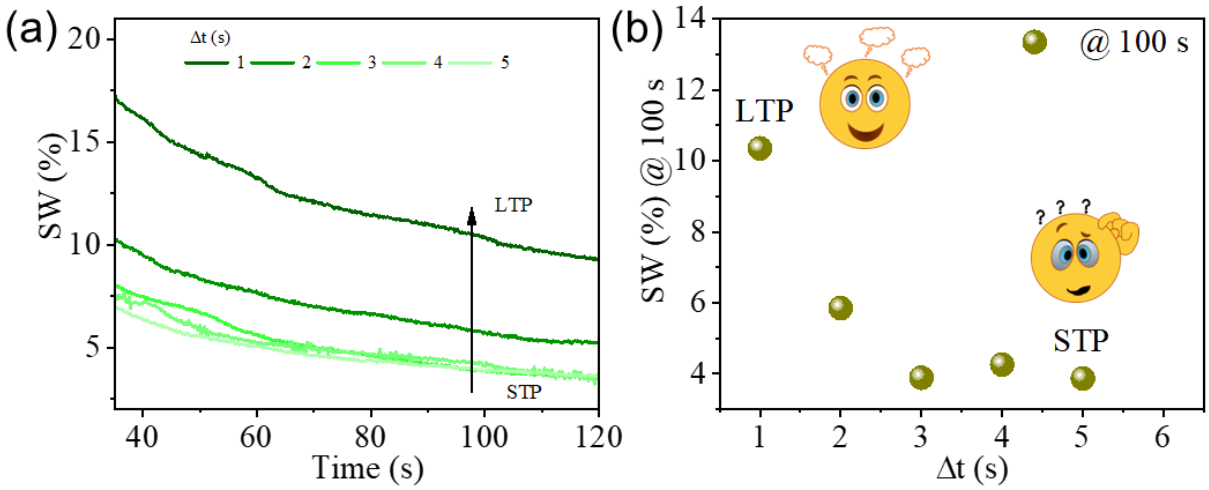

Figure VB.6: (a) Relaxation behavior of the device after the application of the pulses with different time intervals. (b) SW values indicating the change in synaptic weight at 100 s after pulsing.

To show the plasticity behavior in the device, the relaxation behavior was observed after the application of pulses at different intervals (Figure VB.6a). Notably, an efficient LTP can be induced with fewer stimuli if administered at shorter time intervals[26]. Hence, the introduced device exhibits STP characteristics at longer time intervals (Δt, 5 s), where the memory is not sustained for an extended period. Conversely, at shorter intervals (Δt, 1 s), the synaptic connections undergo reinforcement through rapid pulse application, leading to an extended duration and demonstrating LTP behavior. Therefore, by reducing the time interval of pulses (Figure VB.6b), a transition from STP to LTP can be achieved in the device.

VB.5 Conclusions

In essence, a novel strain-sensitive neuromorphic device comprising an interconnected network of Au microwires partially embedded in PDMS was demonstrated. By utilizing strain as input and measuring the resulting change in device resistance, various neuromorphic functionalities, including STP, LTP, SRDP, SADP, potentiation, and depression were demonstrated. The device exhibited a PPF index of 232%, closely mimicking biological systems and indicating robust temporal information processing. This research provides valuable insights into the development of tactile neuromorphic devices with advanced functionalities, paving the way for improved neurorobotics applications.

References

[1] Sandberg A 2016 Energetics of the brain and AI

[2] Ielmini D and Ambrogio S 2019 Emerging neuromorphic devices *Nanotechnology* **31** 92001

[3] Zou L, Ge C, Wang Z J, Cretu E and Li X 2017 Novel Tactile Sensor Technology and Smart Tactile Sensing Systems: A Review *Sensors* **17** 2653

[4] Hong S, Cho H, Kang B H, Park K, Akinwande D, Kim H J and Kim S 2021 Neuromorphic Active Pixel Image Sensor Array for Visual Memory *ACS Nano* **15** 15362–70

[5] Yun S-Y, Han J-K, Lee S-W, Yu J-M, Jeon S-B and Choi Y-K 2023 Self-aware artificial auditory neuron with a triboelectric sensor for spike-based neuromorphic hardware *Nano Energy* **109** 108322

[6] Yang L, Wang Z, Zhang S, Li Y, Jiang C, Sun L and Xu W 2023 Neuromorphic Gustatory System with Salt-Taste Perception, Information Processing, and Excessive-Intake Warning Capabilities *Nano Lett.* **23** 8–16

[7] Han J-K, Kang M, Jeong J, Cho I, Yu J-M, Yoon K-J, Park I and Choi Y-K 2022 Artificial Olfactory Neuron for an In-Sensor Neuromorphic Nose *Adv. Sci.* **9** 2106017

[8] Zeng M, He Y, Zhang C and Wan Q 2021 Neuromorphic Devices for Bionic Sensing and Perception *Front. Neurosci.* **15** 1–23

[9] Yu J, Wang Y, Qin S, Gao G, Xu C, Lin Wang Z and Sun Q 2022 Bioinspired interactive neuromorphic devices *Mater. Today* **60** 158–82

[10] Liu J, Wang Y, Liu Y, Wu Y, Bian B, Shang J and Li R 2024 Recent Progress in Wearable Near-Sensor and In-Sensor Intelligent Perception Systems *Sensors* **24** 2180

[11] Lee Y and Ahn J-H 2020 Biomimetic Tactile Sensors Based on Nanomaterials *ACS Nano* **14** 1220–6

[12] Jiang C, Liu J, Yang L, Gong J, Wei H and Xu W 2022 A Flexible Artificial Sensory Nerve Enabled by Nanoparticle-Assembled Synaptic Devices for Neuromorphic Tactile Recognition *Adv. Sci.* **9** 2106124

[13] Wang L, Zhang P, Gao Z and Wen D 2024 Artificial Tactile Sensing Neuron with Tactile Sensing Ability Based on a Chitosan Memristor *Adv. Sci.* **11** 2308610

[14] Wang M, Tu J, Huang Z, Wang T, Liu Z, Zhang F, Li W, He K, Pan L, Zhang X, Feng X, Liu Q, Liu M and Chen X 2022 Tactile Near-Sensor Analogue Computing for Ultrafast Responsive Artificial Skin *Adv. Mater.* **34** 2201962

[15] Jiang C, Li Q, Sun N, Huang J, Ji R, Bi S, Guo Q and Song J 2020 A high-performance bionic pressure memory device based on piezo-OLED and piezo-memristor as luminescence-fish neuromorphic tactile system *Nano Energy* **77** 105120

[16] Sun F, Lu Q, Hao M, Wu Y, Li Y, Liu L, Li L, Wang Y and Zhang T 2022 An artificial neuromorphic somatosensory system with spatio-temporal tactile perception and feedback functions *npj Flex. Electron.* **6** 72

[17] Chen J, Zheng J, Gao Q, Zhang J, Zhang J, Omisore O M, Wang L and Li H 2018 Polydimethylsiloxane (PDMS)-Based Flexible Resistive Strain Sensors for Wearable Applications *Appl. Sci.* **8** 345

[18] Gupta N, Rao K D M, Srivastava K, Gupta R, Kumar A, Marconnet A, Fisher T S and Kulkarni G U 2018 Cosmetically Adaptable Transparent Strain Sensor for Sensitively Delineating Patterns in Small Movements of Vital Human Organs *ACS Appl. Mater. Interfaces* **10** 44126–33

[19] Li F, Wang R, Song C, Zhao M, Ren H, Wang S, Liang K, Li D, Ma X, Zhu B, Wang H and Hao Y 2021 A Skin-Inspired Artificial Mechanoreceptor for Tactile Enhancement and Integration *ACS Nano* **15** 16422–31

[20] Garcia J R, O'Suilleabhain D, Kaur H and Coleman J N 2021 A Simple Model Relating Gauge Factor to Filler Loading in Nanocomposite Strain Sensors *ACS Appl. Nano Mater.* **4** 2876–86

[21] Martin S J, Grimwood P D and Morris R G M 2000 Synaptic Plasticity and Memory: An Evaluation of the Hypothesis *Annu. Rev. Neurosci.* **23** 649–711

[22] Jackman S L and Regehr W G 2017 The Mechanisms and Functions of Synaptic Facilitation *Neuron* **94** 447–64

[23] Rao T S, Kundu S, Bannur B, George S J and Kulkarni G U 2023 Emulating

Ebbinghaus forgetting behavior in a neuromorphic device based on 1D supramolecular nanofibres *Nanoscale* **15** 7450–9

[24] Hu L, Li L, Chang K-C, Lin X, Huang P and Zhang S 2021 Ultrasensitive Freestanding and Mechanically Durable Artificial Synapse with Attojoule Power Based on Na-Salt Doped Polymer for Biocompatible Neuromorphic Interface *Adv. Funct. Mater.* **31** 2106015

[25] Monalisha P, Li S, Jin T, Kumar P S A and Piramanayagam S N 2023 A multilevel electrolyte-gated artificial synapse based on ruthenium-doped cobalt ferrite *Nanotechnology* **34** 165201

[26] Ohno T, Hasegawa T, Tsuruoka T, Terabe K, Gimzewski J K and Aono M 2011 Short-term plasticity and long-term potentiation mimicked in single inorganic synapses *Nat. Mater.* **10** 591–5

Chapter VI

Summary and Outlook

In this thesis, the optimization and fabrication of the neuromorphic devices is demonstrated by simple processes. The dewetted Ag nanostructures resembling biological neural networks were used as an active material for the device. These self-formed structures show the emulation of synaptic functionalities such as threshold switching, STP, and LTP with strategically designed voltage pulses **(Chapter III)**. With this device, several higher-order learning behaviors including classical associative learning, and second-order associative learning were emulated. In addition, Ebbinghaus's forgetting of associative learning was also demonstrated for the first time. A flexible neuromorphic device was fabricated by taking Kapton as a substrate **(Chapter IV)**. The device could emulate the synaptic functionalities in the bent state including STP and LTP. Also, bent-state classical conditioning was achieved for the first time. A dual-functional strain-sensitive neuromorphic device was fabricated using crackle lithography on a PDMS substrate **(Chapter VA)**. The device acts as a strain sensor as well as a neuromorphic device depending upon its strain range. The device could show the STP, LTP, strain-dependent switching and plasticity. The sensitivity in the neuromorphic regime was found to be enhanced as compared to the strain-sensor regime. By taking strain as an additional stimulus, the pain-related response of the biological systems such as nociception, habituation and antinociception was emulated. A tactile neuromorphic device utilising strain as a direct stimulus was fabricated **(Chapter VB)**. The device could show the basic plasticity behavior such as threshold switching, STP, LTP, SRDP and SADP. Also, this device exhibits a PPF index of 232% which is close to the biological value.

These devices with other bio-inspired architectures could enhance their applicability in complex neuromorphic networks. The successful emulation of synaptic functionalities in a flexible state suggests significant potential for wearable and flexible electronics applications. Further exploration into integrating flexible neuromorphic devices with other flexible components could lead to fully flexible neuromorphic systems for advanced applications in soft robotics and wearable computing.

The dual-functional capabilities of the strain-sensitive neuromorphic device open new avenues for multi-functional sensor systems. The ability to emulate pain-related responses suggests potential applications in artificial sensory systems, such as prosthetics and haptic feedback devices. Further work may also explore the integration of additional sensory modalities to create more comprehensive artificial sensory systems. The tactile neuromorphic demonstrates its potential for applications in artificial tactile sensing and neuroprosthetics. Integrating these devices into larger neuromorphic systems could enable advanced functionalities, such as more nuanced haptic feedback in virtual and augmented reality environments, and more responsive robotic touch systems.

List of Publications

From this thesis

1. **Bhupesh Yadav**, Indrajit Mondal, Bharath Bannur and G.U. Kulkarni, Emulating learning behavior in a flexible device with self-formed Ag dewetted nanostructure as active element. ***Nanotechnology*** **2023**, 35, 015205.

2. Bharath Bannur, **Bhupesh Yadav**, G.U. Kulkarni, Second-Order Conditioning Emulated in an Artificial Synaptic Network. ***ACS Appl. Electron. Mater.*** **2022** ,4, 1552–1557.

3. **Bhupesh Yadav,** Indrajit Mondal, Manpreet Kaur, Vidhyadhiraja N. S., and G.U. Kulkarni, Stretchable hierarchical metal wire networks for neuromorphic emulation of nociception and anti-nociception. ***Mater. Horiz.***, **2024**.

4. Shubhanshi Mishra ǂ, **Bhupesh Yadav ǂ** and G.U. Kulkarni, A strain-sensitive neuromorphic device emulating mechanoreception for different skin sensitivities. ***J. Mater. Chem. C***, **2024**, 12, 18243-18255.

5. **Bhupesh Yadav** and G.U. Kulkarni, Optimized Active Material for Neuromorphic Device Fabrication: Emulating Ebbinghaus Forgetting in Associative Learning (Manuscript under preparation).

6. Indrajit Mondal, Rohit Attri, Tejaswini S. Rao, **Bhupesh Yadav**, G.U. Kulkarni, Recent trends in neuromorphic systems for non-von Neumann in materia computing and cognitive functionalities. ***Appl. Phys. Rev.***, **2024**, 11, 041304.

Co-authored publications

1. Rohit Attri, Indrajit Mondal, **Bhupesh Yadav**, G.U. Kulkarni, and C.N.R. Rao, Neuromorphic devices realised using self-forming hierarchical Al and Ag nanostructures: towards energy-efficient and wide-ranging synaptic plasticity. ***Mater. Horiz.*** **2024**, 11, 737–746.
2. Shubham K. Mehta, Indrajit Mondal, **Bhupesh Yadav** and Giridhar U. Kulkarni, Energy-efficient resistive switching synaptic devices based on patterned Ag nanotriangles with tunable gaps fabricated using plasma-assisted nanosphere lithography. ***Nanoscale***, **2024**, 16, 18365-18374.
3. Mousona Pal, Manpreet Kaur, **Bhupesh Yadav**, Arti Bisht, Vidhyadhiraja N. S., Giridhar U. Kulkarni, A Self-Formed Ag Nanostructure Based Neuromorphic Device Performing Arithmetic Computation and Area Integration: Influence of

Presynaptic Pulsing Scheme on Mathematical Precision. **ACS Appl. Mater. Interfaces**, **2025.**

4. Ankit Kumar, Nikita Gupta, **Bhupesh Yadav**, Chirag Sarthi, Umesh V Waghmare and G. U. Kulkarni, Heating effect on wrinkles and stacking order in Graphene stack (Manuscript under preparation)

5. Mousona Pal, **Bhupesh Yadav**, and Indrajit Mondal and G. U. Kulkarni, Low Voltage Threshold Switching in Hierarchical Ag Nanostructures: Unveiling Gap-Dependent Synaptic Plasticity. (Manuscript Under Preparation)